



Electrical and Thermal Transport through Spin-Orbit coupled Nano-junctions: An emphasis on Graphene based junction devices

A THESIS SUBMITTED FOR THE AWARD OF THE
DEGREE OF DOCTOR OF PHILOSOPHY IN PHYSICS BY

PRIYADARSHINI KAPRI

Supervisor: Prof. Saurabh Basu



INDIAN INSTITUTE OF TECHNOLOGY GUWAHATI

DEPARTMENT OF PHYSICS

GUWAHATI-781039, ASSAM, INDIA

Guwahati, December 2018



Abstract

The thesis investigates electrical and heat transport in spin-orbit coupled normal-superconductor and normal-insulator-superconductor based junction devices via a modified version of the Blonder - Tinkham - Klapwijk (BTK) theory. The primary motivation is to study the conductance characteristics of these junction devices in presence of Rashba spin-orbit coupling. In this thesis, we explore both electrical and thermal transport and how they can be controlled via tuning the fundamental properties of these junctions. Further, the interplay between the spin-orbit coupling and the parameters that characterize the insulating region has been studied extensively in the thesis. Moreover realistic applications of these junction has remained a prime focus with a view of fabricating devices. Particularly, applicability of these junctions for tunable delivery of thermopower and as a thermoelectric cooling device are discussed in details. A special emphasis is laid towards the latter part of the thesis on the graphene-based junction devices owing to their non-trivial topological physics and possible spintronic applications, which have motivated us to study the conductance features of a spin-orbit coupled graphene based junction. The presence of the spin-orbit couplings, namely, the intrinsic and the Rashba couplings in graphene is included via the Kane-Mele Hamiltonian. The transmission properties and practical applications of the Kane-Mele normal-insulator-superconductor junctions are studied thoroughly. Finally, a comparison between a usual junction (with parabolic energy dispersion) and a graphene based junction (linear energy dispersion) with regard to their charge and heat transport is presented.





© 2018- Priyadarshini Kapri





*Dedicated to my parents and
grandparents ...*



Acknowledgement

First and foremost, I would like to express my gratitude to my research supervisor, Prof. Saurabh Basu for giving me the opportunity to join in his research group. His constant guidance, knowledge and intelligent ideas have helped me to complete my thesis work successfully well in time. Despite his own busy official schedule, he gave me time for discussion throughout all these years. The most important thing, I have tried to learn from him in these years is his capability to represent things in a compact way. Finally, It has been a pleasure for me to work under his guidance.

I would like to thank the doctoral committee members Prof. Perumal Alagarsamy, Dr. Debaprasad Maity, Dr. Uday Narayan Maiti and Dr. Manabendra Sarma for reviewing my progress every year and for their frank comments and valuable suggestions.

I am thankful to all other faculty members and the HoDs of the Physics department for their friendly behaviour. I am grateful to Indian Institute of Technology Guwahati, and Government of India, Ministry of Human Resource Development for the financial support. I wish to thank Department of Physics, IIT Guwahati for providing me the necessary computational facilities. I thank all the technical assistants of the department of physics, especially Mr. Basab Bijoy Purkayastha, for their assistance in various ways during my research period.

I would like to thank my senior Dr. Sudin Ganguly for his cooperation. My special thanks go to my junior Sunayana for her assistance in several ways. I would also like to thank my other group members Noor, Priyanka and Shilpi for their help.

I feel fortunate for having Susmita Ghosh, Soumya Basu and Eshita Mal as my best friends with whom I enjoyed so much fun, friendship and excitement during my Ph.D.

My Special thanks go to Semanti Chakroborty (friend cum teacher) and Anamika Ghosh for their assistance and support during my B.Sc.

I am grateful to my teachers Mr. Sadananda Sau, Mr. Pankaj Ghatak and Mr. Gora Chand Samanta for their words of encouragement.

I am also thankful to my other friends, Camelia, Subhadeep, Bijita, Sangkha, Sanjeeb for their friendly behaviour and support.

I am grateful to all my family members and particularly, my parents and brother, for their love and encouragement during my entire academic career. No word is enough to express their love and constant support throughout my endeavor. Finally, I am deeply indebted to my grandparents for their unconditional love and support. They always stood by me and their constant support makes what I am today.

Guwahati, December 2018

Priyadarshini Kapri



Declaration

The work contained in the thesis entitled “Electrical and Thermal Transport through Spin-Orbit coupled Nano-junctions: An emphasis on Graphene based junction devices ” has been carried out at the Department of Physics, Indian Institute of Technology Guwahati, India by me under the supervision of Prof. Saurabh Basu, Professor, Department of Physics, IIT Guwahati. The material of this thesis has not been submitted elsewhere for any other degree. Works presented in the thesis are all my own unless referenced to the contrary in the text.

(Priyadarshini Kapri)

December 2018

Department of Physics

Indian Institute of Technology Guwahati

Guwahati - 781039

India



Disclaimer

The bibliography included in this thesis is, by no means complete but contains the ones which are consulted thoroughly by me. I apologize for inadvertently missing out some of the research papers, review articles and other scientific documents pertaining to the focus of this thesis which should also have been cited. For illustration purpose some of the figures in this thesis are taken from other sources and have been properly cited.





Certificate

This is to certify that the work contained in the thesis titled "Electrical and Thermal Transport through Spin-Orbit coupled Nano-junctions: An emphasis on Graphene based junction devices" by Ms. Priyadarshini Kapri (Roll no.-136121017), a Ph.D. student of the Department of Physics, Indian Institute of Technology Guwahati is carried out under my supervision and has not been submitted elsewhere for the award of any other degree.

(Prof. Saurabh Basu)
December 2018
Department of Physics
Indian Institute of Technology Guwahati
Guwahati - 781039
India





List of Publications

Journal Articles:

1. *Tunneling conductance study of a metal-superconductor junction in the presence of Rashba spin orbit coupling**¹,

Priyadarshini Kapri and Saurabh Basu, Eur. Phys. J. B, **90**, 33 (2017).

2. *Bound state, phase separation and superconductivity in presence of Rashba spin-orbit coupling,*

Priyadarshini Kapri and Saurabh Basu, Physica C, **537**, 10 (2017).

3. *Tunneling conductance oscillations in spin-orbit coupled metal - insulator - superconductor junctions**,

Priyadarshini Kapri and Saurabh Basu, Eur. Phys. J. B, **91**, 12 (2018).

4. *Controlled thermoelectric response of a tunable Rashba coupled metal-insulator-superconductor junction**,

Priyadarshini Kapri, Priyanka Adhikary, Shubham Sinha, Saurabh Basu, Physica E **99**, 67 (2018).

5. *Tunable refrigeration properties of nano-scale Rashba coupled junction devices**,

Priyadarshini Kapri and Saurabh Basu, Physica E, **103**, 383 (2018).

6. *Andreev reflection across a Kane-Mele normal-superconductor nano-junction**,

Priyadarshini Kapri and Saurabh Basu, Euro. Phys. Lett. **124**, 17002 (2018).

7. *Thermopower generation and thermoelectric cooling in a Kane-Mele normal-insulator-superconductor nano-junction**,

Priyadarshini Kapri and Saurabh Basu, Euro. Phys. Lett. (Submitted).

Conference Proceedings:

1. *Tunneling conductance through normal metal-superconductor junctions : effects of Rashba spin orbit coupling and magnetic field,*

Priyadarshini Kapri, Sudin Ganguly and Saurabh Basu, Journal of Physics: Conference Series **759** 012031 (2016).

2. *Tunneling between normal metal and s-wave superconductor: Effects of Rashba spin-orbit coupling and finite quasiparticle lifetime,*

Priyadarshini Kapri and Saurabh Basu, SBN 978-93-86256-85-0 (2017).

3. *Refrigeration properties of Rashba spin-orbit coupled normal-insulator-superconductor*

¹* These journal articles with some modifications are included in this thesis .

based junction device.

Priyadarshini Kapri and Saurabh Basu, Journal of Physics: Conference Series (Submitted).

Conference/School Attended:

- 1. XXVII IUPAP International Conference on Computational Physics**, I.I.T. Guwahati, Guwahati, Assam, India, 2015.
- 2. X PANE Biennial Conference**, St. Anthony's college, Meghalaya, India, 2016.
- 3. PRL conference on Condensed Matter Physics**, Physical Research Laboratory, Gujrat, India, 2018.
- 4. XXX IUPAP International Conference on Computational Physics**, University of California, Davis, California, USA, 2018.



Contents

Abstract	1
Acknowledgement	7
Declaration	9
Disclaimer	11
Certificate	13
Publication	15
1 Introduction	29
1.1 Spin-orbit coupling	34
1.2 Rashba spin-orbit coupling	37
1.3 Bogoliubov-deGennes equations	39
1.4 Normal metal and superconductor junction: Andreev reflection	41
1.5 Normal-insulator-superconductor junction and Fabry-Perot-like oscillations	46
1.6 Basics of Graphene	47
1.7 Klein tunneling in graphene	49
1.8 Kane-Mele Model	52
1.9 Outline of the thesis	53
2 Blonder-Tinkham-Klapwijk (BTK) formalism	57
2.1 Normal-superconductor (NS) junction	57
2.2 Normal-insulator-superconductor (NIS) junction	61
2.3 Graphene based NS junction: Kane-Mele model	66
2.4 Graphene (Kane-Mele) based NIS junction	71
3 Charge transport through NS and NIS junction	77
3.1 Normal-superconductor junction	78
3.2 Results on s-wave pairing symmetry	79
3.3 Other pairing symmetries	82
3.3.1 p-wave superconductor	83
3.3.2 d-wave superconductor	83
3.4 Fermi surface mismatch	86
3.5 Finite quasiparticle lifetime	88
3.6 Normal-superconductor junction (NS) with interfacial RSOC	89
3.7 Normal-insulator-superconductor junction	90

3.7.1 Results and discussions	90
3.8 Conclusions	95
4 Thermoelectric properties of NIS junction	97
4.1 Charge and thermal current through NIS junction	98
4.1.1 Seebeck coefficient	100
4.1.2 Figure of Merit	102
4.1.3 Thermoelectric cooling	103
4.2 Results and discussions: Thermopower	104
4.2.1 Figure of Merit	108
4.3 Results and discussions: Thermoelectric cooling	110
4.3.1 Coefficient of Performance (COP)	113
4.4 Concluding remarks	115
5 Charge transport through graphene based NS junction	117
5.1 Graphene based NS junction	118
5.1.1 Results and Discussions on Kane-Mele NS junction	119
5.2 Kane-Mele NIS junction	124
5.2.1 Results and Discussions on Kane-Mele NIS junction	125
5.3 Conclusion	128
6 Thermoelectric effects of Kane-Mele NIS junction	129
6.1 Kane-Mele NIS junction	130
6.1.1 Seebeck coefficient	131
6.1.2 Thermoelectric cooling	132
6.2 Results and Discussions	133
6.2.1 Seebeck Coefficient and Figure of Merit	134
6.2.2 Thermoelectric cooling and coefficient of performance	138
6.3 Conclusion	140
7 Comparison between generic and graphene based junction system in charge and heat transport	143
7.1 Comparison for electrical current	143
7.2 Comparison of thermoelectric properties	145
7.3 Conclusion	147
8 Conclusions	149
9 Appendix: Simpson's Rule for 2D integration	153
Bibliography	164





List of Figures

1.1	(a) Three-dimensional energy spectrum of the Hamiltonian H (Eqn.(1.21)). (b) The Fermi energy contours for the Hamiltonian H . (c) Energy spectrum for a free electron. (d) Energy spectrum for an electron in presence of a magnetic field (Zeeman splitting). (e) Energy spectrum for an electron in presence of Rashba spin-orbit coupling. Courtesy Ref.[96].	38
1.2	(a) NS and (b) NIS junction. Dashed regions are occupied states. Grey block in (b) is an interface barrier. Courtesy Ref.[102].	42
1.3	Electrical transport at an NS junction. The motion of electrons (e^-) and holes (h^+) and their respective spin (\uparrow, \downarrow) are indicated. The cooper pair at the Fermi energy, the superconducting gap Δ , and the superconducting density of states are shown. Courtesy Ref.[20].	43
1.4	Four processes at NS interface are shown, namely, (a) specular reflection, (b) Andreev reflection, (c) transmission as an electron, (d) transmission as a hole. Arrows point in a direction towards the velocity of the particle, and abbreviations for the directions are: eR - a right moving electron, eL - a left moving electron, hR - a right moving hole, hL - a left moving hole. Full lines denote electron trajectories, dashed lines denote hole trajectories. Courtesy Ref.[102].	44
1.5	NIS junction with the possible trajectories after AR at the superconducting interface. The nomenclature is same as in Fig.(1.4). Courtesy Ref.[102].	45
1.6	Schematic of Fabry-Perot interferometer	46
1.7	(a) Honeycomb lattice structure of graphene. The vectors $\vec{\delta}_1, \vec{\delta}_2$ and $\vec{\delta}_3$ connect NN carbon atoms. The vectors \vec{a}_1 and \vec{a}_2 are the basis vectors. (b) First Brillouin zone (BZ) of the honeycomb lattice. Its primitive lattice vectors are \vec{b}_1 and \vec{b}_2	48
1.8	Electronic band structure of graphene. Left: energy spectrum (in units of nearest neighbour hopping strength, t_1). Right: enlarged view of the energy bands close to one of the Dirac points. Courtesy of Ref.[49].	50
1.9	(a) An energy barrier with width d and height V_0 , (b) Three regions in this problem.	51
2.1	(a) Schematic illustration of the reflection and the transmission processes of the quasiparticle at an NS junction. (b) Profile for a d -wave superconducting gap. α' is the angle between the crystalline orientation and the x axis.	58

2.2	Schematic illustration of an NIS junction setup.	62
2.3	Schematic illustration of the reflection and the transmission processes of the quasiparticle at an NIS junction. The insulating region is between $[0 : d]$. Solid lines denote the electrons and the dashed lines denote the holes.	63
2.4	Schematic diagram of graphene. The coordinates of A and B sublattices are shown. The nearest neighbour vectors are denoted by $\vec{\delta}_i$ and the next-nearest neighbour vectors are denoted by $\vec{\epsilon}_i$	67
2.5	Schematic diagram of a graphene based NIS junction setup.	72
3.1	The variation of the normalized conductance, G for a s -wave superconductor as a function of E/Δ_0 for different strengths of RSOC with $U_0 = 0$ (transparent barrier). There is no visible effect of RSOC. The value 2 denotes the conductance equal to $4e^2/h$	79
3.2	The variation of the AR in (a) and NR in (b) for s -wave superconductor as a function of E/Δ_0 for a transparent barrier.	80
3.3	The variation of the conductance, G for a s -wave superconductor as a function of E/Δ_0 for different strengths of RSOC with $U_0 = E_F^N$ (opaque barrier).	81
3.4	The variation of the (a) AR and the (b) NR for a s -wave superconductor as a function of E/Δ_0 for an opaque barrier.	81
3.5	The variation of the zero bias conductance, $G(E = 0)$ for a s -wave superconductor as a function of RSOC strength, $\hat{\eta}_R$	82
3.6	The variation of the conductance, G for a p -wave superconductor as a function of E/Δ_0 for different strengths of RSOC for (a) $U_0 = 0$ (transparent barrier) and (b) $U_0 = E_F^N$ (opaque barrier).	84
3.7	The variation of the conductance, G for a d -wave superconductor as a function of E/Δ_0 for different strengths of RSOC with (a) $\alpha' = 0$ and $U_0 = 0$, (b) $\alpha' = 0$ and $U_0 = E_F^N$, (c) $\alpha' = \pi/4$ and $U_0 = 0$, (d) $\alpha' = \pi/4$ and $U_0 = E_F^N$	84
3.8	The variation of the conductance, $G(E)$ for a s -wave superconductor as a function of E/Δ_0 for (a) $\hat{\eta} = 0.5$, (b) $\hat{\eta} = 2$ with a transparent barrier ($U_0 = 0$).	86
3.9	The variation of the conductance, $G(E)$ for a s -wave superconductor as a function of E/Δ_0 for (a) $\hat{\eta} = 0.5$, (b) $\hat{\eta} = 2$ with an opaque barrier ($U_0 = E_F^N$).	87
3.10	The variation of the (a) AR and (b) the NR for a s -wave superconductor as a function of E/Δ_0 for a transparent barrier ($U_0 = 0$), the variation of the (c) AR and (d) the NR for a s -wave superconductor as a function of E/Δ_0 for an opaque barrier ($U_0 = E_F^N$).	88

3.11	The variation of the conductance, $G(E)$ for a s-wave superconductor as a function of E/Δ_0 for an opaque barrier with (a) $\hat{\eta} = 1$ and (b) $\hat{\eta} = 2$	89
3.12	The variation of the conductance, G for a s-wave superconductor as a function of biasing energy, E/Δ_0 for a conventional NIS junction.	91
3.13	The variation of the conductance, G for a s-wave superconductor as a function of χ ($k_F^l d$) corresponding to zero bias condition ($E/\Delta_0 = 0$) for different strengths of RSOC. The other parameters are $V_1 = E_F^N$, $\Gamma/\Delta_0 = 0.1$	92
3.14	The variation of the conductance, G for a s-wave superconductor as a function of E/Δ_0 for different strengths of RSOC for two values of the χ , namely, (a) χ_1 and (b) χ_2	93
3.15	(a) The variation of the conductance, $G(E = 0)$ for a s-wave superconductor as a function of RSOC strength $\hat{\eta}_R$, (b) the color maps of the zero bias conductance ($G(E = 0)$) as the function of $\hat{\eta}_R$ and χ	94
4.1	Schematic Diagram of the NIS junction setup as a thermopower device.	99
4.2	Schematic Diagram of the NIS junction setup as a cooling device. It may be noted that a bias voltage V_B is introduced for thermoelectric cooling.	103
4.3	The variation of the Seebeck coefficient, S as function of effective barrier potential, χ . The oscillations are artifacts of electron interferences.	105
4.4	The variation of the Seebeck coefficient, S as a function of temperature scaled by superconducting gap, T/Δ_0 for two different values of χ , namely, (a) χ_1 , (b) χ_2	106
4.5	(a) The variation of the Seebeck coefficient, S as function of $\hat{\eta}_R$. (b) The variation of S as function of both $\hat{\eta}_R$ and χ	107
4.6	The variation of the Figure of Merit (ZT) as a function of effective barrier potential, χ for different strengths of RSOC, $\hat{\eta}_R$	108
4.7	The variation of the Figure of Merit (ZT) as a function of temperature, T/Δ_0 for two different regions of the effective barrier potential, χ , namely, (a) χ_1 , (b) χ_2	109
4.8	(a) The variation of ZT as a function of $\hat{\eta}_R$, (b) The variation of ZT as function of both $\hat{\eta}_R$ and χ	109
4.9	The variation of the thermal current (J_{NS}), rendered dimensionless by $2J_{NS}e^2R_N/\Delta_0^2$ as a function of the effective barrier potential, χ	111

4.10	The variation of $2J_{NS}e^2R_N/\Delta_0^2$ as function of driving voltage, V_B (scaled by the superconducting order parameter, Δ_0) for two different values of χ , namely, (a) χ_1 , (b) χ_2 . The upper and lower critical values of the biasing voltage where refrigeration works are shown.	112
4.11	(a) The variation of $2J_{NS}e^2R_N/\Delta_0^2$ as function of RSOC strength, $\hat{\eta}_R$, (b) The variation of $2J_{NS}e^2R_N/\Delta_0^2$ as function of both $\hat{\eta}_R$ and χ .	113
4.12	The variation of COP as function of χ for different strength of RSOC.	114
4.13	The variation of COP as function of biasing voltage, V_B (scaled by the superconducting order parameter, Δ_0) for two different χ values (namely (a) χ_1 and (b) χ_2).	114
4.14	(a) The variation of COP as function of $\hat{\eta}_R$, (b) The variation of COP as function of both $\hat{\eta}_R$ and χ .	115
5.1	(a) The variation of conductance for the up spin, G_{up} as a function of biasing voltage (scaled by the superconducting order parameter), E/Δ_0 , (b) The variation of conductance for the down spin, G_{down} as the function of E/Δ_0 .	120
5.2	The variation of the spin resolved conductance, as a function of RSOC strength, when ISOC term is kept at zero ($\hat{\eta}_I = 0$).	121
5.3	(a) The variation of conductance for the up spin, G_{up} as a function of biasing voltage scaled by the superconducting order parameter, E/Δ_0 , (b) The variation of conductance for the down spin, G_{down} as the function of E/Δ_0 .	121
5.4	The variation of spin resolved conductance, as the function of ISOC strength, $\hat{\eta}_I$.	122
5.5	The variation of the spin resolved conductance as the function of E/Δ_0 for (a) $\hat{\eta}_R > \hat{\eta}_I$, (b) $\hat{\eta}_R < \hat{\eta}_I$.	123
5.6	The color maps of the spin resolved conductance as the function of $\hat{\eta}_R$ and $\hat{\eta}_I$ for (a) up spin and (b) down spin.	124
5.7	The variation of conductance for (a) the up spin, G_{up} and for (b) the down spin, G_{down} as a function of χ with $\hat{\eta}_I = 0$.	125
5.8	The variation of conductance for (a) the up spin, G_{up} and for (b) the down spin, G_{down} as a function of χ with $\hat{\eta}_R = 0$.	126
5.9	The variation of spin resolved conductance as a function of χ for a full Kane-Mele Hamiltonian.	126
5.10	The variation of spin resolved conductance as a function of SOC strength for (a) up spin and χ_1 , (b) down spin and χ_1 , (c) up spin and χ_2 , (d) down spin and χ_2 .	127

6.1	The variation of the Seebeck coefficient, S as a function of temperature, T (scaled by superconducting order parameter, Δ_0) (a) for pristine graphene, (b) for Au decorated graphene. The values of the spin-orbit coupling are shown in the figure.	134
6.2	The variation of the Seebeck coefficient, S as a function of temperature, T/Δ_0 for a larger RSOC parameter by one order greater magnitude compared to that of the Au decorated graphene.	135
6.3	The variation of the spin resolved Seebeck coefficient, S as function of $\hat{\eta}_R$ and $\hat{\eta}_I$ for (a) up spin, (b) down spin. Reddish yellow regions indicate the parameters values needed for the achieving maximum, S	135
6.4	(a) The variation of the charge Seebeck coefficient as function of $\hat{\eta}_R$ and $\hat{\eta}_I$, (b) The variation of the spin Seebeck coefficient as function of $\hat{\eta}_R$ and $\hat{\eta}_I$	136
6.5	The variation of Figure of Merit, ZT as a function of temperature, T (scaled by superconducting order parameter, Δ_0) for (a) $\hat{\eta}_R = 0$ and $\hat{\eta}_I = 0$, (b) $\hat{\eta}_R = 0.165t_1$ and $\hat{\eta}_I = 0.007t_1$	137
6.6	The variation of the 'Figure of Merit', ZT as function of $\hat{\eta}_R$ and $\hat{\eta}_I$ for (a) up spin and (b) down spin.	137
6.7	(a) The variation of the charge 'Figure of Merit', $Z_{ch}T$ as function of $\hat{\eta}_R$ and $\hat{\eta}_I$, (b) The variation of the spin 'Figure of Merit', $Z_{sp}T$ as function of $\hat{\eta}_R$ and $\hat{\eta}_I$	138
6.8	The variation of the dimensionless thermal current, $2J_{NS}e^2R_N/\Delta_0^2$ as a function of biasing voltage, V_B (scaled by superconducting order parameter, Δ_0) for (a) $\hat{\eta}_R = 0$ and $\hat{\eta}_I = 0$, (b) $\hat{\eta}_R = 0.165t_1$ and $\hat{\eta}_I = 0.007t_1$. The operating regions are indicated.	138
6.9	The variation of the thermal current, $2J_{NS}e^2R_N/\Delta_0^2$ as a function of $\hat{\eta}_R$ and $\hat{\eta}_I$ for (a) up spin and (b) down spin.	139
6.10	The variation of the coefficient of performance, COP as a function of biasing voltage, V_B (scaled by superconducting order parameter, Δ_0) for (a) $\hat{\eta}_R = 0$ and $\hat{\eta}_I = 0$, (b) $\hat{\eta}_R = 0.165t_1$ and $\hat{\eta}_I = 0.007t_1$	140
6.11	The variation of the COP as a function of $\hat{\eta}_R$ and $\hat{\eta}_I$ for (a) up spin and (b) down spin.	140
7.1	The variation of the conductance, G as a function of biasing energy, E (scaled by superconducting order parameter, Δ_0) for (a) usual NIS junction system and for (b) graphene based junction system. Graphene based NIS junctions register a slightly larger conductance.	144

7.2 The variation of the conductance, G as a function χ , for (a) generic junction system (parabolic energy dispersion) and for (b) for graphene based junction system (linear energy dispersion). 145

7.3 The variation of the Seebeck coefficient, S as a function of temperature, T/Δ_0 (scaled by superconducting order parameter, Δ_0) for (a) generic 2D junction system (parabolic dispersion) and for (b) graphene based junction system (linear energy dispersion). S is suppressed for the graphene based junction. 146

7.4 The variation of the dimensionless thermal current, $(2J_{NS}e^2R_N)/\Delta_0^2$ as a function of biasing voltage, V_B/Δ_0 (scaled by superconducting order parameter, Δ_0) for (a) generic 2D junction system (parabolic dispersion) and for (b) graphene based junction system (linear energy dispersion). The operating region is smaller for (b). 146



List of Tables

- 3.1 Behavior of amplitudes of the Andreev reflection (AR) and the normal reflection (NR) with RSOC strength. 95





Chapter 1: Introduction

The quantum transport in mesoscopic dimensions is of crucial importance and a key to the success of modern research in developing the devices at atomic / molecular level. Over the last two decades the development in fabrication techniques provides the possibility to experimentally realize mesoscopic dimensions. The well-known techniques are the molecular beam epitaxy (MBE), lithography technique [1-6] which are widely used in the fabrication of nano-structured materials. A familiar example is realization of a two dimensional electron gas, 2DEG (a thin layer of charges) at the interfaces of two semiconducting heterostructures, such as, GaAs/GaAlAs, where the mean free path of electrons are measured to be about $10\mu\text{m}$ which justifies the term *mesoscopic transport*. This miniaturization of devices has been evoking immense excitement that has gone beyond the realm of a single topic of interest and is considered to be a multidisciplinary research.

On a parallel front, the studies of electron transport through superconductor based junctions (normal metal-superconductor (NS), normal metal-insulator-superconductor (NIS), superconductor-insulator-superconductor (SIS)) have proved to have a great deal of interest owing to the fundamental physics embedded therein, which is further accentuated by the possibility of fabricating devices at small length scales. Recently, SIS junctions have emerged as a viable technology for a range of cryogenic applications which are used wide range of applications such as, high speed digital circuit elements, high-sensitivity detectors of electromagnetic radiation, magnetometers, and quantum computing circuits etc [7-10]. Further, the NIS junctions are also gaining increased attention in modern research to develop nanoscale devices in the field of thermometric, thermoelectric, solid state cooling which received a boost from the recent measurements of the Seebeck coefficient [11-14]. Seebeck effect in junction devices can be used for power generation by converting the waste heat energy into useful power. Further, the thermopower measurements aid in probing the chemistry of the molecular heterojunctions [13]. In Ref. [11, 12] the thermopower or the Seebeck coefficient of molecular junctions between two gold electrodes and the thermopower of atomic-size metallic contacts have been investigated. A growing number of studies of these junction devices in the field of transport, thermometric, thermoelectric, solid state cooling and shot noise have been carried out in details [15-18]. In Ref. [18] an original technique based on controlled oxidation for fabrication of high quality superconducting tunnel junctions between superconducting Al reservoirs and InAs semiconducting nano-wires has been demonstrated where the junctions are shown to have profound applications in low-temperature thermometry and electronic cooling. These are of course very useful in numerous fields of nanoscience

and nanotechnology including sensing, quantum computation etc. In Ref. [15] the authors have presented fabrication of a NIS based refrigerator with an exceptional cooling rate where it was shown that this refrigerator should be able to cool membranes to temperature below $100mK$ starting from a temperature of $300mK$ within $0.1s$. In Ref. [16] shot noise has been studied in superconductor-normal metal (SN) junction between a Niobium (Nb) film and a 2DEG formed in an *InAs* based semiconductor heterostructure. Shot noise is a powerful technique to study the statistics of electron transfer processes which otherwise cannot be obtained from resistance measurements. It also provides the information of the charge of quasiparticles.

Further, the tunneling spectroscopy in an NS junction, which is known as known as Andreev-Saint-James (ASJ) spectroscopy, is one of the most effective tool to investigate the nature (amplitude and the symmetry of the gap) of the superconducting state [19, 20] for unconventional superconductors, such as heavy fermions [21, 22], organic superconductors [23] and high T_c superconductors. To acquire concrete information regarding the symmetry of the order parameter, one needs experiments that are phase-sensitive, such as, the cornerstone experiments of Wollman [24] using superconducting quantum interference device (SQUID) and the experiments by Tsuei and Kirtley [25, 26]. But these experiments have some shortcomings, such as they are not suitable for detecting the existence of a small imaginary component in the order parameter. Further these experiments can only measure the phase difference of the order parameter near the interfaces and are unable to sense the changes of the symmetry between the surfaces and the bulk. Whereas the ASJ spectroscopy is appropriate in overcoming these issues as the Andreev bound-state is very sensitive to the existence of even small imaginary components of the order parameter. In Ref. [19, 20] it is shown that how the ASJ tunneling spectroscopy has been used to probe the cuprate based and iron based superconductors respectively. The fundamental physics in the study of the transport through junction devices, includes probing of the electronic states in the normal metal and thereby acquiring information on the interparticle interaction and the nature of the superconducting gap.

In a normal-superconductor (NS) junction, the low energy transmission is dominated by Andreev reflection [27–29], caused by the conversion of normal current to the super-current which can be described by the familiar Blonder-Tinkham-Klapwijk (BTK) theory [30]. When an electron incidents from a normal metal in a NS junction with an energy lower than the superconducting gap, a cooper pair is injected into the superconducting layer with retroreflecting a hole with spin and velocity opposite to that of the incident electron, a phenomenon known as Andreev reflection (AR). The reflected hole ensures the current conservation as a charge of $2e$ flows across the interface, which, paradoxically results

an increase in the conductance of the junction by a factor of 2 compared to the conductance in the normal-normal junction or at biasing energies much larger than the superconducting gap. The details of this process involves the formation of electron and hole excitations in the superconductor near the interface, which recombine into pairs within the coherence length of the superconductor. In addition to the Andreev reflection, there is of course the normal reflection where the electron is specularly reflected. This we shall term as normal reflection (NR), while it gives vanishing contribution in the low energy spectrum for a perfect NS contact, however it will play (subdominant) a role in our discussion.

Saint-James [31, 32] also studied the charge transport in NS junctions independently of Andreev's work. In 1966 Pankove reported an enhanced electrical conductance at an NS junction below the superconducting gap. His observations on contacts between Al and Nb are as follows: *"When a contact is made between a normal metal and a superconductor, the V-I characteristic of the contact shows an initial region of high conductance with an abrupt change to a region of lower conductance."* [33]. However he did not relate his observations to the works of Andreev or Saint-James [31, 32].

The essential physics governing charge transport through the junction can be captured via a single particle picture described by the BTK theory [30] where a complete theoretical discussion is emphasized, including the effect of an imperfect (not fully transparent) interface, and successfully compared their predictions to the measurements performed on point contacts. The advantage of the BTK formalism is that it can describe different types of contacts ranging from a pure metallic contact to pure tunnel junctions via modeling the barrier potential by an arbitrary strength at the interface. This approach is able to describe several properties of the NS junctions, such as, the charge imbalance generation, the excess current due to the Andreev reflection etc. The essence of the BTK theory is that it is extremely successful though the approach is quite simple. The results of numerous experiments [19, 34–37] can be well described, at least qualitatively, by the BTK theory. Further, to show its applicability to experiments, Blonder and Tinkham applied the BTK theory to the point contact experiments on Nb [38]. In the view of success of the BTK theory to compute the electrical charge current through the NS and NIS junctions, one can employ the formalism to obtain the thermal current and hence compute different thermoelectric properties of the junction devices. For this reason we have adopted this technique to study the properties of different junctions in this thesis.

The violation of the surface inversion symmetry at the interfaces of the junction may induce a special type of spin-orbit coupling, which is known as the Rashba spin-orbit coupling (RSOC) [39]. The Rashba spin-orbit coupling (RSOC) originates due to an effective electric field originating from the potential gradient

across the interface [40, 41]. The RSOC has great importance in the emerging field of spintronics for fabricating novel devices at very small length scales and is very central to our discussion. The possibility of being able to tune the RSOC strength by an external gate voltage or other techniques offers an additional significance [42, 43]. Recently in Ref. [44] it is shown how a double gated structure and a solid electrolyte surrounding the gates have been used to obtain an enhanced RSOC strength. A large number of devices have been proposed based on spin-orbit interaction, for example, the spin field effect transistor [45], and several spin interference based devices [46, 47]. In two dimensional systems, owing to its surface inversion asymmetry, RSOC is found to have large values and hence produces unignorable effects in quantum transport. Since we are going to be interested in conductance properties of two dimensional junction systems, the RSOC will be important for most of our studies. Graphene, owing to its perfect two dimensional nature, is thought to a candidate where RSOC effects could be strong. However the spin gap in a pristine graphene is vanishingly small (a few mev), although there are proposals to enhance this value. We shall discuss them in details in the latter chapters.

In addition to the generic metallic leads, with the adjacent of graphene, fabrication of graphene based junction devices has become fashionable and demands attention. The successful fabrication of graphene [48] has arguably demanded large attention from the condensed matter community than any other topic in the last decade or so owing to its several interesting electronic and transport properties [49–55]. The most interesting feature of the graphene is that its low-energy excitations show massless, chiral, Dirac-like dispersions. This particular low energy dispersion imitates the physics of relativistic particles. As a result, many surprising properties of relativistic physics can be observed in graphene at much smaller speeds that is at Fermi velocity, v_F , 300 times smaller than the speed of light c [56–58]. Further, when a system of such massless fermion is subjected to an external magnetic field, it leads to a new physical phenomenon, for example, the integer quantum Hall effect [50, 51]. Another interesting aspect of Dirac fermions is the Klein tunneling, the indifferent behavior to external electrostatic potentials where the Dirac fermions can be transmitted through a classically forbidden region with probability 1 [58, 59]. In graphene, these electrostatic potentials appear due to presence of disorder and since disorder is integral component in any material, the transport properties of electrons in graphene is a subject of great interest.

In fact, Dirac fermions lead to another interesting phenomenon which is known as Zitterbewegung, or jittery motion of the wave function [60] in presence of a confining potential. It has also been suggested that Coulomb interactions are considerably enhanced in smaller dimensions, such as the graphene quantum

dots [61] which leads to unusual Coulomb blockade effects [62]. The ballistic electronic propagation in graphene is used for fabricating field-effect devices, such as, p-n junctions [63–66], n-p-n junctions [67] etc. The interesting transport properties of graphene allow their usage in a plethora of applications ranging from single molecule detection [68, 69] to spin injection [70–73]. The recent realization of freestanding graphene nano-ribbons (GNRs) [74, 75] has generated renewed interest in carbon-based materials with exotic properties. Quantum Hall effect [48], half metallicity [52, 53], high carrier mobility [54] are the other interesting features that make graphene as a promising candidate for nano-electronics and spintronics applications.

Recently, the thermal and thermoelectric properties of graphene based structures have gained much attention because of the large Seebeck coefficient and high thermal conductivity obtained in graphene sheets [76–78]. Moreover, the superconducting properties can be induced in graphene by possible intercalation with dopant molecules [79] or via proximity effects [80, 81]. Such prospects provide newer scopes of fabricating devices based on hybrid structures of graphene based superconductors.

Apart from the spintronic application point of view, on a theoretical front, C. L. Kane and E. J. Mele [82, 83] proposed two types of spin-orbit couplings (SOC) in graphene, namely the Rashba spin SOC (RSOC) (which arises because of two-dimensional nature) and the intrinsic SOC (ISOC) (a spinless version of which has been proposed by Haldane [84]). The two term, along with a tight-binding dispersion render a P-T symmetric Hamiltonian which has been predicted to beget non-trivial properties. Particularly, it has been inferred that the existence of the spin-orbit terms should be the reason behind realizing a new type of topological state which is known as the quantum spin Hall (QSH) state. But owing to the very small strength of the spin gap (typically $0.01 - 0.05\text{meV}$) [85, 86] in graphene, the QSH state is extremely difficult to realize in experiments. However there are possible methods to induce enhanced SOC strengths in graphene, such as via adatoms [87], using proximity effect of a three dimensional topological insulators [50, 88], by functionalization with methyl groups [89] etc. It is observed that from gold (Au) intercalation at the graphene-Ni interface [90], the RSOC is enhanced up to approximately 100meV . A Rashba splitting about 225meV in epitaxial graphene layers grown on the surface of Ni is obtained in experiments [91].

Motivated by the preceding discussion, we aim to study several interesting features concerning the charge and heat transport properties of spin-orbit coupled superconductor based junctions via modified version of the BTK formalism for both generic and graphene based devices. Since the studies concern electronic transport, it is interesting to compare the two cases as the dispersion of the carriers (electrons) are different, that is parabolic in former and linear (in the

region of interest) for graphene.

In the upcoming sections, we briefly discuss some of the necessary ingredients (or phenomenon) that are used in thesis, such as, the Rashba spin-orbit coupling, Bogoliubov-DeGennes equations, NS and NIS junction, Fabry-Perot oscillations, crystalline structure of graphene, Klein tunneling and finally the Kane-Mele model.

1.1 Spin-orbit coupling

The spin-orbit coupling is actually the interaction of a particle's spin with its motion that causes shifts in its energy levels due to the interaction between the electron's spin and the nucleus magnetic field. Here we provide a back of the envelope derivation of spin-orbit coupling. Since the electric and the magnetic fields undergo a Lorentz transformation as one goes from one inertial frame of reference to another, an electron moving through an electric field of the nucleus experiences a magnetic field in its own inertial frame of reference. The interaction of the electron's spin and the magnetic field arises from the orbital motion is given by the form,

$$E_{int} = -\vec{\mu}_e \cdot \vec{B} \quad 1.1$$

where $\vec{\mu}_e$ is the magnetic moment of the self rotating electron. As $\vec{\mu}_e = -g\mu_B\vec{S}$ (g is gyromagnetic ratio and μ_B is Bohr magneton),

$$E_{int} = g\mu_B\vec{S} \cdot \vec{B} \quad 1.2$$

Since $\vec{B} = \frac{1}{2} \frac{\vec{E} \times \vec{v}}{c^2 \sqrt{1-v^2/c^2}}$ (1/2 is the Thomas correction factor and $\sqrt{1-v^2/c^2}$ is the relativistic factor), the energy corresponding to interaction term gives,

$$E_{SO} = g\mu_B \frac{\vec{E} \times \vec{v}}{2c^2 \sqrt{1-v^2/c^2}} \cdot \vec{S} \quad 1.3$$

Now putting $\vec{S} = \frac{1}{2}\vec{\sigma}$ and $\mu_B = e\hbar/2m$,

$$E_{SO} = \frac{ge\hbar}{8mc^2} \frac{\vec{E} \times \vec{v}}{\sqrt{1-v^2/c^2}} \cdot \vec{\sigma} \quad 1.4$$

with $g = 2$,

$$\begin{aligned} E_{SO} &= \frac{e\hbar}{4mc^2} \frac{\vec{E} \times \vec{v}}{\sqrt{1-v^2/c^2}} \cdot \vec{\sigma} \\ &= \frac{e\hbar}{4m^2c^2} \frac{-\vec{\nabla}V \times \vec{p}}{\sqrt{1-v^2/c^2}} \cdot \vec{\sigma} \end{aligned} \quad 1.5$$

where \vec{E} is related to the electric potential and is given by, $\vec{E} = -\vec{\nabla}V$ and $\vec{v} = \vec{p}/m$ with $\vec{p} = -i\hbar\vec{\nabla}$ is the momentum operator. From the above expression it is understood that if a charged particle moves through a potential gradient, then spin-orbit coupling emerges. The term E_{SO} can be derived by taking the non-relativistic limit of the Dirac equation [92]. In the next section we briefly show a more thorough technique to obtain the spin-orbit coupling starting with relativistic Quantum mechanics for completeness

The Dirac equation is given by the following form,

$$(c\vec{a} \cdot \vec{p} + \beta mc^2 + V) | \psi \rangle = E | \psi \rangle \quad 1.6$$

where a and β are given by,

$$a = \begin{pmatrix} 0 & \vec{\sigma} \\ \vec{\sigma} & 0 \end{pmatrix} ; \beta = \begin{pmatrix} 1 & 0 \\ 0 & -1 \end{pmatrix} \quad 1.7$$

and m , \vec{p} and E are mass, momentum and energy of an electron and V is any spin independent interaction parameter. The wave function Ψ as a two component object can be written as,

$$| \psi \rangle = \begin{pmatrix} \chi \\ \phi \end{pmatrix} \quad 1.8$$

with this, Dirac equation becomes,

$$\begin{pmatrix} E - V - mc^2 & -c\vec{\sigma} \cdot \vec{p} \\ -c\vec{\sigma} \cdot \vec{p} & E - V + mc^2 \end{pmatrix} \begin{pmatrix} \chi \\ \phi \end{pmatrix} = \begin{pmatrix} 0 \\ 0 \end{pmatrix} \quad 1.9$$

This is equivalent to,

$$(E - V - mc^2)\chi - c\vec{\sigma} \cdot \vec{p}\phi = 0 \quad 1.10$$

$$(E - V + mc^2)\phi - c\vec{\sigma} \cdot \vec{p}\chi = 0 \quad 1.11$$

Now combining these two equations by eliminating ϕ one gets,

$$(E - V - mc^2)\chi = c\vec{\sigma} \cdot \vec{p} \left(\frac{1}{E - V + mc^2} \right) c\vec{\sigma} \cdot \vec{p}\chi \quad 1.12$$

On the LHS, $E - mc^2$ is put as E_s , where E_s is the energy from Schrodinger's equation, and on the RHS an approximation is made which is given by,

$$\frac{1}{E - V + mc^2} = \frac{1}{2mc^2} \left(1 + \frac{E_s - V}{2mc^2} \right)^{-1} \approx \frac{1}{2mc^2} - \frac{E_s - V}{4m^2c^4} \quad 1.13$$

The lowest term in this expansion provides the familiar non relativistic Schrodinger equation, whereas keeping the higher order term allows us to see the fine struc-

ture corrections. Now making the substitution in to Eqn.(1.12) we get,

$$E_s \chi = \left(\frac{p^2}{2m} + V - \frac{\vec{\sigma} \cdot \vec{p} (E_s - V) \vec{\sigma} \cdot \vec{p}}{4m^2 c^2} \right) \chi \quad 1.14$$

In order to get rid of the E_s on the RHS, we use the fact that V and $\vec{\sigma}$ commute and that we only need $E_s - V$ to lower (v^2/c^2) order to write,

$$(E_s - V) \vec{\sigma} \cdot \vec{p} \chi = (\vec{\sigma} \cdot \vec{p}) \frac{p^2}{2m} \chi + \vec{\sigma} \cdot [\vec{p}, V] \chi \quad 1.15$$

Hence Eqn.(1.14) becomes,

$$E_s \chi = \left(\frac{p^2}{2m} + V - \frac{p^4}{8m^3 c^2} - \frac{(\vec{\sigma} \cdot \vec{p}) \cdot (\vec{\sigma} \cdot [\vec{p}, V])}{4m^2 c^2} \right) \chi \quad 1.16$$

$$E_s \chi = \left(\frac{p^2}{2m} + V - \frac{p^4}{8m^3 c^2} - \frac{i\vec{\sigma} \cdot \vec{p} \times [\vec{p}, V]}{4m^2 c^2} - \frac{\vec{p} \cdot [\vec{p}, V]}{4m^2 c^2} \right) \chi \quad 1.17$$

The first two terms are just the Hamiltonian for the non relativistic Schrodinger equation. The third term is the relativistic correction to the kinetic energy. We are concerned with the fourth term, the SOC. To analyze the term,

$$(\vec{p}, V) | \psi \rangle = -i\hbar e^2 \frac{\vec{r}}{8\pi^2 \epsilon_0 r^3} | \psi \rangle \quad 1.18$$

The fourth term becomes,

$$\frac{i\vec{\sigma} \cdot \vec{p} \times [\vec{p}, V]}{4m^2 c^2} = \frac{-\hbar e^2}{32\pi^2 \epsilon_0 r^3 m^2 c^2} \vec{\sigma} \cdot \vec{p} \times \vec{r} = \frac{e^2}{8\pi \epsilon_0 r^3 m^2 c^2} \vec{S} \cdot \vec{L} \quad 1.19$$

The above energy depends on the scalar product $\vec{L} \cdot \vec{S}$, where \vec{L} and \vec{S} are the orbital angular momentum and the spins.

There could be three reasons behind the origin of spin-orbit coupling in material. (a) Impurities in the conduction layer which is the main source of SOC in metallic systems. (b) Lack of crystal inversion symmetry where an electron feels an asymmetry in the crystal potential due to the lack of bulk-inversion symmetry. This may cause spin splitting in the conduction band. This is known as Dresselhaus spin-orbit interaction [93]. (c) Lack of surface inversion symmetry in the confinement potential of electrons which may occur in a quantum well or a heterostructure. When the motion of electron is confined to two dimensions, for example in quantum wells, an asymmetric confinement potential gives rise to another type of SOC which is known as Rashba spin-orbit coupling (RSOC) [94].

1.2 Rashba spin-orbit coupling

In solids, quasi free electrons do not feel the strong attraction of the nucleus of their host atoms. However the electrons still may experience an electric field or a potential gradient due to internal effects. As we know, if the electrons experience a strong electric field of potential gradient, then there is possibility of emerging of a spin-orbit coupling. So if a potential gradient exists across the interface due to the structural inversion asymmetry, there will be a spin-orbit coupling and named after its discoverer, E.I. Rashba, that is, Rashba spin-orbit coupling (RSOC) [94]. The importance of the RSOC lies in the fact that asymmetry in the confinement potential can be varied by electrostatics means, allowing one to tune the RSOC strength by an external gate voltage. The strength of RSOC depends also on the crystal composition in quantum wells, and is largest for narrow gap III – V semiconductors, such as InAs and InGaAs etc. In the following subsection we shall describe the RSOC in a continuum model. Later on we shall also incorporate it in graphene.

A priori, RSOC yields electrons with same wave vector and different spins to have different energies. Further it leads to orientation of spins which points perpendicular to the direction of the electron propagation wave vector. The free particle Hamiltonian including RSOC is described by the following Hamiltonian [94],

$$\begin{aligned} H_R &= - \frac{ge\hbar}{8m^2c^2} \vec{\nabla}V \cdot (\vec{p} \times \vec{\sigma}) \\ &= a\hat{n} \cdot (\vec{p} \times \vec{\sigma}) \end{aligned} \quad 1.20$$

where $a = -\frac{ge\hbar}{8m^2c^2}E$ is the strength of the RSOC, $\vec{\sigma}$ is a vector of Pauli spin matrices, $\vec{E} = -\vec{\nabla}V$ is electric field along \hat{n} direction, and $\vec{p} = -i\hbar\vec{\nabla}$ is momentum operator. In the absence of any Zeeman coupling, assuming elastic scattering and for $\hat{n} = \hat{z}$ (as per convention), the total Hamiltonian for the electron is given by,

$$H = \frac{p^2}{2m} + a(\vec{p} \times \vec{\sigma}) \cdot \hat{z} = \frac{p_x^2 + p_y^2}{2m} + a(\sigma_x p_y - \sigma_y p_x) \quad 1.21$$

This Hamiltonian yields the following energy spectrum [95, 96],

$$E(k) = \frac{\hbar^2 k^2}{2m} \pm a\hbar|k| \quad 1.22$$

where $|k|$ is the modulus of electron momentum with plus and minus signs denote two possible spin directions. The associated wave functions are related to the

eigenvectors of the Hamiltonian and are given by the following form,

$$\Psi_{\pm}(x, y) = e^{i(k_x x + k_y y)} \frac{1}{\sqrt{2}} \begin{pmatrix} 1 \\ \pm i e^{-i\vartheta} \end{pmatrix} \quad \text{1.23}$$

where $\vartheta = \tan^{-1}(k_y/k_x)$. It is easily understood that the spin states are always perpendicular to the direction of motion (see Eqn.(1.23)). If an electron moves along the x -direction the spinor part of the eigenvector becomes $(1; \pm i)$, that is, the spin up and the spin down are locked in y direction. By contrast, if the electron moves along the y direction, the eigenvectors become $(1, \pm 1)$, that is, the spin up and the spin down states are constrained in the x direction (see Fig.(1.1)).

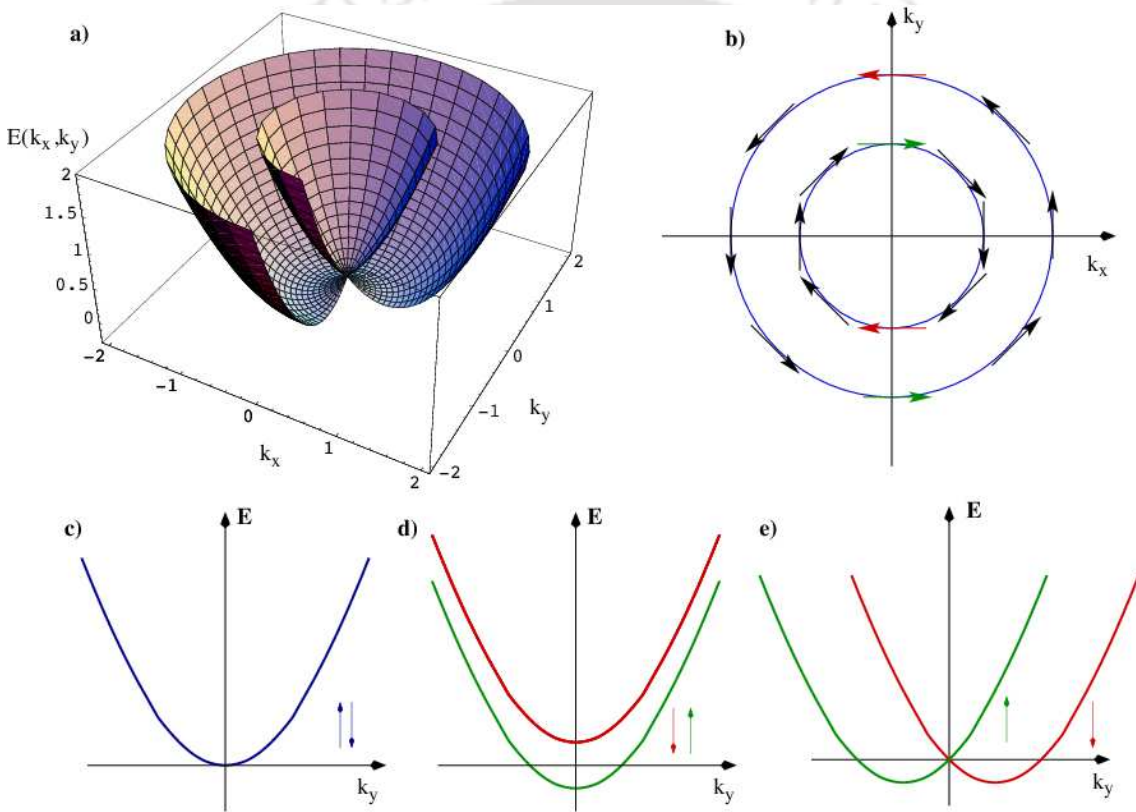


Figure 1.1: (a) Three-dimensional energy spectrum of the Hamiltonian H (Eqn.(1.21)). (b) The Fermi energy contours for the Hamiltonian H . (c) Energy spectrum for a free electron. (d) Energy spectrum for an electron in presence of a magnetic field (Zeeman splitting). (e) Energy spectrum for an electron in presence of Rashba spin-orbit coupling. Courtesy Ref.[96].

In Fig.(1.1(c-e)), the k_y -section of the energy spectra as a function of momentum for a 2DEG are plotted in different physical conditions which are explained in the following. Fig.(1.1c) is related to a free electron in 2DEG where the spin degeneracy is present. Fig.(1.1d) represents the energy spectrum for an electron in presence of a magnetic field \vec{B} , the spin degeneracy is lifted by the Zeeman splitting and the gap separating spin up and spin down bands is equal to $g\mu_B B$

where g is the Bohr magneton. Fig.(1.1e) presents a one dimensional view of the energy spectrum for an electron in presence of RSOC. The spin degeneracy is lifted up except for $k_y = 0$. In this situation, the degeneracy is removed without opening of any gap.

1.3 Bogoliubov-deGennes equations

After the discovery of the superconducting state in 1911 [97], the field of superconductivity has drawn tremendous attention both theoretically and experimentally. In the 1950s there was a great deal of attempt to establish a theory that would enable to explain the phenomenon of superconductivity. In 1957 John Bardeen, Leon Neil Cooper, and John Robert Schrieffer (BCS) proposed a microscopic theory of superconductivity [97] which is quite successful to interpret different properties, such as, the superconducting energy gap, the transition temperature, the heat capacity, the Meissner effect [98] and the penetration depth [99] for a class of superconductors that entail singlet pairing and phonon mediated superconducting correlations with low transition temperature ($T_c \leq 25K$). These are often referred to as conventional superconductor. For these conventional (weak coupling) superconductors, the predictions of BCS theory are quite successful. For example, the tunneling experiments in Ref. [100] shows that the superconducting energy gap follows the BCS ratio $2\Delta/k_B T_c \sim 3.52$ (where Δ_0 is the energy gap at $T = 0K$, k_B is the Boltzmann constant and T_c is the transition temperature). In the discussion below, we shall provide a brief account of the Bogoliubov-deGennes (BdG) equations that describe superconducting condensate and has been used by us extensively in this thesis.

The BdG equations are the meanfield equations for the superconducting systems. They are obtained as the equations of motion for the meanfield approximation of BCS Hamiltonian. In the following we will derive the BdG equations. The Hamiltonian H is given by [101],

$$H = H_0 + H_1 \quad 1.24$$

where H_0 is the kinetic energy operator and H_1 is the interaction energy operator.

$$H_0 = \int dr \sum_{\sigma} \Psi_{\sigma}^{\dagger}(r) \left[\frac{1}{2m} \left(-i\hbar\nabla - \frac{eA}{c} \right)^2 + U_0(r) - \mu \right] \Psi_{\sigma}(r) \quad 1.25$$

$$H_1 = -\frac{1}{2}V \int dr \sum_{\sigma\sigma'} \Psi_{\sigma}^{\dagger}(r)\Psi_{\sigma'}^{\dagger}(r)\Psi_{\sigma'}(r)\Psi_{\sigma}(r) \quad 1.26$$

where m is the mass of the quasiparticles, A is the vector potential, e is the electronic charge, c is the speed of light, $U_0(r)$ is an external potential which

may be present due to the impurities, μ is the chemical potential, σ denotes the spin direction and V is considered to be a constant (BCS approximation) which denotes the net interaction between quasiparticles (pairing interaction and Coulomb interaction). The Ψ and Ψ^\dagger are the annihilation and the creation field operators.

H_1 in Eqn.(1.26) is replaced by a bilinear form according to the mean field decomposition. This provides an effective Hamiltonian which is given by,

$$H_{eff} = \int dr \left[\sum_{\sigma} \Psi_{\sigma}^{\dagger}(r) H_0 \Psi_{\sigma}(r) + U(r) \Psi_{\sigma}^{\dagger}(r) \Psi_{\sigma}(r) + \Delta(r) \Psi_{\uparrow}^{\dagger}(r) \Psi_{\downarrow}^{\dagger}(r) + \Delta(r)^* \Psi_{\downarrow}(r) \Psi_{\uparrow}(r) \right] \quad 1.27$$

where $U(r)$ is the Hartree-Fock averaged Coulomb potentials. $\Delta(r)$ is the pairing potentials and $\Delta(r)^*$ is its h.c.

We wish to make a transformation to a basis such that the Hamiltonian is diagonal, i.e.,

$$H_{eff} = E_0 + \sum_{n\sigma} \epsilon_n \gamma_{n\sigma}^{\dagger} \gamma_{n\sigma} \quad 1.28$$

E_0 is the ground state energy, and ϵ_n is the energy of the quasiparticle excitation in state n . The operators $\gamma_{n\sigma}$ and $\gamma_{n\sigma}^{\dagger}$ are the annihilation and creation operators of the quasiparticles. The quasiparticle operators must obey the fermion anti-commutation relations which are given by,

$$\{\gamma_{m\sigma}, \gamma_{n\sigma'}^{\dagger}\} = \delta_{mn} \delta_{\sigma\sigma'} \quad ; \quad \{\gamma_{m\sigma}, \gamma_{n\sigma'}\} = 0 \quad ; \quad \{\gamma_{m\sigma}^{\dagger}, \gamma_{n\sigma'}^{\dagger}\} = 0 \quad 1.29$$

The transformation which diagonalizes the mean-field Hamiltonian in the Bogoliubov-Valatin transformation and gives the electron annihilation and creation operators in terms of quasiparticle operators are given by,

$$\begin{aligned} \Psi_{\uparrow}(r) &= \sum_n \left[\gamma_{n\uparrow} u_n(r) - \gamma_{n\downarrow}^{\dagger} v_n^*(r) \right] \quad ; \quad \Psi_{\downarrow}(r) = \sum_n \left[\gamma_{n\downarrow} u_n(r) + \gamma_{n\uparrow}^{\dagger} v_n^*(r) \right] \quad 1.30 \\ \Psi_{\uparrow}^{\dagger}(r) &= \sum_n \left[\gamma_{n\uparrow}^{\dagger} u_n^*(r) - \gamma_{n\downarrow} v_n(r) \right] \quad ; \quad \Psi_{\downarrow}^{\dagger}(r) = \sum_n \left[\gamma_{n\downarrow}^{\dagger} u_n^*(r) + \gamma_{n\uparrow} v_n(r) \right] \end{aligned}$$

The commutator $[\Psi_{\sigma}(r), H_{eff}]$ using the anti-commutation rules of the operators $\Psi_{\sigma}(r)^{\dagger}$ and $\Psi_{\sigma}(r)$ yields,

$$\begin{aligned} [\Psi_{\uparrow}(r), H_{eff}] &= [H_0 + U(r)] \Psi_{\uparrow}(r) + \Delta(r) \Psi_{\downarrow}^{\dagger}(r) \quad 1.31 \\ [\Psi_{\downarrow}(r), H_{eff}] &= [H_0 + U(r)] \Psi_{\downarrow}(r) - \Delta^*(r) \Psi_{\uparrow}^{\dagger}(r) \end{aligned}$$

Using the Bogoliubov transformations as in Eqn.(1.30) to the Eqn.(1.31) and Eqn.(1.28), a pair of equations is obtained by which one can derive the Bogoliubov

equations by comparing the coefficients of quasiparticle operators γ_n and γ_n^\dagger ,

$$Eu(r) = [H_0 + U(r)]u(r) + \Delta(r)v(r) \quad 1.32$$

$$Ev(r) = -[H_0^* + U(r)]v(r) + \Delta^*(r)u(r)$$

These equation can be written in a matrix form as,

$$\begin{pmatrix} H_0 + U(r) & \Delta(r) \\ \Delta^*(r) & -H_0 - U(r) \end{pmatrix} \begin{pmatrix} u(r) \\ v(r) \end{pmatrix} = E \begin{pmatrix} u(r) \\ v(r) \end{pmatrix} \quad 1.33$$

The self consistency equation for $U(r)$ and $\Delta(r)$ are given by [101],

$$U(r) = -V \langle \Psi_\uparrow^\dagger(r) \Psi_\downarrow(r) \rangle = -V \sum_n [|u_n(r)|^2 f_n + |v_n(r)|^2 (1 - f_n)] \quad 1.34$$

$$\Delta_r = V \langle \Psi_\uparrow(r) \Psi_\downarrow(r) \rangle = V \sum_n v_n^* u_n(r) (1 - f_n)$$

where f_n is the Fermi-Dirac distribution and is given by,

$$f_n = \frac{1}{\left(1 + e^{\frac{E_n - \mu}{k_B T}}\right)} \quad 1.35$$

where μ is the chemical potential.

1.4 Normal metal and superconductor junction: Andreev reflection

The contact between a normal metal and a superconductor can be different of types - a direct contact junction of a normal metal and a superconductor (NS) or a tunneling junction in which there is presence of an insulating region between the normal metal and the superconducting material (NIS). It is considerably very hard to make a direct contact NS junction with a clean interface (no potential barrier and impurities). The tunnel junction, that is, an insulating layer between the metallic and superconducting material (therefore NIS) is usually the consequence of a naturally occurring oxide on a metal surface, but it can also be artificially produced. Fig.(1.2) shows the schematic diagram of the NS and NIS junctions.

In these junctions the sub-gap transport (for the energies $E < \Delta$) are mainly dominated by the Andreev reflection. Andreev reflection (AR) is a process where an incoming electron gets reflected from the interface of the NS junction as a hole, nearly retracing the trajectory of the incoming electron and subsequently a Cooper pair is generated at the Fermi level of the superconductor (see Fig.(1.3)). This type of reflection is known as retroreflection. Since at the energies below

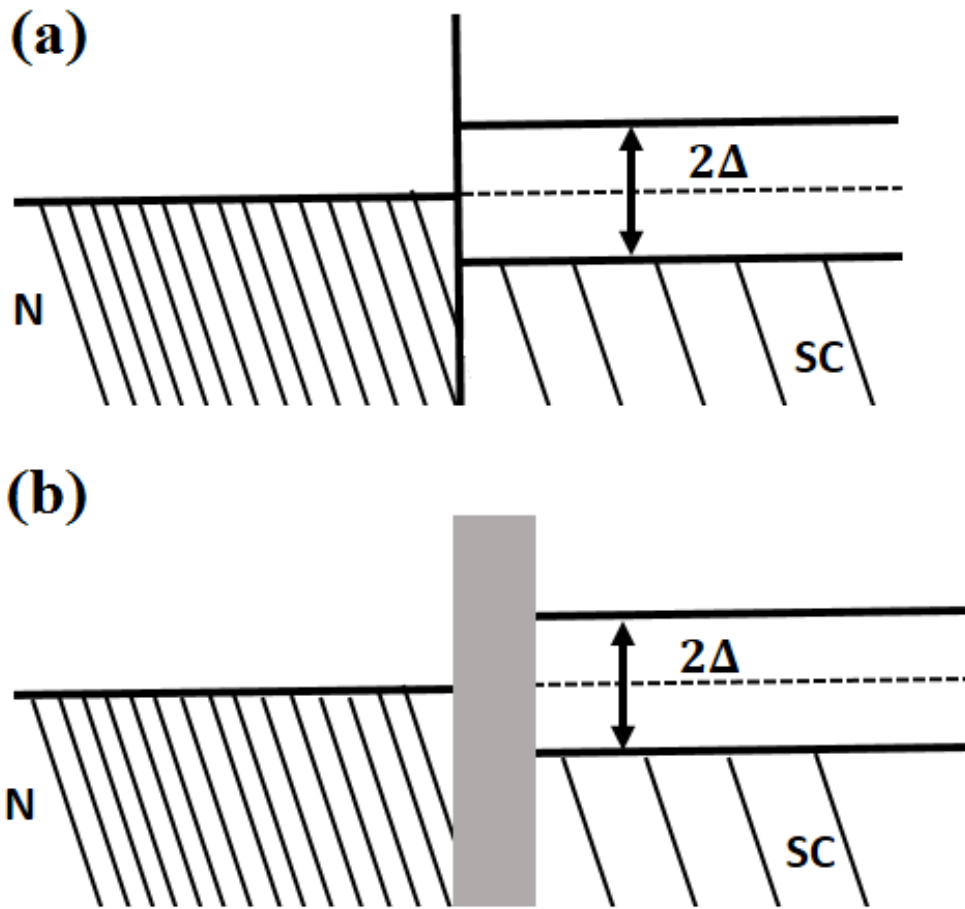


Figure 1.2: (a) NS and (b) NIS junction. Dashed regions are occupied states. Grey block in (b) is an interface barrier. Courtesy Ref.[102].

the superconducting gap and $T = 0$, only pairs exist in superconducting side, this is the only mechanism which transfer the charges in superconducting in this energy range. This effect was first studied by Andreev [27, 28] in order to explain the anomalous heat conduction properties at NS contact.

For a finite barrier at the NS interface, a particle with $E < \Delta$ can also specularly reflect back to the normal side from the interface whereas the particles with energy $E > \Delta$ can easily transmit as electron-like or hole-like quasiparticles into the superconducting side. The details of transport phenomena for both the NS and NIS junction will be discussed via BTK theory in the next chapter. Here we shall specify how the components of the velocity changes corresponding to different processes that take place at the interface. They are following (see Fig.(1.4)).

- (i) Specular reflection: $v_{\perp} \rightarrow -v_{\perp}, v_{\parallel} \rightarrow v_{\parallel}$
- (ii) Andreev reflection: $v_{\perp} \rightarrow -v_{\perp}, v_{\parallel} \rightarrow -v_{\parallel}$
- (iii) Transmission as an electron: $v_{\perp} \rightarrow v_{\perp}, v_{\parallel} \rightarrow v_{\parallel}$
- (iv) Transmission as a hole: $v_{\perp} \rightarrow v_{\perp}, v_{\parallel} \rightarrow -v_{\parallel}$

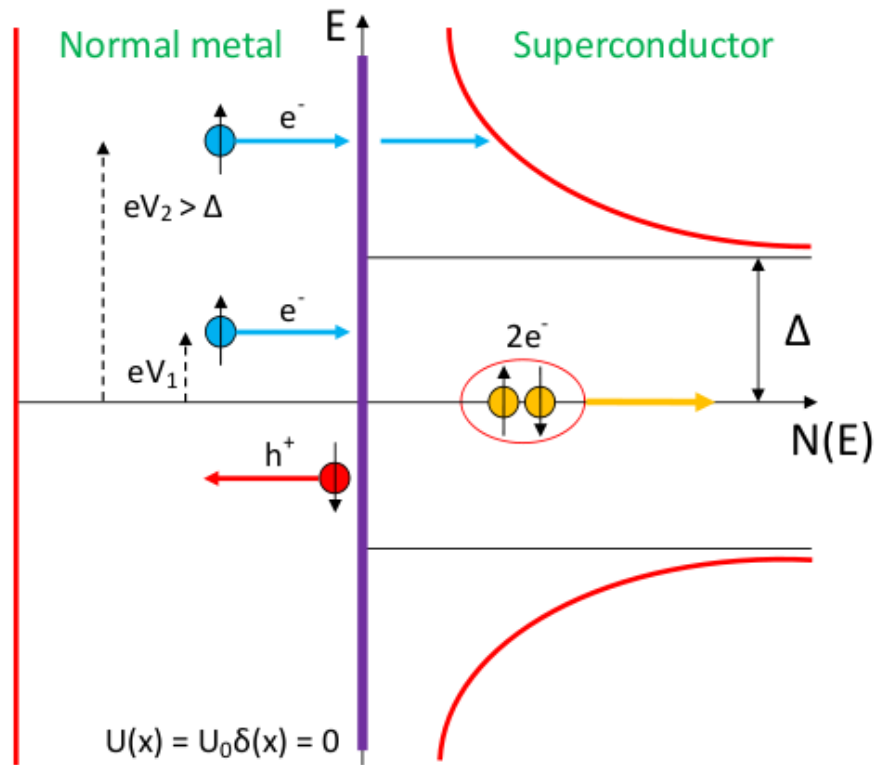


Figure 1.3: *Electrical transport at an NS junction. The motion of electrons (e^-) and holes (h^+) and their respective spin (\uparrow , \downarrow) are indicated. The Cooper pair at the Fermi energy, the superconducting gap Δ , and the superconducting density of states are shown. Courtesy Ref.[20].*

One should keep in mind that the parallel component of the momentum is conserved in all the four processes listed above. Only the momentum of the hole is opposite to its direction of propagation.

In case of NS junction (no impurities at the interface), Andreev reflection has the spectacular consequences for the low-energy electrical transport. As emphasized earlier, even if an electron incident with an energy $E < \Delta$ from the metallic side, one still obtains a significant current in the superconducting lead. But in case of an NIS junction the low energy transmission is greatly suppressed because of the specular reflection. In Fig.(1.5) it is shown how the transmission takes place in case of NIS junction where the following processes occur [102]:

- (i) Specular reflection: electron reflects back to the normal side from the normal-insulator (NI) interface.
- (ii) P1: Propagation to the insulating barrier, AR at the insulator-superconductor (IS) interface, transmission to normal side.
- (iii) P2: Transmission to insulator, AR at IS interface, specular reflection at NI interface, AR at IS interface, transmission to normal side.

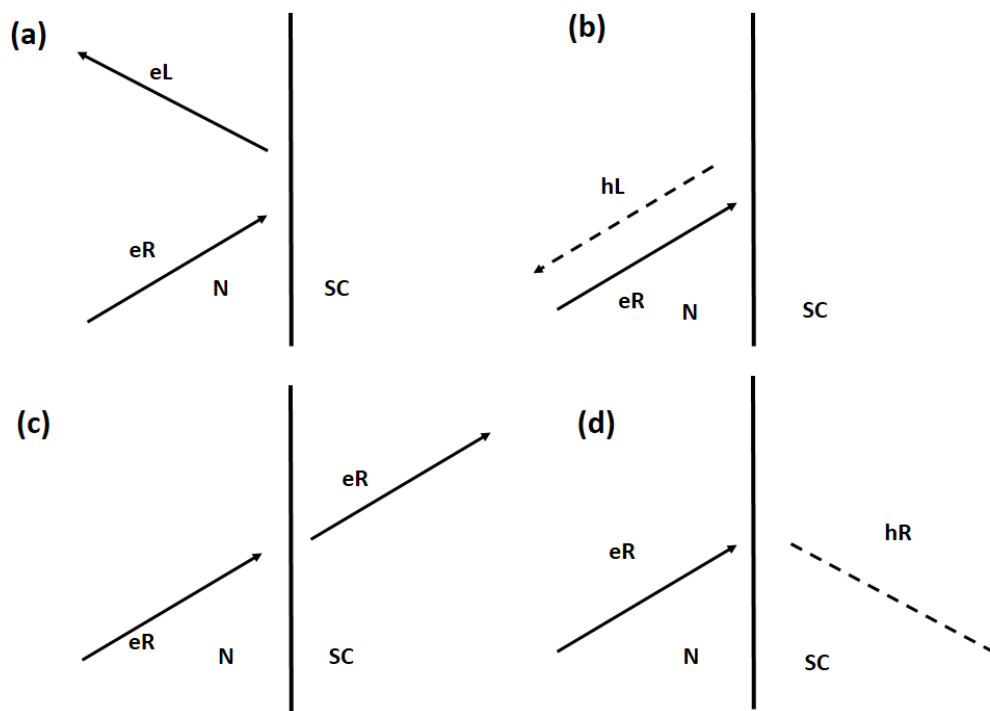


Figure 1.4: Four processes at NS interface are shown, namely, (a) specular reflection, (b) Andreev reflection, (c) transmission as an electron, (d) transmission as a hole. Arrows point in a direction towards the velocity of the particle, and abbreviations for the directions are: eR - a right moving electron, eL - a left moving electron, hR - a right moving hole, hL - a left moving hole. Full lines denote electron trajectories, dashed lines denote hole trajectories. Courtesy Ref.[102].

(iv) P3: Transmission to insulator, AR at IS interface, specular reflection at NI interface, AR at IS interface, specular reflection at NI interface, AR at IS interface, transmission to normal side.

So it is clear that the processes with an odd number of AR transfer a hole back to the normal side (see Fig.(1.5)), and thus account for an AR by transferring charge $2e$ to the superconducting side. Whereas the processes with an even number of AR transfer an electron back to the normal side, and thus provide an overall effect of specular reflection or what we call as normal reflection (NR). As AR has positive contribution and NR has negative contribution to the conductance from normal side to superconducting side, and some of the electrons that get through the barrier reflect back as holes (Andreev reflection) and some of them reflect back as electrons (normal reflection), the conductance will not be 2 at zero bias voltage.

Here, for completeness, we describe the techniques for fabricating the tunnel junctions. There are several methods available for creating the contacts between two materials, such as, needle-anvil [103], shear method [104], lithography [105],

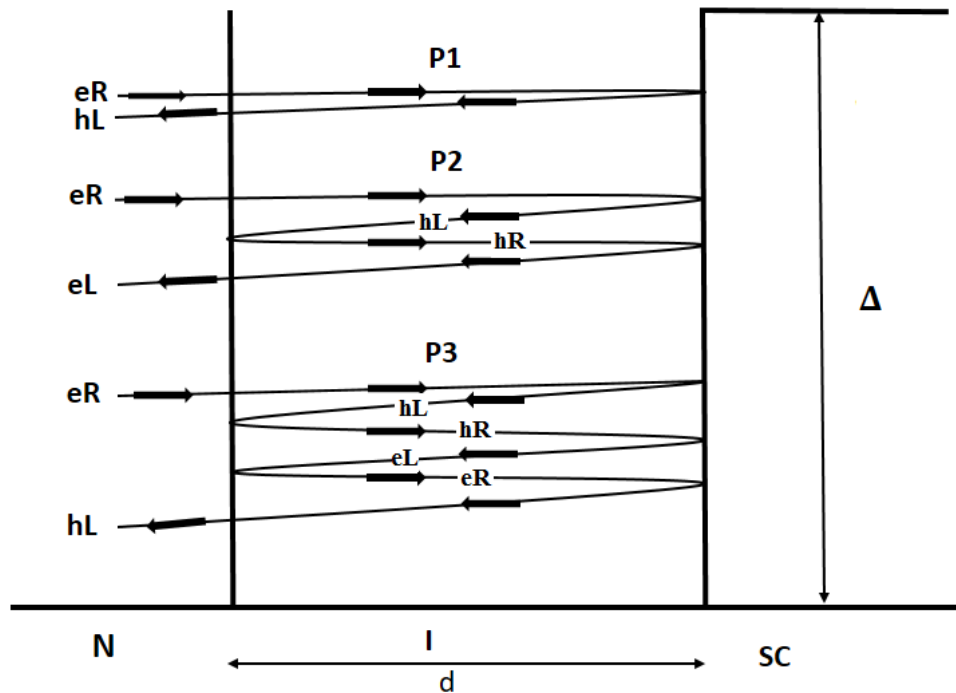


Figure 1.5: NIS junction with the possible trajectories after AR at the superconducting interface. The nomenclature is same as in Fig.(1.4). Courtesy Ref.[102].

break junctions etc [106]. We elaborate on two of them here. In a needle-anvil method a sharp tip is made by mechanically cutting a wire of the material of interest and then it is engaged slowly on a foil or film of the other sample to form a very sharp point contact between them. This is mainly done by moving the sharp tip which is controlled by a 100 threads per inch, differential screw rotated by a stepper motor. Naturally, either the tip or the surface of the sample has an insulating layer present on it. The insulating layer can be modified using large electrical pulse that causes the local breakdown of the layer. To achieve a good point contact, the sample surface should be very smooth which is mainly done by rubbing the surface with very fine emery paper and then by alumina powder of very small grain size. Further in Ref.([18]) it is described how a high quality tunnel junctions between the superconducting Al reservoirs and InAs nanowires are made by multiple steps of electron beam lithography, evaporation, and controlled in situ oxidation. Here we will highlights few steps followed by them. The InAs nanowires [107] are grown via chemical beam epitaxy method and then passivated by using a $(NH_4)_2S_x$ solution [108] to remove the native oxide. Then the sample was transferred to the vacuum chamber of an electron-beam evaporator, where a 5/50nm thick layer of Ti/AlMn was evaporated. The reason behind using the Mn impurities in the alloy was to quench the superconductivity in the Al-based

layer [109] such that it can develop a thin normal metal interlayer between the oxide barrier on top of it and the InAs crystal. Subsequently it was transferred to an oxidation chamber, where the AlMn layer was exposed to 0.2–0.4 Torr of O_2 for 5 min to create a 1–2 nm thick oxide layer. After the oxidation method, a residual AlMn layer of approximately 50 nm thickness remained as a buffer between the oxide and the InAs. Finally, a layer of superconductive Al of thickness 50 nm was deposited on top of AlO_x .

1.5 Normal-insulator-superconductor junction and Fabry-Perot-like oscillations

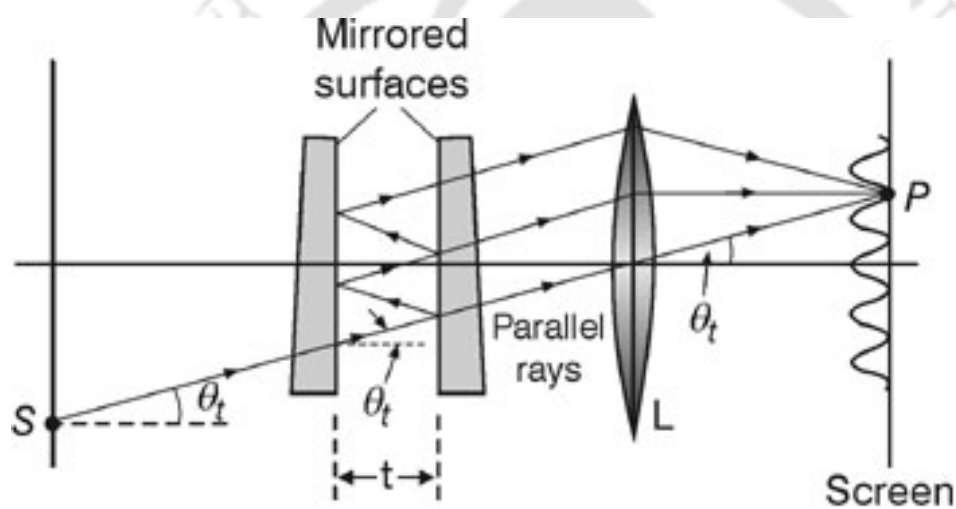


Figure 1.6: Schematic of Fabry-Perot interferometer

In the context of NIS junctions here we shall briefly discuss about the Fabry-Perot oscillations. In the Fabry-Perot interferometer the phenomenon of multiple beam interference takes place when light propagates through a cavity bounded by two partial reflective parallel surfaces (see Fig.(1.6)). Each time the light reaches one of the surfaces, a portion of the light is reflected back, and the remaining part is transmitted. Thus a single beam breaks into multiple beams which interfere with each other. All such transmitted light rays interfere with each other to give rise to a maxima or minima in the intensity spectrum depending on the path difference between them. It can be shown that if the optical path difference between two neighbouring rays is an even multiple of the wavelength of the light, then the intensity of the resultant transmitted light is maximum and for an odd multiple case, the intensity is minimum. As the path difference between the two neighbouring rays depend on the number of reflections at the two surfaces and

the distance between the two surfaces, the intensity of transmitted wave will show an oscillating nature as a function of the distance between the two surfaces that controls the phase matching condition. Further if we fix the distance between the surfaces and vary the wavelength of the light, the same oscillations in the intensity spectrum of the transmitted light can be obtained.

Similarly in the case of an NIS junction (obviously with an external gate voltage across the insulating layer which helps in transmission across the insulating layer) the electrons which behave as waves, undergo multiple reflections back and forth from the two interfaces (NI and IS) along the insulating region (see Fig.(1.5)). Each time the electron reaches one of the surfaces, it can reflect back, and also it can transmit. All such transmitted electron waves interfere with each other and yield a maxima or minima in the conductance characteristics depending on the mutual path difference between them. For example, the path difference between the electrons following path P1 and P3 is $4d$ (see Fig.(1.5)) for four extra reflections (d is the width of the insulating region). The quantum interference occurs when such a round trip becomes a multiple of the wavelength of the electron. So in this case also if we vary the width of the insulating layer or alternately, the wavelength of the electron, the conductance will show the oscillations.

1.6 Basics of Graphene

Here we give a brief account of graphene owing to its importance in our thesis. Graphene is made of a single layer of sp_2 bonded carbon atoms that are packed in the honeycomb form of a crystal lattice. Graphene denotes a new class of materials that are only one atom thick (so thickness can be considered to be zero) and called as two-dimensional (2D) materials. It was first experimentally realized only a decade ago [48]. The unique geometrical structure of graphene has attracted a great attention to be used as a future electronic material, because of its extraordinary properties, such as, high current density, high thermal conductivity, chemical inertness, optical transmittance and super hydrophobicity [62, 110]. This list of astonishing properties of graphene, make it suitable for a wide range of applications starting from electronics to optics, sensors, and bio-devices. The intriguing characteristics of graphene originate from π electrons of $2p$ orbitals that delocalize over the sheet of carbon atoms while the strong σ bonds are responsible for the honeycomb geometry.

Now we describe the graphene geometry mathematically. It can easily be seen that the honeycomb lattice of graphene is not a Bravais lattice because of two neighbouring sites being non-equivalent. It is actually the union of two triangular Bravais lattices which are conventionally denoted as A and B sublattices. From Fig.(1.7) it is clear that a carbon atom on the A sublattice has nearest neighbours

(NN) towards right, lower-left and upper-left which belong to the B sublattice, whereas an atom on the B sublattice has NN in the directions left, upper-right, and lower-right which belong to the A sublattice. The primitive lattice vectors of

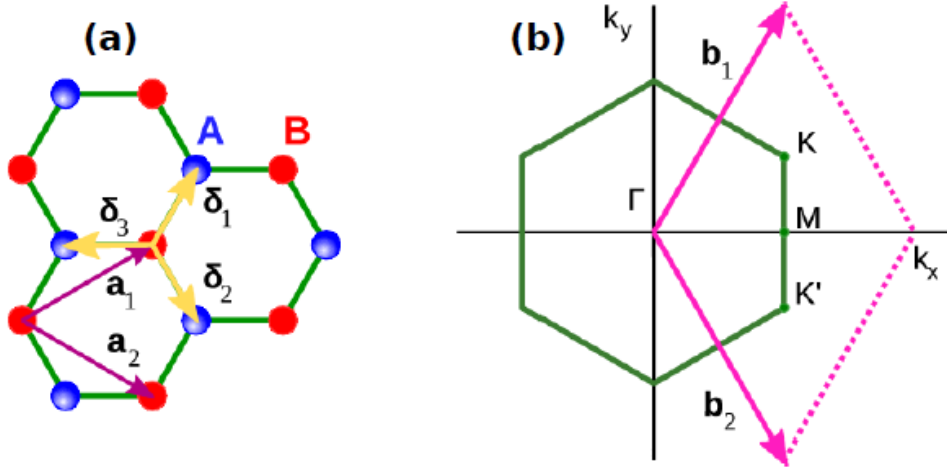


Figure 1.7: (a) Honeycomb lattice structure of graphene. The vectors $\vec{\delta}_1$, $\vec{\delta}_2$ and $\vec{\delta}_3$ connect NN carbon atoms. The vectors \vec{a}_1 and \vec{a}_2 are the basis vectors. (b) First Brillouin zone (BZ) of the honeycomb lattice. Its primitive lattice vectors are \vec{b}_1 and \vec{b}_2 .

graphene can be written as Fig.(1.7a),

$$\vec{a}_1 = \frac{3a}{2} \left(\hat{x} + \frac{1}{\sqrt{3}} \hat{y} \right) ; \quad \vec{a}_2 = \frac{3a}{2} \left(\hat{x} - \frac{1}{\sqrt{3}} \hat{y} \right) \quad 1.36$$

The reciprocal lattice vectors Fig.(1.7b) are given by,

$$\vec{b}_1 = \frac{2\pi}{3a} \left(\hat{x} + \sqrt{3} \hat{y} \right) ; \quad \vec{b}_2 = \frac{2\pi}{3a} \left(\hat{x} - \sqrt{3} \hat{y} \right) \quad 1.37$$

The three nearest neighbour vectors in real space are,

$$\vec{\delta}_1 = \frac{a}{2} \left(\hat{x} + \sqrt{3} \hat{y} \right) ; \quad \vec{\delta}_2 = \frac{a}{2} \left(\hat{x} - \sqrt{3} \hat{y} \right) ; \quad \vec{\delta}_3 = -a \hat{x} \quad 1.38$$

For the electronic band structure of graphene, we directly work in second quantized notation, where a tight binding model with nearest neighbour hopping only has been considered. If we denote the lattice sites by an index, i and the corresponding creation operator by $a_{i\sigma}^\dagger$ ($b_{i\sigma}^\dagger$) for an atom on the A(B) sublattice, the nearest neighbour tight binding Hamiltonian acquires following form,

$$H = -t_1 \sum_{\langle i,j \rangle} \left(a_{i\sigma}^\dagger b_{j\sigma} + H.c. \right) \quad 1.39$$

Applying the following Fourier transformation to the above Hamiltonian,

$$a_i = \frac{1}{\sqrt{N}} \sum_k a_k e^{-i\vec{k}\cdot\vec{r}} ; \quad b_i = \frac{1}{\sqrt{N}} \sum_k b_k e^{-i\vec{k}\cdot\vec{r}} \quad 1.40$$

One gets,

$$\begin{aligned} H &= -t_1 \sum_k a_k^\dagger b_k (e^{-i\vec{\delta}_1\cdot\vec{k}} + e^{-i\vec{\delta}_2\cdot\vec{k}} + e^{-i\vec{\delta}_3\cdot\vec{k}}) \\ &\quad - t_1 \sum_k b_k^\dagger a_k (e^{i\vec{\delta}_1\cdot\vec{k}} + e^{i\vec{\delta}_2\cdot\vec{k}} + e^{i\vec{\delta}_3\cdot\vec{k}}) \\ &= \sum_k \begin{pmatrix} a_k^\dagger & b_k^\dagger \end{pmatrix} \begin{pmatrix} 0 & f(k) \\ f^*(k) & 0 \end{pmatrix} \begin{pmatrix} a_k \\ b_k \end{pmatrix} \end{aligned} \quad 1.41$$

where

$$\begin{aligned} f(k) &= -t_1 (e^{-i\vec{\delta}_1\cdot\vec{k}} + e^{-i\vec{\delta}_2\cdot\vec{k}} + e^{-i\vec{\delta}_3\cdot\vec{k}}) \\ &= -t_1 (e^{ik_x a} + e^{-ik_x a/2} 2 \cos(\sqrt{3}ak_y/2)) \end{aligned} \quad 1.42$$

$$\begin{aligned} f^*(k) &= -t_1 (e^{i\vec{\delta}_1\cdot\vec{k}} + e^{i\vec{\delta}_2\cdot\vec{k}} + e^{i\vec{\delta}_3\cdot\vec{k}}) \\ &= -t_1 (e^{-ik_x a} + e^{+ik_x a/2} 2 \cos(\sqrt{3}ak_y/2)) \end{aligned} \quad 1.43$$

Finally, the energy eigenvalues are given by,

$$E_k = \pm \sqrt{f(k)f^*(k)} = \pm t_1 \sqrt{(3 + 2 \cos(\sqrt{3}k_y a) + 4 \cos(\sqrt{3}k_y a/2) \cos(3k_x a/2))} \quad 1.44$$

The two energy bands touch at six points in the first Brillouin zone. We would like to identify these points which can be obtained from the condition $f(k) = 0$. It can be shown that there is six points where $f(k) = 0$. Only two of these six points are inequivalent and they are generally referred to as the K and K' points. The K and K' points are given by,

$$\vec{K} = \left(0, \frac{4\pi}{3\sqrt{3}a}\right) ; \quad \vec{K}' = \left(0, -\frac{4\pi}{3\sqrt{3}a}\right) \quad 1.45$$

Since we would like to focus on the low energy transmission characteristics in graphene based junction devices, we expand the Hamiltonian around each of these points. A Dirac-like (linear) energy dispersion is obtained near these K and K' points. The shape of the resulting band structure is shown in Fig.(1.8).

1.7 Klein tunneling in graphene

In 1929, physicist Oskar Klein [111] obtained a surprising result by applying the Dirac equation for a step potential. In a non-relativistic quantum mechanical

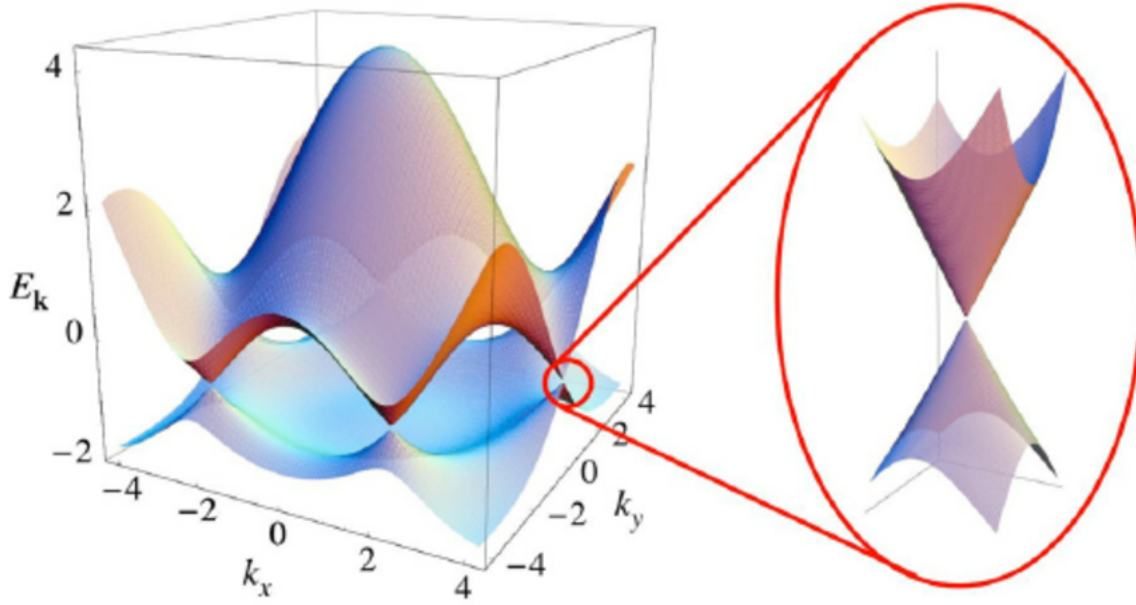


Figure 1.8: *Electronic band structure of graphene. Left: energy spectrum (in units of nearest neighbour hopping strength, t_1). Right: enlarged view of the energy bands close to one of the Dirac points. Courtesy of Ref.[49].*

sense, an electron tunneling into a large barrier can be realized, with exponential damping. However, according to Klein's result, when the potential barrier approaches to infinity, the barrier is almost transparent to the incident Dirac particle. As a result, the transmitted current will not vanish. As in this thesis, the conductance properties of the graphene based NIS (though the insulating layer has been modeled in a different way) junction has been studied, here we shall briefly discuss the Klein tunneling phenomenon in graphene.

The equation of motion for the massless Dirac particle is given by,

$$-i v_F \vec{\sigma} \cdot \vec{\nabla} \psi(r) = E \psi(r) \quad 1.46$$

which is also known as the Weyl equation. The solution of Eqn.(1.46) (neglecting the normalization factor) is given by,

$$\psi^\pm(r) = \begin{pmatrix} 1 \\ \pm e^{i\phi} \end{pmatrix} e^{i(k_x x + k_y y)} \quad 1.47$$

where \pm denotes the positive and negative energy solutions and $\phi = \tan^{-1}(k_x/k_y)$. Now consider a plane wave described by Eqn.(1.47) is made to incident from left ($x < 0$) to an energy barrier, as represented in Fig.(1.9a). Now we shall find out the tunneling coefficient through the barrier for low energies, that is, $E < V_0$. The

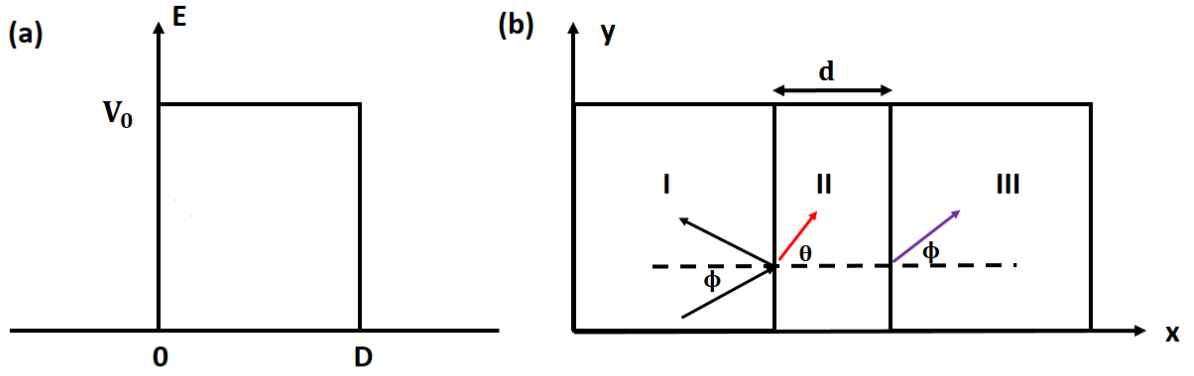


Figure 1.9: (a) An energy barrier with width d and height V_0 , (b) Three regions in this problem.

wave functions in three different regions Fig.(1.9b) are given by,

$$\psi_I(r) = \begin{pmatrix} 1 \\ e^{i\phi} \end{pmatrix} e^{i(k_x x + k_y y)} + r \begin{pmatrix} 1 \\ e^{i(\pi - \phi)} \end{pmatrix} e^{i(-k_x x + k_y y)} \quad 1.48$$

$$\psi_{II}(r) = \alpha \begin{pmatrix} 1 \\ -e^{i\vartheta} \end{pmatrix} e^{i(q_x x + q_y y)} + r \begin{pmatrix} 1 \\ -e^{i(\pi - \vartheta)} \end{pmatrix} e^{i(-q_x x + q_y y)} \quad 1.49$$

$$\psi_{III}(r) = t \begin{pmatrix} 1 \\ e^{i\phi} \end{pmatrix} e^{i(k_x x + k_y y)} \quad 1.50$$

where r and t denote amplitudes of reflection and transmission respectively and $\vartheta = \tan^{-1}(k_y/q_x)$, $q_x = \sqrt{(V_0 - E)^2/v_F^2 - k_y^2}$. The wavefunctions must satisfy the boundary conditions which are given by,

$$\psi_I(0, y) = \psi_{II}(0, y) \quad ; \quad \psi_{II}(d, y) = \psi_{III}(d, y) \quad 1.51$$

Form the boundary conditions, the transmission coefficient, T can be obtained which is given by,

$$T = t * t = \frac{\cos^2(\vartheta) \cos^2(\phi)}{\cos^2(dq_x) \cos^2(\phi) \cos^2(\vartheta) + \sin^2(dq_x) (1 + \sin(\phi) \sin(\vartheta))^2} \quad 1.52$$

For an infinite potential barrier, that is, $V_0 \rightarrow \infty$,

$$T = \frac{\cos^2(\phi)}{1 - \cos^2(dq_x) \sin^2(\phi)} \quad 1.53$$

From Eqn.(1.52) or Eqn.(1.53), it can be seen that when $dq_x = n\pi$ (n is an integer), $T = 1$. However, when $\phi = 0$ (thus $\vartheta = 0$), T is always equal to 1 for any value of dq_x . This behavior is referred to Klein tunneling. T. Ando [112] studied this

phenomenon 20 years ago in details.

1.8 Kane-Mele Model

The generation of spin currents is a subject of great interest in solid state systems. It has been stated in Ref. [113, 114], that spin-Hall effect can be observed in doped semiconductors in the presence of the spin-orbit (SO) interaction, where a spin current flows perpendicular to an applied electric field. Kane and Mele [82] have argued that at sufficiently low energies a single plane of graphene may exhibit a quantum spin-Hall (QSH) effect owing to an energy gap that can be generated by the SO interactions.

The effective mass Hamiltonian for graphene with a new term which denotes the spin-orbit interaction is given by [82],

$$H_0 = -i\hbar v_F \Psi^\dagger (\sigma_x \tau_z \partial_x + \sigma_y \partial_y) \Psi + \Delta_{SO} \Psi^\dagger \sigma_z \tau_z s_z \Psi \quad 1.54$$

where σ and τ are Pauli matrices with $\sigma_z = \pm 1$ describing states on the A(B) sublattice and $\tau_z = \pm 1$ describing describing states at the $K(K')$ points.

In the second quantized notation, the above Hamiltonian can be written in the following form,

$$H = -t_1 \sum_{\langle ij \rangle} a_i^\dagger b_j - t_1 \sum_{\langle ij \rangle} b_i^\dagger a_j + i\hbar l_I \sum_{\langle\langle ij \rangle\rangle} V_{ij} (a_i^\dagger \sigma_z a_j + b_i^\dagger \sigma_z b_j) \quad 1.55$$

The first and second terms denote the nearest neighbour (NN) hopping term from B to A and A to B sublattices respectively, with a hopping strength t_1 , the third term connects second neighbors with a spin dependent amplitude. $\langle\langle ij \rangle\rangle$ denotes the summation over next nearest neighbours, $V_{ij} = +(-)$ if the hopping is clock-(anti clock) wise. At low energies Eqn.(1.55) reduces to Eqn.(1.54) with $\Delta_{SO} = 3\sqrt{3}\hbar l_I$. If the mirror symmetry is broken by a perpendicular electric field, then there could be an additional spin-orbit coupling, which is a Rashba term [39] and is given by,

$$H_R = i\hbar l_R \sum_{\langle ij \rangle} a_i^\dagger (\hat{\sigma} \times \hat{d}_{ij}) \cdot \hat{z} b_j + i\hbar l_R \sum_{\langle ij \rangle} b_i^\dagger (\hat{\sigma} \times \hat{d}_{ij}) \cdot \hat{z} a_j \quad 1.56$$

For the quantum Hall effect to occur, the requirement is of the presence of gapless edge states which are able to conduct, although the bulk remain insulated. Kane and Mele has shown gapless edge states are present in their model. They have shown that the gapless edge states are present irrespective of the Rashba term and are robust against disorder or any perturbation that preserves the time reversal symmetry. Thus these gapless edge states characterize a novel topological state which is distinct from an ordinary insulator.

As we want to study the transport properties of graphene based junction devices in the presence of spin-orbit interactions, we have considered a Kane-Mele model in presence of both Rashba and intrinsic spin-orbit interactions to compute tunneling conductance and thermoelectric properties of graphene based junction devices.

1.9 Outline of the thesis

In the following, we present a more elaborate plan of the thesis by including a description of the various problems that have been tackled in the form of different chapters of the thesis. There are a total of eight chapters. We proceed with a brief description in the context of each one by one.

Chapter 1 presents an introduction of NS, NIS nano-junctions and their applications, Rashba spin-orbit coupling, Andreev reflection, Bogoliubov deGennes formalism, electron interferences leading to Fabry-Perot oscillations, basics of graphene, Klein tunneling and the Kane-Mele model. The chapter consolidates both the experimental and theoretical developments that have occurred in the field of the quantum transport through junction devices over several decades. It also provides a layout of the thesis that are discussed in subsequent chapters.

Chapter 2 deals with the Blonder-Tinkham-Klapwijk (BTK) [30] formalism for computing the current flowing across the normal-superconductor (NS) or normal-insulator-superconductor (NIS) devices. In both the NS and NIS junction devices, the low energy transmission characteristics are shown to be dominated by the Andreev reflection (AR) caused by the conversion of current in the normal region to a supercurrent in the superconductor occurring at the interface of the junction system. The superconducting sample is characterized by the quasiparticles that denote excitations of the Fermionic system and their propagation is described by the Bogoliubov-de Gennes (BdG) equations [101]. In this chapter we have modified the original BTK theory for different types of superconductor based junction systems suitable for our study and shown the detail derivations to compute the electrical conductance through the system. The BTK theory for studying the quantum transport through the graphene based junction devices and derivation of the involved formulae for the electrical conductance near the Dirac points for practical applications have been presented with due elaboration.

Chapter 3 describes the tunneling conductance properties of Rashba coupled normal metal-superconductor (NS) and normal metal-insulator-superconductor

(NIS) junction devices. In this chapter we report a thorough investigation on the interesting interplay between the RSOC parameter and a number of parameters that have experimental significances, such as, barrier transparency, quasiparticle lifetime, Fermi surface mismatch and their effects on the tunneling conductance. Further we have studied the conductance characteristics corresponding to the different types of pairing symmetries of the superconducting lead and the effects of the insulating layer intermediate to the metallic and superconducting electrodes therein. We have found that the interplay of the RSOC strength and the insulating barrier strength assumes a decisive role in determining the nature of conductance characteristics. As in case of a NIS junction the conductance gets suppressed significantly, the insulating layer between the metallic and superconducting leads has been modeled via an external gate voltage in such a way that it causes Fabry-Perot like oscillations in the conductance characteristics which depict signatures of electron interference. It is worth noting here that a conventional modeling of the insulating barrier would prohibit such oscillations, severely suppress the transmission and disallow exploration of the interplay of the barrier properties (such as its width) with the conductance spectra. Thus most of our work in the thesis involve modeling the insulating barrier by an external gate voltage. The tunability of the RSOC strength and the gate voltage that exists across the barrier gives possibility of a tunable conductance of this junction device.

Chapter 4 deals with the application of the NIS junctions in the field of thermoelectric studies. In this chapter we have studied the thermopower of this junction device and investigated how the RSOC and the properties of the insulating layer in between the metallic and the superconducting leads can control features of the thermopower that can be delivered by the junction. Also we have studied the efficiency of the system as a thermopower device. Further we have investigated its refrigeration properties and its the performance as a refrigerator. The Fabry-Perot like oscillations in the thermopower and thermoelectric cooling, similar to the charge conductance, are indicative of tunable thermoelectric properties via the external gate voltage across the barrier. Finally, the effects of an interesting interplay of the RSOC parameters and the gate voltage across the barrier on the thermoelectric properties have been studied in details which provides useful hints for achieving a desired thermopower or thermoelectric cooling.

Chapter 5 describes the tunneling conductance characteristics of Kane-Mele normal - superconductor (KMNS) and normal - insulator - superconductor junction system (KMNIS). In this chapter we have studied the spin resolved tunneling transport of the graphene based normal-superconductor and normal-insulator-

superconductor junctions in the presence of spin-orbit couplings. The presence of spin-orbit couplings is mimicked by the well known Kane-Mele model. Since the strengths of the spin-orbit coupling in graphene can be enhanced by adatoms or some other techniques, such as, using proximity effect of a three dimensional topological insulators [88, 115] , by functionalization with methyl groups [89] etc, we study noticeable changes in the transport properties at large values of the spin orbit couplings. We have investigated the effects of RSOC and ISOC on the transport properties of the KMNS and KMNIS nano-junctions where Fabry-Perot are discussed in the context of latter. Keeping in mind of the topological properties of the Kane Mele model, a scrutiny of the conductance properties is done corresponding to certain choices of the SOC parameters. This has probable implications with transmission through topological and trivial insulators.

Chapter 6 describes the application of the KMNIS junction in the field of thermoelectric applications. In this chapter we have studied the spin resolved thermoelectric properties of the KMNIS junction and investigated the role of the Rashba and intrinsic spin-orbit couplings. Further we have studied the efficiency of the system as a thermopower device. Finally the refrigeration properties and the performance of coefficient as a refrigerator of the KMNIS system have been explored. Keeping in mind about the tunable spin-orbit coupling, a detailed map of the parameter space (Rashba *vs* intrinsic SOC) is prepared for desired technological applications.

Chapter 7 deals with the comparison between the usual (parabolic energy dispersion) and graphene (linear energy dispersion) based junctions devices. Particularly we have focused on charge and heat transport. Mainly we have checked which of the two is more effective in generating larger electrical current, larger thermopower or is more useful for the phenomenon of thermoelectric cooling.

Chapter 8 summarizes the major findings of the work of this thesis and emphasizes on their significances.



Chapter 2: Blonder-Tinkham-Klapwijk (BTK) formalism

We need to introduce a simple, yet efficient technique to study the charge and heat transport through a spin-orbit coupled junction. Thus this chapter deals with the Blonder-Tinkham-Klapwijk (BTK) [30] formalism to compute the conductance through the normal-superconductor (NS) and normal-insulator-superconductor (NIS) junction devices. Here we present the derivation of the modified BTK equations for spin-orbit coupled junction devices. While deriving we separately consider parabolic and the linear energy momentum dispersions as they, respectively denote a generic two dimensional metal and graphene. We present the formalism one after another in the following. The inclusion of the spin-orbit coupling in graphene has been mimicked by the Kane-Mele model [82].

2.1 Normal-superconductor (NS) junction

We consider a two dimensional NS junction as shown in Fig.(2.1a) where an interface is located at $x = 0$, the left of which is a normal metal (N) with a superconducting (S) lead on the right. Due to the difference in crystal structure between the normal metal and superconducting specimen, a potential gradient across the interface can be responsible for the Rashba type spin-orbit coupling [39]. The interaction potential is described by,

$$U_{\sigma}(x) = U_1 \hat{n} \cdot (\vec{\sigma} \times \vec{k}) \Theta(-x) + U_2 \hat{n} \cdot (\vec{\sigma} \times \vec{k}) \Theta(x) + U_0 \delta_{x,0} \quad 2.1$$

where $\hat{n} = \hat{x}$ is the unit vector along the interface normal, U_0 is the strength of spin independent potential barrier at the interface which is considered to capture the effects of any interfacial scattering by a single parameter. This quantity actually represents the effect of the usual oxide layer in a contact, the localized disorder in the neck of a short micro-bridge [30]. U_1 and U_2 are the strengths of the RSOC for normal (N) region and superconducting (S) regions respectively. $\vec{\sigma}$ are the Pauli matrices, momentum, $\vec{k} = -i\vec{\nabla}$ and $\Theta(x)$ is the Heaviside function defined by,

$$\Theta(x) = 1 \text{ for } x > 0 ; \Theta(x) = 0 \text{ for } x < 0 \quad 2.2$$

Bogoliubov de Gennes (BdG) equations [101] are used here to describe the quasiparticles. The BdG equations (without any Rashba term) denote a 2×2 matrix in the quasiparticle basis, namely u and v . With inclusion of the Rashba term, the quasiparticle wave function acquires four components corresponding to the electron-hole and spin degrees of freedom. Assuming a two-dimensional

geometry (with \hat{n} pointing in the \hat{x} direction), only the σ_z matrix survive in the Rashba term, which does not mix the spin components and yields a decoupled Hamiltonian as follows,

$$H_\sigma \Psi(r) = E \Psi(r) \quad 2.3$$

where $\sigma = \pm 1$ denote two different spin orientations. H_σ is written as,

$$H_\sigma = \begin{pmatrix} -\frac{\hbar^2 \nabla^2}{2m} - E_F(x) + U_\sigma(x) & \tilde{\Delta} \\ \tilde{\Delta}^\dagger & \frac{\hbar^2 \nabla^2}{2m} + E_F(x) - U_\sigma(x) \end{pmatrix} \quad 2.4$$

where m is the electronic mass and $\tilde{\Delta}$ is the superconducting gap (see discussion below). The interaction term with $\hat{n} = \hat{x}$ can explicitly be written as,

$$U_\sigma(x) = U_0 \delta_{x,0} - \sigma U_1 (k_{N1})_y \Theta(-x) - \sigma U_2 (k_{S1})_y \Theta(x) \quad 2.5$$

The Fermi energies in the normal region and the superconducting region are E_F^N

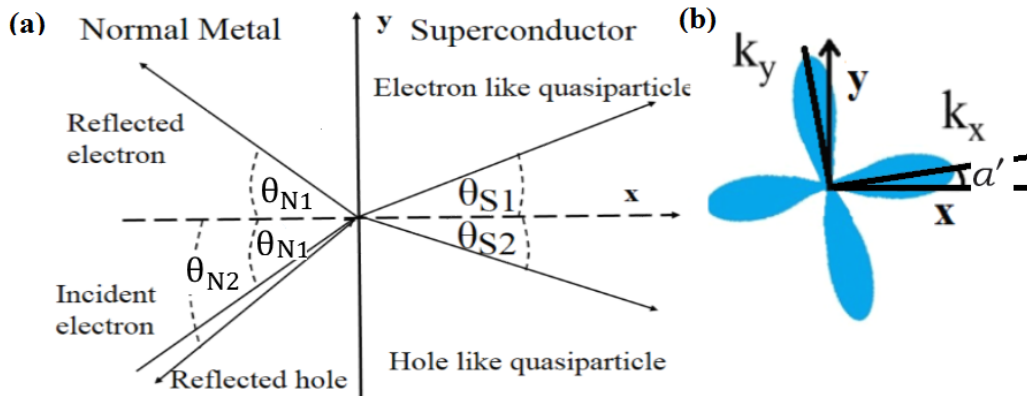


Figure 2.1: (a) Schematic illustration of the reflection and the transmission processes of the quasiparticle at an NS junction. (b) Profile for a d-wave superconducting gap. a' is the angle between the crystalline orientation and the x axis.

and E_F^S respectively. The superconducting gap for s-wave is a constant and is given by,

$$\tilde{\Delta}_s = \Delta_0 \Theta(x) \quad 2.6$$

Δ_0 being the strength of the gap. We also introduce the corresponding quantities for p-wave and d-wave superconductors respectively by [116–118],

$$\tilde{\Delta}_p = \Delta(k_\pm) \Theta(x) = \pm \Delta_0 e^{\pm i\theta_{S1,S2}} \Theta(x) \quad 2.7$$

and

$$\tilde{\Delta}_d = \Delta(k_\pm) \Theta(x) = \Delta_0 \cos(2\theta_{S1,S2} \mp 2a') \Theta(x) \quad 2.8$$

where a' is the angle between the crystalline orientation and x axis as shown in Fig.(2.1b), Δ_+ and Δ_- are the gap functions of electron and hole-like quasiparticles. The k dependence in the $\tilde{\Delta}_\pm$ enters through ∂_{S1} and ∂_{S2} (see Eq.(2.7) and Eq.(2.8)). It should be noted that the superconducting order parameter can be different for electron-like and hole-like quasiparticles.

To make our discussion clear, we refer to Fig.(2.1a). Suppose an electron from the left metallic lead is injected with an energy, $E \geq 0$, spin σ , and incident angle ∂_{N1} . The incident electron will be reflected back either as an electron (normal reflection) or as a hole (Andreev reflection). The momenta of the electrons and the holes in the normal region, k_{N1} and k_{N2} are given by,

$$\begin{aligned} k_{N1} &= \frac{\sigma m U_1 \sin \partial_{N1}}{\hbar^2} + \sqrt{\left(\frac{\sigma m U_1 \sin \partial_{N1}}{\hbar^2}\right)^2 + \frac{2m}{\hbar^2}(E_F^N + E)} \\ k_{N2} &= \frac{\sigma m U_1 \sin \partial_{N2}}{\hbar^2} + \sqrt{\left(\frac{\sigma m U_1 \sin \partial_{N2}}{\hbar^2}\right)^2 + \frac{2m}{\hbar^2}(E_F^N - E)} \end{aligned} \quad 2.9$$

Further the momenta of the electron-like and hole-like quasiparticles in superconducting region are given by k_{S1} and k_{S2} which are,

$$\begin{aligned} k_{S1} &= \frac{\sigma m U_2 \sin \partial_{S1}}{\hbar^2} + \sqrt{\left(\frac{\sigma m U_2 \sin \partial_{S1}}{\hbar^2}\right)^2 + \frac{2m}{\hbar^2}\left(E_F^S + \sqrt{E^2 - \tilde{\Delta}^2}\right)} \\ k_{S2} &= \frac{\sigma m U_2 \sin \partial_{S2}}{\hbar^2} + \sqrt{\left(\frac{\sigma m U_2 \sin \partial_{S2}}{\hbar^2}\right)^2 + \frac{2m}{\hbar^2}\left(E_F^S - \sqrt{E^2 - \tilde{\Delta}^2}\right)} \end{aligned} \quad 2.10$$

Here we consider a simplification where the magnitudes of these momenta of the electron-like and hole-like quasiparticles of the superconducting region are equal by setting,

$$k_{S1} = k_{S2} = \frac{\sigma m U_2 \sin \partial_{S1}}{\hbar^2} + \sqrt{\left(\frac{\sigma m U_2 \sin \partial_{S1}}{\hbar^2}\right)^2 + \frac{2m}{\hbar^2} E_F^S} \quad 2.11$$

This simplification introduces an error of the order $\sqrt{E^2 - \tilde{\Delta}^2}/E_F^S$. Since $\tilde{\Delta}$ is much smaller than E_F^S , this is a reasonable assumption. However we retain different symbols for them for the sake of convenience.

The momentum parallel to the interface is conserved in the tunneling process which allows us to write,

$$k_{N1} \sin \partial_{N1} = k_{N2} \sin \partial_{N2} = k_{S1} \sin \partial_{S1} = k_{S2} \sin \partial_{S2} \quad 2.12$$

where ∂_{N2} is angle of reflection of the hole due to AR, ∂_{S1} and ∂_{S2} are the angles of refraction of the electron-like and the hole-like quasiparticles respectively. All

the angles can be calculated from the following equations,

$$\begin{aligned}\sin \partial_{N2} &= \frac{k_{N1} \sin \partial_{N1}}{\sqrt{\frac{2m}{\hbar^2} \sigma U_1 k_{N1} \sin \partial_{N1} + \frac{2m}{\hbar^2} (E_F^N - E)}} \\ \sin \partial_{S1/S2} &= \frac{k_{N1} \sin \partial_{N1}}{\sqrt{\frac{2m}{\hbar^2} \sigma U_2 k_{N1} \sin \partial_{N1} + \frac{2m}{\hbar^2} E_F^S}}\end{aligned}\quad 2.13$$

The solutions of Eq.(2.3) has the form $\Psi(r) = e^{ik_y y} \Psi(x)$ where $\Psi(x)$ in the normal and the superconducting regions are given by,

$$\Psi_N(x) = \begin{pmatrix} 1 \\ 0 \end{pmatrix} e^{ik_{N1} \cos \partial_{N1} x} + a_\sigma \begin{pmatrix} 0 \\ 1 \end{pmatrix} e^{ik_{N2} \cos \partial_{N2} x} + b_\sigma \begin{pmatrix} 1 \\ 0 \end{pmatrix} e^{-ik_{N1} \cos \partial_{N1} x} \quad 2.14$$

and

$$\Psi_S(x) = c_\sigma \begin{pmatrix} u_+ e^{i\phi_+} \\ v_+ \end{pmatrix} e^{ik_{S1} \cos \partial_{S1} x} + d_\sigma \begin{pmatrix} v_- e^{i\phi_-} \\ u_- \end{pmatrix} e^{-ik_{S2} \cos \partial_{S2} x} \quad 2.15$$

respectively. Here a_σ and b_σ denote the amplitudes of the Andreev reflection (AR) and normal reflection (NR) respectively. Also c_σ and d_σ correspond to coefficients of transmission to the superconducting leads as electron-like quasiparticles and as hole-like quasiparticles whose amplitudes are given by,

$$u_\pm = \frac{1}{\sqrt{2}} \sqrt{1 + \frac{\Omega_\pm}{E}} ; \quad v_\pm = \frac{1}{\sqrt{2}} \sqrt{1 - \frac{\Omega_\pm}{E}} \quad 2.16$$

where

$$\Omega_\pm = \sqrt{E^2 - \tilde{\Delta}_\pm^2} \quad 2.17$$

The above wavefunctions are written in generalized forms which are applicable to all the pairing symmetries, that is, s , p and d - wave superconducting order parameters. For a s -wave superconductor $e^{i\phi_\pm}$ becomes 1 which renders $\Omega_+ = \Omega_- = \Omega$, $u_+ = u_- = u$ and $v_+ = v_- = v$. The wave functions must satisfy the boundary conditions,

$$\begin{aligned}\Psi_S(x=0^+) &= \Psi_N(x=0^-) \\ \frac{d\Psi_S}{dx}(x=0^+) - \frac{d\Psi_N}{dx}(x=0^-) &= \frac{2m}{\hbar^2} U_0 \Psi_N(x=0^-)\end{aligned}\quad 2.18$$

All the reflection and transmission amplitudes can be found from the boundary conditions. In particular, for the reflection amplitudes we obtain,

$$a_\sigma(E, \partial_{N1}) = \frac{Q\omega_-(P_1 - P_2)}{P_2 P_3 \omega_+ \omega_- e^{i\phi_+} - P_1 P_4 e^{i\phi_-}} \quad 2.19$$

and

$$b_\sigma(E, \partial_{N1}) = -\mathcal{Q}\omega_+\omega_- \frac{P_2 e^{i\phi_+}}{P_2 P_3 \omega_+ \omega_- e^{i\phi_+} - P_1 P_4 e^{i\phi_-}} + \frac{\mathcal{Q}P_1 e^{i\phi_-}}{P_2 P_3 \omega_+ \omega_- e^{i\phi_+} - P_1 P_4 e^{i\phi_-}} - 1 \quad 2.20$$

where,

$$\begin{aligned} \mathcal{Q} &= 2ik_{N1} \cos \partial_{N1} \\ \omega_\pm &= \frac{u_\pm}{v_\pm} \\ e^{i\phi_\pm} &= \tilde{\Delta}_\pm / |\tilde{\Delta}_\pm| \end{aligned} \quad 2.21$$

The four P_i 's appearing above are given by (considering $\hbar = 1$),

$$\begin{aligned} P_1 &= 2mU_0 + ik_{N2} \cos \partial_{N2} - ik_{S1} \cos \partial_{S1} \\ P_2 &= 2mU_0 + ik_{N2} \cos \partial_{N2} + ik_{S2} \cos \partial_{S2} \\ P_3 &= 2mU_0 - ik_{N1} \cos \partial_{N1} - ik_{S1} \cos \partial_{S1} \\ P_4 &= 2mU_0 - ik_{N1} \cos \partial_{N1} + ik_{S2} \cos \partial_{S2} \end{aligned} \quad 2.22$$

Using the BTK formalism, the normalized differential tunneling conductance (at zero temperature) is given by,

$$G(E) = \frac{G_S(E)}{G_N} \quad 2.23$$

where we have,

$$G_S(E) = \sum_\sigma \int_{-\pi/2}^{\pi/2} d\partial_{N1} \cos \partial_{N1} G_\sigma(E, \partial_{N1}) \quad 2.24$$

with the angle and the spin resolved conductance $G_\sigma(E, \partial_{N1})$ given by,

$$G_\sigma(E, \partial_{N1}) = 1 + |a_\sigma(E, \partial_{N1})|^2 \frac{\cos \partial_{N2}}{\cos \partial_{N1}} - |b_\sigma(E, \partial_{N1})|^2 \quad 2.25$$

and G_N is the conductance for a two metallic junctions. The consideration of different Fermi energies corresponding to two different regions imposes a further constraint on the effective range of the angle contributing to the integral appearing in Eq.(2.24). We consider this more elaborately in the following chapters.

2.2 Normal-insulator-superconductor (NIS) junction

Next we consider a two dimensional NIS junction setup as shown in Fig.(2.2) where the normal region and the superconducting region occupy $x \leq 0$ and $x \geq d$ respectively, with the insulating region extending from $x = 0$ to d . The $x \leq 0$ (normal) and $x \geq d$ (superconducting) regions denote the electrodes that carry the current through the junctions. The interfaces of this NIS junction are located at

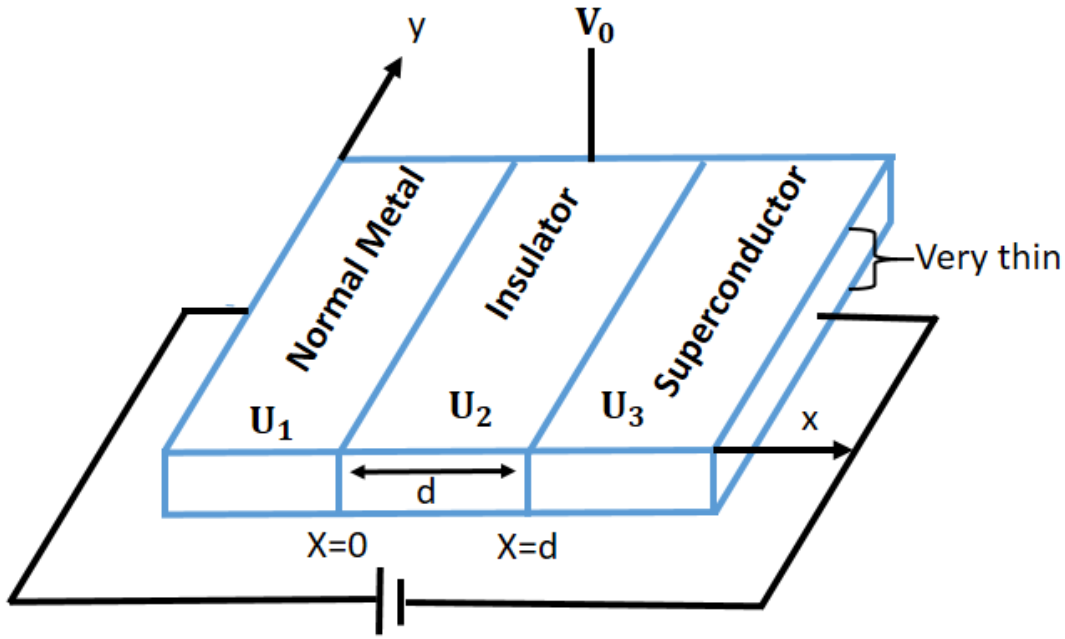


Figure 2.2: Schematic illustration of an NIS junction setup.

$x = 0$ and $x = d$. The RSOC is present owing to the violation of space inversion symmetry across the interfaces. The corresponding potential is given by,

$$U_o(x) = U_1 \hat{n} \cdot (\vec{\sigma} \times \vec{k}) \Theta(-x) + U_2 \hat{n} \cdot (\vec{\sigma} \times \vec{k}) \Theta(d - x) + U_3 \hat{n} \cdot (\vec{\sigma} \times \vec{k}) \Theta(x - d) \quad 2.26$$

where $\hat{n} = \hat{x}$ as the unit vector along the interface normal, U_1 , U_2 , U_3 are the strengths of the RSOC parameter in normal, insulating and superconducting region respectively. $\vec{\sigma}$ are the Pauli matrices, and the propagation direction is denoted by, \hat{k} . The Rashba term can explicitly be written as,

$$U_o(x) = -\sigma U_1 (k_{N1})_y \Theta(-x) - \sigma U_2 (k_{I1})_y \Theta(d - x) - \sigma U_3 (k_{S1})_y \Theta(x - d) \quad 2.27$$

The Fermi energy $E_F(x)$ across the junction is defined by,

$$E_F(x) = E_F^N \Theta(-x) + (E_F^N + V_0) \Theta(d - x) + (E_F^N + V_1) \Theta(x - d) \quad 2.28$$

E_F^N , $E_F^I = (E_F^N + V_0)$ and $E_F^S = (E_F^N + V_1)$ are the Fermi energies of normal, insulating and superconducting regions respectively. It needs to be noted that the Fermi energy of the insulating layer is ramped by V_0 via an arbitrary gate voltage applied across the barrier region and V_1 is electrostatic potential in the superconducting region, used to tune the Fermi surface mismatch between the metal and superconducting regions. Here we would like to point out that generally the Fermi energy of the insulating layer is defined by, $E_F^I = E_F^N - V_0$, in which case, if the V_0

is very high, the conductance through the NIS junction significantly decreases. To overcome this situation we have modeled the insulating layer by an external gate voltage across the barrier such that the transmission is possible through the junction. A similar approach has been taken by others as well [119].

The Bogoliubov DeGennes (BdG) equations [101] to describe the quasiparticles in the superconducting regime are discussed in previous section (see Eqn.(2.3) and Eqn.(2.4)).

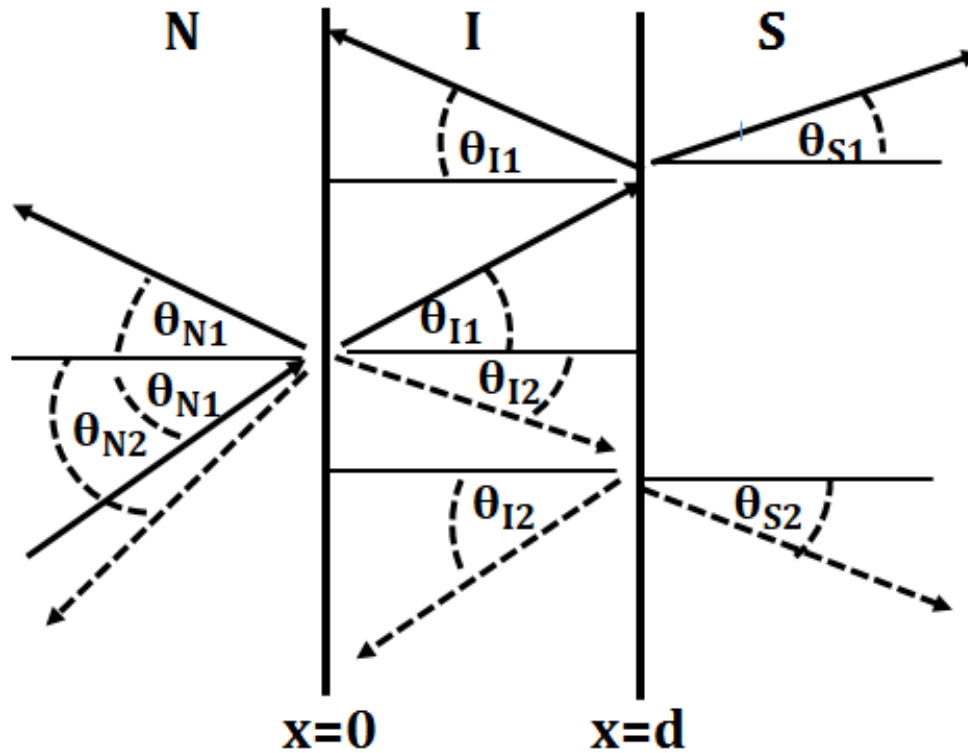


Figure 2.3: Schematic illustration of the reflection and the transmission processes of the quasiparticle at an NIS junction. The insulating region is between $[0 : d]$. Solid lines denote the electrons and the dashed lines denote the holes.

To understand the different processes that take place in an NIS junction, we refer to Fig.(2.3). Suppose an electron from the left (normal) lead is injected with a biasing energy, $E \geq 0$, spin σ , and incident angle θ_{N1} . The different processes taking place are different from that of the NS junction. They are : (i) Andreev reflection with angle θ_{N2} (ii) normal reflection with angle θ_{N1} (iii) transmission as electron with angle θ_{I1} and as hole with angle θ_{I2} to the insulating region (iv) reflection as an electron with angle θ_{I1} and as a hole with angle θ_{I2} at the insulating and the superconducting interfaces (v) transmission as electron-like quasiparticle with angle θ_{S1} and as hole-like quasiparticle with angle θ_{S2} . The

momenta of electrons and holes in the normal region are given by,

$$\begin{aligned} k_{N1} &= \frac{\sigma m U_1 \sin \partial_{N1}}{\hbar^2} + \sqrt{\left(\frac{\sigma m U_1 \sin \partial_{N1}}{\hbar^2}\right)^2 + \frac{2m}{\hbar^2}(E_F^N + E)} \\ k_{N2} &= \frac{\sigma m U_1 \sin \partial_{N2}}{\hbar^2} + \sqrt{\left(\frac{\sigma m U_1 \sin \partial_{N2}}{\hbar^2}\right)^2 + \frac{2m}{\hbar^2}(E_F^N - E)} \end{aligned} \quad 2.29$$

Similarly, the momenta of electrons and holes in the insulating region are given by,

$$\begin{aligned} k_{I1} &= \frac{\sigma m U_2 \sin \partial_{I1}}{\hbar^2} + \sqrt{\left(\frac{\sigma m U_2 \sin \partial_{I1}}{\hbar^2}\right)^2 + \frac{2m}{\hbar^2}(E_F^I + E)} \\ k_{I2} &= \frac{\sigma m U_2 \sin \partial_{I2}}{\hbar^2} + \sqrt{\left(\frac{\sigma m U_2 \sin \partial_{I2}}{\hbar^2}\right)^2 + \frac{2m}{\hbar^2}(E_F^I - E)} \end{aligned} \quad 2.30$$

Further, the momenta of the electron-like and hole-like quasiparticles in superconducting region are,

$$\begin{aligned} k_{S1} &= \frac{\sigma m U_3 \sin \partial_{S1}}{\hbar^2} + \sqrt{\left(\frac{\sigma m U_3 \sin \partial_{S1}}{\hbar^2}\right)^2 + \frac{2m}{\hbar^2}(E_F^S + \sqrt{E^2 - \tilde{\Delta}^2})} \\ k_{S2} &= \frac{\sigma m U_3 \sin \partial_{S2}}{\hbar^2} + \sqrt{\left(\frac{\sigma m U_3 \sin \partial_{S2}}{\hbar^2}\right)^2 + \frac{2m}{\hbar^2}(E_F^S - \sqrt{E^2 - \tilde{\Delta}^2})} \end{aligned} \quad 2.31$$

The momentum parallel to the interface is conserved in the tunneling process. So we can write,

$$k_{N1} \sin \partial_{N1} = k_{N2} \sin \partial_{N2} = k_{I1} \sin \partial_{I1} = k_{I2} \sin \partial_{I2} = k_{S1} \sin \partial_{S1} = k_{S2} \sin \partial_{S2} \quad 2.32$$

All the angles are to be calculated from,

$$\begin{aligned} \sin \partial_{N2} &= \frac{k_{N1} \sin \partial_{N1}}{\sqrt{\frac{2m}{\hbar^2} \sigma U_1 k_{N1} \sin \partial_{N1} + \frac{2m}{\hbar^2}(E_F^N - E)}} \\ \sin \partial_{I1} &= \frac{k_{N1} \sin \partial_{N1}}{\sqrt{\frac{2m}{\hbar^2} \sigma U_2 k_{N1} \sin \partial_{N1} + \frac{2m}{\hbar^2}(E_F^I + E)}} \\ \sin \partial_{I2} &= \frac{k_{N1} \sin \partial_{N1}}{\sqrt{\frac{2m}{\hbar^2} \sigma U_2 k_{N1} \sin \partial_{N1} + \frac{2m}{\hbar^2}(E_F^I - E)}} \\ \sin \partial_{S1/S2} &= \frac{k_{N1} \sin \partial_{N1}}{\sqrt{\frac{2m}{\hbar^2} \sigma U_3 k_{N1} \sin \partial_{N1} + \frac{2m}{\hbar^2} E_F^S}} \end{aligned} \quad 2.33$$

The solutions of Eqn.(2.3) in the normal, insulator and the superconducting re-

gions are,

$$\Psi_N(x) = \begin{pmatrix} 1 \\ 0 \end{pmatrix} e^{ik_{N1} \cos \vartheta_{N1} x} + a_\sigma \begin{pmatrix} 0 \\ 1 \end{pmatrix} e^{ik_{N2} \cos \vartheta_{N2} x} + b_\sigma \begin{pmatrix} 1 \\ 0 \end{pmatrix} e^{-ik_{N1} \cos \vartheta_{N1} x} \quad 2.34$$

$$\Psi_I(x) = l_\sigma \begin{pmatrix} 1 \\ 0 \end{pmatrix} e^{ik_{I1} \cos \vartheta_{I1} x} + m_\sigma \begin{pmatrix} 1 \\ 0 \end{pmatrix} e^{-ik_{I1} \cos \vartheta_{I1} x} + p_\sigma \begin{pmatrix} 0 \\ 1 \end{pmatrix} e^{-ik_{I2} \cos \vartheta_{I2} x} + q_\sigma \begin{pmatrix} 0 \\ 1 \end{pmatrix} e^{ik_{I2} \cos \vartheta_{I2} x} \quad 2.35$$

and

$$\Psi_S(x) = c_\sigma \begin{pmatrix} u_+ e^{i\varphi_+} \\ v_+ \end{pmatrix} e^{ik_{S1} \cos \vartheta_{S1} x} + d_\sigma \begin{pmatrix} v_- e^{i\varphi_-} \\ u_- \end{pmatrix} e^{-ik_{S2} \cos \vartheta_{S2} x} \quad 2.36$$

respectively. Here a_σ and b_σ denote the amplitudes of reflection of hole (AR) and normal reflection (NR) respectively in the normal region. l_σ and m_σ denote the amplitudes of incoming and reflected electron in the insulating region. Further p_σ and q_σ represent for amplitudes of the incoming and the reflected holes in the insulating region. Also c_σ and d_σ correspond to coefficients of transmission to the superconducting leads as electron-like quasiparticles and as hole-like quasiparticles. The expressions for u_\pm, v_\pm are given earlier in Eqn.(2.16).

The wave functions must satisfy the boundary conditions,

$$\begin{aligned} \Psi_N(x=0) &= \Psi_I(x=0) ; \quad \Psi_I(x=d) = \Psi_S(x=d) \\ \frac{d\Psi_I}{dx}(x=0) &= \frac{d\Psi_N}{dx}(x=0) ; \quad \frac{d\Psi_S}{dx}(x=d) = \frac{d\Psi_I}{dx}(x=d) \end{aligned} \quad 2.37$$

All the reflection and the transmission amplitudes can be found from the boundary conditions. In particular, the reflection amplitudes needed to compute the conductance (see Eq.(2.23)), are given by,

$$a_\sigma = p_\sigma + q_\sigma ; \quad b_\sigma = l_\sigma + m_\sigma - 1 \quad 2.38$$

where,

$$\begin{aligned} l_\sigma &= P_1 c_\sigma u_+ e^{i\varphi_+} + P_2 d_\sigma v_- e^{i\varphi_-} ; \quad m_\sigma = P_3 c_\sigma u_+ e^{i\varphi_+} + P_4 d_\sigma v_- e^{i\varphi_-} \\ q_\sigma &= P_5 c_\sigma v_+ + P_6 d_\sigma u_- ; \quad p_\sigma = P_7 c_\sigma v_+ + P_8 d_\sigma u_- \end{aligned} \quad 2.39$$

The different P_i 's appearing above are respectively are given by,

$$\begin{aligned}
 P_1 &= e^{i(X_{S1}-X_{I1})d} \left[\frac{X_{I1} + X_{S1}}{2X_{I1}} \right] & ; & & P_2 &= e^{-i(X_{S1}+X_{I1})d} \left[\frac{X_{I1} - X_{S1}}{2X_{I1}} \right] & \quad \text{2.40} \\
 P_3 &= (e^{i(X_{S1}-X_{I1})d} - P_1) e^{2iX_{I1}d} & ; & & P_4 &= (e^{-i(X_{S1}+X_{I1})d} - P_2) e^{2iX_{I1}d} \\
 P_5 &= e^{i(X_{S1}-X_{I2})d} \left[\frac{X_{I2} + X_{S1}}{2X_{I2}} \right] & ; & & P_6 &= e^{-i(X_{S1}+X_{I2})d} \left[\frac{X_{I2} - X_{S1}}{2X_{I2}} \right] \\
 P_7 &= (e^{i(X_{S1}-X_{I2})d} - P_5) e^{2iX_{I2}d} & ; & & P_8 &= (e^{-i(X_{S1}+X_{I2})d} - P_6) e^{2iX_{I2}d}
 \end{aligned}$$

Further,

$$c_\sigma = -d_\sigma \frac{u_- L_4}{v_+ L_3} & ; & d_\sigma = \frac{2}{v_- L_2 e^{i\phi_-} - \frac{u_+ u_- L_1 L_4}{v_+ L_3} e^{i\phi_+}} & ; & e^{i\phi_\pm} = \tilde{\Delta}_\pm / |\tilde{\Delta}_\pm| \quad \text{2.41}$$

All the L_i and the X_i appearing in Eqn.(2.40) and Eqn.(2.41) are given by,

$$\begin{aligned}
 L_1 &= P_1 + P_3 + \frac{X_{I1}(P_1 - P_3)}{X_{N1}} & ; & & L_2 &= P_2 + P_4 + \frac{X_{I1}(P_2 - P_4)}{X_{N1}} & \quad \text{2.42} \\
 L_3 &= P_5 + P_7 - \frac{X_{I2}(P_5 - P_7)}{X_{N2}} & ; & & L_4 &= P_6 + P_8 - \frac{X_{I2}(P_6 - P_8)}{X_{N2}} \\
 X_{N1,N2} &= k_{N1,N2} \cos \partial_{N1,N2} & ; & & X_{I1,I2} &= k_{I1,I2} \cos \partial_{I1,I2} & ; & & X_{S1,S2} &= k_{S1,S2} \cos \partial_{S1,S2}
 \end{aligned}$$

Now using the formulae of Eqn.(2.23, 2.24, 2.25) the conductance through the NIS junctions can be obtained.

2.3 Graphene based NS junction: Kane-Mele model

In this section we set up the equations to study the transport properties of an NS junction in a graphene sheet placed along XY plane. The schematic diagram of the junction setup has been shown in Fig.(2.1a) where the left electrode is a normal ($x \leq 0$) and the right one ($x \geq 0$) is made of a superconducting material. The $x \geq 0$ region is considered to have been produced by proximity effect by an external superconductor. For simplicity, we consider s-wave pairing symmetry for the graphene superconductor.

The Hamiltonian for the Kane-Mele model in presence of Rashba spin-orbit coupling is written as,

$$\begin{aligned}
 H &= -t_1 \sum_{\langle ij \rangle} a_i^\dagger b_j + i\hat{n}_I \sum_{\langle\langle ij \rangle\rangle} V_{ij} (a_i^\dagger \sigma_z a_j \\
 &+ b_i^\dagger \sigma_z b_j) + i\hat{n}_R \sum_{\langle ij \rangle} a_i^\dagger (\hat{\sigma} \times \hat{d}_{ij}) \cdot \hat{n} b_j + \hat{n}_v \sum_i a_i^\dagger a_i \\
 &- \hat{n}_v \sum_i b_i^\dagger b_i + h.c. \quad \text{2.43}
 \end{aligned}$$

The first term is the nearest neighbour (NN) hopping term, with a hopping

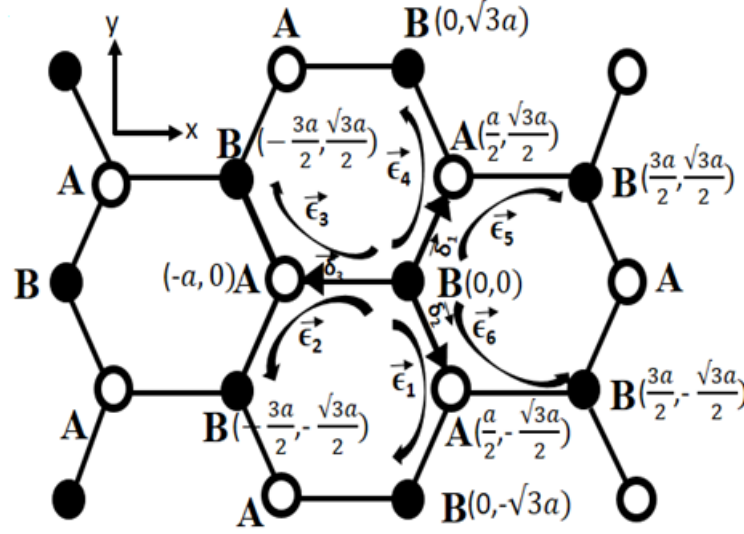


Figure 2.4: Schematic diagram of graphene. The coordinates of A and B sublattices are shown. The nearest neighbour vectors are denoted by \vec{d}_i and the next-nearest neighbour vectors are denoted by \vec{e}_i .

strength t_1 , the second term is local intrinsic spin-orbit coupling term given by the next-nearest neighbours (NNN) hopping, where $\hat{\eta}_I$ is the strength of the intrinsic spin-orbit coupling. $\langle\langle ij \rangle\rangle$ denotes the summation over NNN, $V_{ij} = +(-)$ if the hopping is clock-(anti clock) wise. The third term is the nearest neighbour Rashba term, where \hat{d}_{ij} is the unit vector pointing from site i to j , σ is the vector of Pauli matrices and $\hat{n} = \hat{x}$ is unit vector along the interface normal. $\hat{\eta}_v$ is an on-site energy which is different on the two sites within the cell. In particular we have considered ” $+\hat{\eta}_v$ ” energy at site A and ” $-\hat{\eta}_v$ ” energy at site B. Operators a_i^\dagger (b_i^\dagger) create and a_i (b_i) annihilate an electron at R_i site of the A(B) sublattices.

We apply the following transformation to the above Hamiltonian in Eqn.(2.43),

$$a_i = \frac{1}{\sqrt{N}} \sum_{\mathbf{k}} a_{\mathbf{k}} e^{-i\mathbf{k}\cdot\mathbf{r}_i} \quad a_i^\dagger = \frac{1}{\sqrt{N}} \sum_{\mathbf{k}} a_{\mathbf{k}}^\dagger e^{i\mathbf{k}\cdot\mathbf{r}_i} \quad 2.44$$

A Fourier transformation of H yields,

$$H = \begin{pmatrix} \hat{\eta}_v - i\hat{\eta}_I(S_1 - S_2) & -t_1 f - i\hat{\eta}_R S_3 & 0 & 0 \\ -t_1 f^* + i\hat{\eta}_R S_3^* & -\hat{\eta}_v + i\hat{\eta}_I(S_1 - S_2) & 0 & 0 \\ 0 & 0 & \hat{\eta}_v + i\hat{\eta}_I(S_1 - S_2) & -t_1 f + i\hat{\eta}_R S_3 \\ 0 & 0 & -t_1 f^* - i\hat{\eta}_R S_3^* & -\hat{\eta}_v - i\hat{\eta}_I(S_1 - S_2) \end{pmatrix} \quad 2.45$$

where the coefficient $f(k)$, $S_1(k)$, $S_2(k)$ and $S_3(k)$ are given by,

$$\begin{aligned} f(k) &= [e^{-i\vec{k}\cdot\vec{\delta}_1} + e^{-i\vec{k}\cdot\vec{\delta}_2} + e^{-i\vec{k}\cdot\vec{\delta}_3}] \\ S_1(k) &= [e^{-i\vec{k}\cdot\vec{\epsilon}_1} + e^{-i\vec{k}\cdot\vec{\epsilon}_3} + e^{-i\vec{k}\cdot\vec{\epsilon}_5}] \\ S_2(k) &= [e^{-i\vec{k}\cdot\vec{\epsilon}_2} + e^{-i\vec{k}\cdot\vec{\epsilon}_4} + e^{-i\vec{k}\cdot\vec{\epsilon}_6}] \\ S_3(k) &= \frac{\sqrt{3}}{2}[e^{-i\vec{k}\cdot\vec{\delta}_1} - e^{-i\vec{k}\cdot\vec{\delta}_2}] \end{aligned} \quad 2.46$$

$\vec{\delta}_1$, $\vec{\delta}_2$, $\vec{\delta}_3$ are the three NN hopping and $\vec{\epsilon}_1$, $\vec{\epsilon}_2$, ..., $\vec{\epsilon}_6$ are the NNN hopping in real space (see Fig.(2.4)). The NN and NNN hopping terms are given by,

$$\begin{aligned} \vec{\delta}_1 &= \frac{a}{2}\hat{x} + \frac{\sqrt{3}a}{2}\hat{y} ; \quad \vec{\delta}_2 = \frac{a}{2}\hat{x} - \frac{\sqrt{3}a}{2}\hat{y} ; \quad \vec{\delta}_3 = -a\hat{x} \\ \vec{\epsilon}_1 &= -\sqrt{3}a\hat{y} ; \quad \vec{\epsilon}_2 = -\frac{3a}{2}\hat{x} - \frac{\sqrt{3}a}{2}\hat{y} \\ \vec{\epsilon}_3 &= -\frac{3a}{2}\hat{x} + \frac{\sqrt{3}a}{2}\hat{y} ; \quad \vec{\epsilon}_4 = \sqrt{3}a\hat{y} \\ \vec{\epsilon}_5 &= \frac{3a}{2}\hat{x} + \frac{\sqrt{3}a}{2}\hat{y} ; \quad \vec{\epsilon}_6 = \frac{3a}{2}\hat{x} - \frac{\sqrt{3}a}{2}\hat{y} \end{aligned} \quad 2.47$$

The Hamiltonian can be represented by a following 2×2 matrix for each spin degree of freedom,

$$H_\sigma = \begin{pmatrix} \hat{n}_v - i\sigma\hat{n}_I(S_1 - S_2) & -t_1f(k) - i\sigma\hat{n}_R S_3 \\ -t_1f^* + i\sigma\hat{n}_R S_3^* & -\hat{n}_v + i\sigma\hat{n}_I(S_1(k) - S_2) \end{pmatrix} \quad 2.48$$

where $\sigma = \pm$ for up spin and down spin respectively.

In graphene near the K and K' points, the energy dispersion is a linear function of the momentum, where the K and K' points are given by,

$$\vec{K} = (0, \frac{4\pi}{3\sqrt{3}a}) ; \quad \vec{K}' = (0, -\frac{4\pi}{3\sqrt{3}a}) \quad 2.49$$

As we shall like to focus on the low energy physics for explaining transmission properties in our thesis, we expand the $f(k)$, $S_1(k)$, $S_2(k)$ and $S_3(k)$ in Eqn.(2.46) near the K point. The expansion yields,

$$\begin{aligned} f(\vec{K} + \vec{q}) &= -\frac{3}{2}a[q_y - iq_x] ; \quad (S_1 - S_2)(\vec{K} + \vec{q}) = -3\sqrt{3}i \\ S_3(\vec{K} + \vec{q}) &= \frac{\sqrt{3}}{2}[-i\sqrt{3} - \frac{\sqrt{3}a}{2}(q_x - iq_y)] \end{aligned} \quad 2.50$$

An equivalent expression can be done around the K' point. We have concentrated on results in the vicinity of one of non-identical k points. In particular we have

chosen the K point, while the K' point would have given slightly different, although qualitatively similar results.

The NS junction can be described by the familiar Dirac-Bogoliubov de Gennes (BdG) equations. It is clear that the Hamiltonian splits into two blocks one for each spin as we have considered $\hat{n} = \hat{x}$ (normal to the interface). The two component decoupled BdG equation for each spin can be written as,

$$H'_\sigma \Psi(r) = E \Psi(r) \quad 2.51$$

where H'_σ is given by,

$$H'_\sigma(\vec{K} + \vec{q}) = \begin{pmatrix} \hat{\eta}'_{lv} - E_F(x) & Mq_y - iNq_x - \sigma\hat{\eta}'_R & \tilde{\Delta} & 0 \\ Mq_y + iNq_x - \sigma\hat{\eta}'_R & -\hat{\eta}'_{lv} - E_F(x) & 0 & \tilde{\Delta} \\ \tilde{\Delta} & 0 & -\hat{\eta}'_{lv} + E_F(x) & -Mq_y + iNq_x + \sigma\hat{\eta}'_R \\ 0 & \tilde{\Delta} & -Mq_y - iNq_x + \sigma\hat{\eta}'_R & \hat{\eta}'_{lv} + E_F(x) \end{pmatrix} \quad 2.52$$

and the M , N , $\hat{\eta}'_R$ and $\hat{\eta}'_{lv}$ appearing in the above Hamiltonian are given by,

$$M = \frac{3at_1}{2} + \sigma \frac{\hat{\eta}'_R a}{2} \quad ; \quad N = \frac{3at_1}{2} - \sigma \frac{\hat{\eta}'_R a}{2} \quad 2.53$$

$$\hat{\eta}'_R = \frac{3\hat{\eta}_R}{2} \quad ; \quad \hat{\eta}'_{lv} = \hat{\eta}_v - \sigma 3\sqrt{3}\hat{\eta}_l$$

The Fermi energy variation across the system is assumed to have the form,

$$E_F(x) = E_F^N \Theta(-x) + E_F^S \Theta(x) \quad 2.54$$

where E_F^N and E_F^S are the Fermi energies of the normal lead and the superconducting leads where, $E_F^S = E_F^N + V_0$, The Fermi energy mismatch is characterized by the potential, V_0 . The terms, $\tilde{\Delta}$ are the superconducting order parameter. As said earlier, here we have considered only s-wave case which yields the following form, $\tilde{\Delta}_s = \Delta_0 \Theta(x)$.

We reiterate the physical process relevant to the transmission characteristics. Suppose an electron from the left normal lead is made to incident with spin σ , and incident angle ∂_{N1} . This electron at the normal-superconductor interface ($x = 0$) experiences the following processes. (i) an Andreev reflection by an angle ∂_{N2} , (ii) a normal reflection by an angle ∂_{N1} , (iii) transmission as electron-like quasiparticle and also as hole-like quasiparticle with an angle ∂_{S1} and ∂_{S2} respectively.

Since the momentum parallel to the interface is conserved in the tunneling process we can write,

$$q^{N1} \sin \partial_{N1} = q^{N2} \sin \partial_{N2} = q^{S1} \sin \partial_{S1} = q^{S2} \sin \partial_{S2} \quad 2.55$$

where q^{N1} , q^{N2} are the momenta of the electrons and the holes in the normal region and q^{S1} , q^{S2} are the momenta of the electron-like quasiparticle and the hole-like quasiparticle in the superconducting region. The expressions for momenta corresponding to all of them are given by the following compact form,

$$q^{N1/S1/N2/S2} = \frac{B_{N1/S1/N2/S2} \pm \sqrt{B_{N1/S1/N2/S2}^2 - 4 \cdot A_{N1/S1/N2/S2} \cdot C_{N1/S1/N2/S2}}}{2A_{N1/S1/N2/S2}} \quad 2.56$$

where,

$$\begin{aligned} A_{N1/S1/N2/S2} &= N^2 \cos^2 \partial_{N1/S1/N2/S2} + M^2 \sin^2 \partial_{N1/S1/N2/S2} \\ B_{N1/S1/N2/S2} &= 2\hat{\eta}'_R M \sin \partial_{N1/S1/N2/S2} \\ C_{N1} &= \hat{\eta}'_{lv}{}^2 + \hat{\eta}'_R{}^2 - (E + E_F^N)^2 \\ C_{N2} &= \hat{\eta}'_{lv}{}^2 + \hat{\eta}'_R{}^2 - (E - E_F^N)^2 \\ C_{S1} &= \hat{\eta}'_{lv}{}^2 + \hat{\eta}'_R{}^2 - (\sqrt{E^2 - \tilde{\Delta}^2} + E_F^S)^2 \\ C_{S2} &= \hat{\eta}'_{lv}{}^2 + \hat{\eta}'_R{}^2 - (\sqrt{E^2 - \tilde{\Delta}^2} - E_F^S)^2 \end{aligned} \quad 2.57$$

and all the angles can be calculated from the following relation,

$$\sin \partial_{N2/S1/S2} = \frac{Nq^{N1} \sin \partial_{N1}}{\sqrt{-C_{N2/S1/S2} + 2M\hat{\eta}'_R q^{N1} \sin \partial_{N1} + (N^2 - M^2)(q^{N1} \sin \partial_{N1})^2}} \quad 2.58$$

The solutions of Eqn.(2.51) in the normal and the superconducting regions can be expressed as,

$$\begin{aligned} \Psi_N(x) &= \begin{pmatrix} 1 \\ W_1 \\ 0 \\ 0 \end{pmatrix} e^{iq^{N1} \cos \partial_{N1} x} + a_\sigma \begin{pmatrix} 0 \\ 0 \\ 1 \\ W_3 \end{pmatrix} e^{iq^{N2} \cos \partial_{N2} x} \\ &+ b_\sigma \begin{pmatrix} 1 \\ W_2 \\ 0 \\ 0 \end{pmatrix} e^{-iq^{N1} \cos \partial_{N1} x} \end{aligned} \quad 2.59$$

and

$$\Psi_S(x) = c_\sigma \begin{pmatrix} 1 \\ W_4 \\ e^{-i\beta} \\ e^{-i\beta} W_4 \end{pmatrix} e^{iq^{S1} \cos \partial_{S1} x} + d_\sigma \begin{pmatrix} 1 \\ W_5 \\ e^{i\beta} \\ e^{i\beta} W_5 \end{pmatrix} e^{-iq^{S2} \cos \partial_{S2} x} \quad 2.60$$

where a_σ and b_σ are the amplitudes of the Andreev reflection (AR) and the normal reflection (NR) respectively in the normal electrode. Further c_σ and d_σ correspond to coefficients of transmission into the superconducting leads as electron-like quasiparticles and as hole-like quasiparticles with,

$$\begin{aligned}
W_1 &= \frac{E_F^N + E - \hat{I}'_{Iv}}{Mq^{N1} \sin \partial_{N1} - iNq^{N1} \cos \partial_{N1} - \sigma \hat{I}'_R} \\
W_2 &= \frac{E_F^N + E - \hat{I}'_{Iv}}{Mq^{N1} \sin \partial_{N1} + iNq^{N1} \cos \partial_{N1} - \sigma \hat{I}'_R} \\
W_3 &= \frac{E_F^N - E - \hat{I}'_{Iv}}{Mq^{N2} \sin \partial_{N2} - iNq^{N2} \cos \partial_{N2} - \sigma \hat{I}'_R} \\
W_4 &= \frac{E_F^S + \Omega - \hat{I}'_{Iv}}{Mq^{S1} \sin \partial_{S1} - iNq^{S1} \cos \partial_{S1} - \sigma \hat{I}'_R} \\
W_5 &= \frac{E_F^S - \Omega - \hat{I}'_{Iv}}{Mq^{S2} \sin \partial_{S2} + iNq^{S2} \cos \partial_{S2} - \sigma \hat{I}'_R} \\
\Omega &= \sqrt{E^2 - \tilde{\Delta}^2} ; e^{\pm i\beta} = \frac{E \pm \Omega}{\tilde{\Delta}}
\end{aligned} \tag{2.61}$$

The wave functions must satisfy the following boundary condition,

$$\Psi_N(x=0) = \Psi_S(x=0) \tag{2.62}$$

All the reflection and transmission amplitudes can be obtained from the above boundary condition. In particular, the reflection amplitudes are given by,

$$a_\sigma = c_\sigma e^{-i\beta} + d_\sigma e^{i\beta} ; b_\sigma = c_\sigma + d_\sigma - 1 \tag{2.63}$$

where,

$$\begin{aligned}
c_\sigma &= -d_\sigma e^{2i\beta} \frac{W_3 - W_5}{W_3 - W_4} \\
d_\sigma &= \frac{(W_1 - W_2)(W_3 - W_4)}{-W_2 W_3 + W_2 W_4 + W_3 W_5 - W_4 W_5 + e^{2i\beta}(W_2 W_3 - W_3 W_4 - W_2 W_5 + W_4 W_5)}
\end{aligned} \tag{2.64}$$

Using the BTK formalism, the normalized differential tunneling conductance at zero temperature is given by, $G_\sigma(E) = \frac{G_\sigma^S(E)}{G_N}$, where the expressions for $G_\sigma(E)$, $G_\sigma^S(E)$ and G_N are given in Eqn.(2.23,2.24,2.25).

2.4 Graphene (Kane-Mele) based NIS junction

Next we shift focus to a NIS junction. In Fig.(2.5) the schematic diagram of the junction setup has been shown where the left electrode is a normal ($x \leq 0$) and the right electrode ($x \geq d$) is a superconducting material with the insulating layer

is extending from $x = 0$ to $x = d$. It may be considered that the superconducting ($x \geq d$) region of the junction system is produced by proximity effect due to an external superconductor.

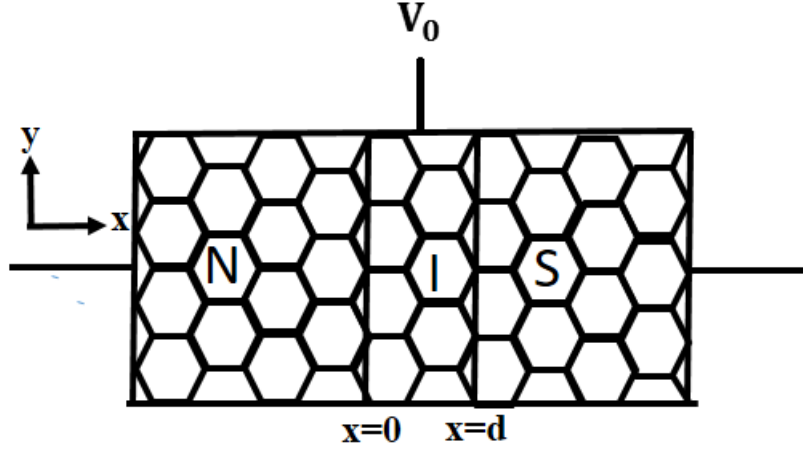


Figure 2.5: Schematic diagram of a graphene based NIS junction setup.

The Kane-Mele Hamiltonian and the corresponding simplification is elaborately discussed in previous section. The Fermi energy variation across the junction system is,

$$E_F(x) = E_F^N \Theta(-x) + E_F^I \Theta(d - x) + E_F^S \Theta(x - d) \quad 2.65$$

where E_F^N and E_F^S are the Fermi energies of the normal and superconducting leads. E_F^I is the Fermi energy of the insulating barrier which is defined by, $E_F^I = E_F^N + V_0$. The Fermi energy of the insulating layer is ramped by V_0 using an external gate voltage across the insulating barrier.

Again we remind the physical processes for the NIS junction. Suppose an electron from the left metallic lead is made to incident with spin σ , and incident angle ∂_{N1} . This electron at the normal-insulator interface ($x = 0$) experiences the following processes. (i) an Andreev reflection by an angle ∂_{N2} , (ii) a normal reflection by an angle ∂_{N1} and (iii) a transmission as an electron and a hole with the angle ∂_{I1} and ∂_{I2} respectively into the insulating region. Further at the insulator-superconductor interface ($x = d$) the electron experiences, (i) reflections both as an electron and a hole by an angle ∂_{I1} and ∂_{I2} , and (ii) transmission as an electron-like quasiparticle and also as a hole-like quasiparticle with an angle ∂_{S1} and ∂_{S2} .

Since the momentum parallel to the interface is conserved in the tunneling process, we can write,

$$q^{N1} \sin \partial_{N1} = q^{N2} \sin \partial_{N2} = q^{I1} \sin \partial_{I1} = q^{I2} \sin \partial_{I2} = q^{S1} \sin \partial_{S1} = q^{S1} \sin \partial_{S1} \quad 2.66$$

where q^{N1} , q^{N2} are the momenta of electrons and holes in the normal region, q^{I1} ,

q^{I2} are the momenta of electrons and holes in the insulating region and q^{S1} , q^{S2} are the momenta of electron-like and hole-like quasiparticles in the superconducting region. All the expressions for momenta are given by,

$$q^{N1/I1/S1} = \frac{B_{N1/I1/S1} \pm \sqrt{B_{N1/I1/S1}^2 - 4 \cdot A_{N1/I1/S1} \cdot C_{N1/I1/S1}}}{2A_{N1/I1/S1}} \quad 2.67$$

$$q^{N2/I2/S2} = \frac{B_{N2/I2/S2} \pm \sqrt{B_{N2/I2/S2}^2 - 4 \cdot A_{N2/I2/S2} \cdot C_{N2/I2/S2}}}{2A_{N2/I2/S2}}$$

where

$$\begin{aligned} A_{N1/I1/S1} &= N^2 \cos^2 \theta_{N1/I1/S1} + M^2 \sin^2 \theta_{N1/I1/S1} \\ A_{N2/I2/S2} &= N^2 \cos^2 \theta_{N2/I2/S2} + M^2 \sin^2 \theta_{N2/I2/S2} \\ B_{N1/I1/S1} &= 2\tilde{\eta}'_R M \sin \theta_{N1/I1/S1} \\ B_{N2/I2/S2} &= 2\tilde{\eta}'_R M \sin \theta_{N2/I2/S2} \\ C_{N1/I1} &= \tilde{\eta}'_{Iv}{}^2 + \tilde{\eta}'_R{}^2 - (E + E_F^{N/I})^2 \\ C_{N2/I2} &= \tilde{\eta}'_{Iv}{}^2 + \tilde{\eta}'_R{}^2 - (E - E_F^{N/I})^2 \\ C_{S1} &= \tilde{\eta}'_{Iv}{}^2 + \tilde{\eta}'_R{}^2 - (\sqrt{E^2 - \tilde{\Delta}^2} + E_F^S)^2 \\ C_{S2} &= \tilde{\eta}'_{Iv}{}^2 + \tilde{\eta}'_R{}^2 - (\sqrt{E^2 - \tilde{\Delta}^2} - E_F^S)^2 \end{aligned} \quad 2.68$$

and all the angles can be obtained from the following expressions,

$$\begin{aligned} \sin \theta_{I1/S1} &= \frac{Nq^{N1} \sin \theta_{N1}}{\sqrt{-C_{I1/S1} + 2M\tilde{\eta}'_R q^{N1} \sin \theta_{N1} + (N^2 - M^2)(q^{N1} \sin \theta_{N1})^2}} \\ \sin \theta_{N2/I2/S2} &= \frac{Nq^{N1} \sin \theta_{N1}}{\sqrt{-C_{N2/I2/S2} + 2M\tilde{\eta}'_R q^{N1} \sin \theta_{N1} + (N^2 - M^2)(q^{N1} \sin \theta_{N1})^2}} \end{aligned} \quad 2.69$$

The wavefunction in the normal, insulator and the superconducting regions can be expressed as,

$$\Psi_N(x) = \begin{pmatrix} 1 \\ W_1 \\ 0 \\ 0 \end{pmatrix} e^{iq^{N1} \cos \theta_{N1} x} + a_\sigma \begin{pmatrix} 0 \\ 0 \\ 1 \\ W_3 \end{pmatrix} e^{iq^{N2} \cos \theta_{N2} x} + b_\sigma \begin{pmatrix} 1 \\ W_2 \\ 0 \\ 0 \end{pmatrix} e^{-iq^{N1} \cos \theta_{N1} x} \quad 2.70$$

$$\Psi_I(x) = l_\sigma \begin{pmatrix} 1 \\ W_4 \\ 0 \\ 0 \end{pmatrix} e^{iq^1 \cos \theta_{11} x} + m_\sigma \begin{pmatrix} 1 \\ W_5 \\ 0 \\ 0 \end{pmatrix} e^{-iq^1 \cos \theta_{11} x} \\ + p_\sigma \begin{pmatrix} 0 \\ 0 \\ 1 \\ W_6 \end{pmatrix} e^{-iq^2 \cos \theta_{12} x} + q_\sigma \begin{pmatrix} 0 \\ 0 \\ 1 \\ W_7 \end{pmatrix} e^{iq^2 \cos \theta_{12} x} \quad 2.71$$

and

$$\Psi_S(x) = c_\sigma \begin{pmatrix} 1 \\ W_8 \\ e^{-i\beta} \\ e^{-i\beta} W_8 \end{pmatrix} e^{iq^{S1} \cos \theta_{S1} x} + d_\sigma \begin{pmatrix} 1 \\ W_9 \\ e^{i\beta} \\ e^{i\beta} W_9 \end{pmatrix} e^{-iq^{S2} \cos \theta_{S2} x} \quad 2.72$$

where a_σ and b_σ denote the amplitudes of the Andreev reflection (AR) and the normal reflection (NR) respectively in the normal lead. l_σ and m_σ are the amplitudes of the incoming and reflected electrons in the insulating region, while p_σ and q_σ are the amplitudes of the incoming and the reflected holes in the insulating region. Further c_σ and d_σ denote coefficients of transmission into the superconducting leads as electron-like quasiparticles and as hole-like quasiparticles. The various

quantities listed in Eqn.((2.70), (2.71), (2.72)) are given by,

$$\begin{aligned}
 W_1 &= \frac{E_F^N + E - \hat{\eta}'_{Iv}}{Mq^{N1} \sin \partial_{N1} - iNq^{N1} \cos \partial_{N1} - \sigma \hat{\eta}'_R} \\
 W_2 &= \frac{E_F^N + E - \hat{\eta}'_{Iv}}{Mq^{N1} \sin \partial_{N1} + iNq^{N1} \cos \partial_{N1} - \sigma \hat{\eta}'_R} \\
 W_3 &= \frac{E_F^N - E - \hat{\eta}'_{Iv}}{Mq^{N2} \sin \partial_{N2} - iNq^{N2} \cos \partial_{N2} - \sigma \hat{\eta}'_R} \\
 W_4 &= \frac{E_F^I + E - \hat{\eta}'_{Iv}}{Mq^{I1} \sin \partial_{I1} - iNq^{I1} \cos \partial_{I1} - \sigma \hat{\eta}'_R} \\
 W_5 &= \frac{E_F^I + E - \hat{\eta}'_{Iv}}{Mq^{I1} \sin \partial_{I1} + iNq^{I1} \cos \partial_{I1} - \sigma \hat{\eta}'_R} \\
 W_6 &= \frac{E_F^I - E - \hat{\eta}'_{Iv}}{Mq^{I2} \sin \partial_{I2} + iNq^{I2} \cos \partial_{I2} - \sigma \hat{\eta}'_R} \\
 W_7 &= \frac{E_F^I - E - \hat{\eta}'_{Iv}}{Mq^{I2} \sin \partial_{I2} - iNq^{I2} \cos \partial_{I2} - \sigma \hat{\eta}'_R} \\
 W_8 &= \frac{E_F^S + \Omega - \hat{\eta}'_{Iv}}{Mq^{S1} \sin \partial_{S1} - iNq^{S1} \cos \partial_{S1} - \sigma \hat{\eta}'_R} \\
 W_9 &= \frac{E_F^S - \Omega - \hat{\eta}'_{Iv}}{Mq^{S2} \sin \partial_{S2} + iNq^{S2} \cos \partial_{S2} - \sigma \hat{\eta}'_R} \\
 \Omega &= \sqrt{E^2 - \tilde{\Delta}^2}
 \end{aligned} \tag{2.73}$$

The wave functions must satisfy the following boundary conditions,

$$\Psi_N(x=0) = \Psi_I(x=0); \quad \Psi_I(x=d) = \Psi_S(x=d) \tag{2.74}$$

From the boundary conditions all the reflection and transmission amplitudes can be obtained. The reflection amplitudes are given by,

$$\alpha_\sigma = c_\sigma N_5 + d_\sigma N_6 \quad ; \quad b_\sigma = c_\sigma N_1 + d_\sigma N_2 - 1 \tag{2.75}$$

where

$$\begin{aligned}
 c_\sigma &= -d_\sigma \frac{W_3 N_6 - N_8}{W_3 N_5 - N_7} & ; & & d_\sigma &= \frac{W_2 - W_1}{N_9(W_2 N_1 - N_3)} & \quad \quad \quad \mathbf{2.76} \\
 N_9 &= \frac{W_2 N_2 - N_4}{W_2 N_1 - N_3} & - & & \frac{W_3 N_6 - N_8}{W_3 N_5 - N_7} \\
 N_8 &= e^{i\beta} W_6 e^{-i(X_4 - X_2)d} \frac{W_7 - W_9}{W_7 - W_6} & + & & e^{i\beta} W_7 e^{-i(X_4 + X_2)d} \frac{W_6 - W_9}{W_6 - W_7} \\
 N_7 &= e^{-i\beta} W_6 e^{i(X_3 + X_2)d} \frac{W_7 - W_8}{W_7 - W_6} & + & & e^{-i\beta} W_7 e^{i(X_3 - X_2)d} \frac{W_6 - W_8}{W_6 - W_7} \\
 N_6 &= e^{i\beta} e^{-i(X_4 - X_2)d} \frac{W_7 - W_9}{W_7 - W_6} & + & & e^{i\beta} e^{-i(X_4 + X_2)d} \frac{W_6 - W_9}{W_6 - W_7} \\
 N_5 &= e^{-i\beta} e^{i(X_3 + X_2)d} \frac{W_7 - W_8}{W_7 - W_6} & + & & e^{i\beta} e^{i(X_3 - X_2)d} \frac{W_6 - W_8}{W_6 - W_7} \\
 N_4 &= W_4 e^{-i(X_4 + X_1)d} \frac{W_5 - W_9}{W_5 - W_4} & + & & W_5 e^{-i(X_4 - X_1)d} \frac{W_4 - W_9}{W_4 - W_5} \\
 N_3 &= W_4 e^{i(X_3 - X_1)d} \frac{W_5 - W_8}{W_5 - W_4} & + & & W_5 e^{i(X_3 + X_1)d} \frac{W_4 - W_8}{W_4 - W_5} \\
 N_2 &= e^{-i(X_4 - X_1)d} \frac{W_4 - W_9}{W_4 - W_5} & + & & e^{-i(X_4 + X_1)d} \frac{W_5 - W_9}{W_5 - W_4} \\
 N_1 &= e^{i(X_3 + X_1)d} \frac{W_4 - W_8}{W_4 - W_5} & + & & e^{i(X_3 - X_1)d} \frac{W_5 - W_8}{W_5 - W_4} \\
 X_1 &= e^{iq^{l1} \cos \vartheta_{l1} d}; X_2 = e^{iq^{l2} \cos \vartheta_{l2} d} & ; & & X_3 = e^{iq^{s1} \cos \vartheta_{s1} d}; X_4 = e^{iq^{s2} \cos \vartheta_{s2} d},
 \end{aligned}$$

The conductance through the graphene based NIS junctions (Kane-Mele junction) can be calculated using the Eqn.((2.23),(2.24),(2.25)).

Chapter 3: Charge transport through NS and NIS junction

Since the development in the point contact spectroscopy technique [120], the studies on normal-superconductor junctions have gained attention for acquiring knowledge of several physical phenomena occurring at the interfaces. We have already discussed that the tunneling spectroscopy at the NS junction, generally known as Andreev-Saint-James (ASJ) spectroscopy is very sensitive to the existence of a small imaginary component in the superconducting order parameter, thus it is the most effective tool to gain information on the superconducting order parameter. In an NS junction with a superconducting lead of anisotropic pairing symmetry, the quasiparticles experience a sign change in the order parameter owing to reflection from the interface. The interference between the incident and reflected quasiparticles gives rise to the formation of Andreev bound states (ABS) [121, 122] near the interface which are responsible for different low-energy conductance characteristics and thus provides the useful information on pairing symmetries. Especially, the zero-bias conductance peaks (ZBCP) in high- T_c cuprates manifest strong dependency on the crystallographic orientation of the interface which can be shown to be relevant for the d-wave pairing symmetry [123]. Further, in the tunneling conductance of Sr_2RuO_4 [124] the presence of broad subgap peaks can also be described in terms of the surface ABS, which usually exist in the chiral p-wave type superconductor [125, 126].

With the advent of spintronics in the recent past, the ability to manipulate the spin degree of freedom with precision, just like the charge degree of freedom has gained prominence. Understanding the phenomenon of spin-orbit coupling (SOC) is central to the development of this emerging field. In low dimensions, particularly, in the context of two dimensional electron gases (2DEG), a system where the surface inversion symmetry is lost, such as InAs etc. [127], Rashba spin-orbit coupling [94] becomes important and hence cannot be neglected. The possibility of being able to tune the strength of Rashba SOC (RSOC) using an external field [42] provides additional impetus. A few studies have been carried out to understand the effect of RSOC in NS junction [116, 117, 128]. In an NS junction the asymmetry in the crystal potential in the normal and superconducting leads gives rise to a potential gradient across the interface which results in the Rashba spin-orbit coupling.

A holistic view towards the work at hand reveals that the conductance properties of an NS junction device can be manipulated by the RSOC. Further the interplay between the RSOC and a few of the physical quantities, that are essentially properties of the interface or the insulating layer or the superconducting leads, renormalize the features of the low energy conductance spectrum. Further,

we emphasize on the distinction in the conductance profile with regard to the different pairing symmetries as the symmetry of the superconducting gap plays a decisive role on the conductance properties of such junctions.

Motivated by the above, we perform an extensive investigation of the conductance characteristics of a normal-superconductor (NS) junction corresponding to different pairing symmetries for the superconducting lead in the presence of RSOC. We are particularly interested in examining an interplay of RSOC with a number of useful parameters that are indispensable in an NS junction device. These parameters include transparency of the interface, finite quasiparticle lifetime, Fermi surface mismatch between the metallic and the superconducting region. We make a mention the experimental relevance and hence the importance of these parameters as we go along discussing the key results. Further, we have studied normal-insulator-superconductor (NIS) junctions where the insulating layer has a finite width. This insulating layer is modeled via an external gate voltage in a way such that the transmission is possible through it. We have extended most of our analysis for the NIS junction as well, and particularly focus on the effect of the interplay of the RSOC parameter and the effective barrier potential which characterizes the insulating layer.

We organize this chapter as follows. The numerical results and their corresponding discussions of the tunneling conductance spectrum of an NS junction with *s*-wave superconducting pairing symmetry are discussed in Section(3.2) and the same for *p* and *d*-wave superconductor appear in Section(3.3). The effect of the Fermi surface mismatch and the finite quasiparticle lifetime on the conductance spectrum are discussed in Sections(3.4) and (3.5) respectively. The results for the NIS junctions are discussed in Section(3.7). We finally conclude with a highlight of our main results in Section(3.8).

3.1 Normal-superconductor junction

We consider a two dimensional NS junction as shown in Fig.(2.1a) where an interface is located at $x = 0$, the left of which being a normal metal (N) with a superconducting (S) lead in the right. The interaction potential everywhere is described by,

$$U_o(x) = U_1 \hat{n} \cdot (\vec{\sigma} \times \vec{k}) \Theta(-x) + U_2 \hat{n} \cdot (\vec{\sigma} \times \vec{k}) \Theta(x) + U_0 \delta_{x,0} \quad 3.1$$

where $\hat{n} = \hat{x}$ is the unit vector along the interface normal, U_0 is the strength of spin independent potential barrier at the interface, U_1 and U_2 are the strengths of the RSOC for normal and superconducting region, $\vec{\sigma}$ are the Pauli matrices, $\vec{k} = -i\vec{\nabla}$ denote the momentum and $\Theta(x)$ is the Heaviside function.

3.2 Results on s-wave pairing symmetry

Before getting ahead with the discussions of our results, we include a note on the values of the parameters used in our numerical computation. To put things in perspective, let us assume some realistic values of Δ_0 , for example $\Delta_0 \sim (10^{-2} - 10^{-3})eV$. Usually E_F^N has values approximately equal to $10^2 - 10^3$ times Δ_0 . As a representative case, we have assumed, $E_F^N = 150\Delta_0$. To see the effects of the RSOC, we have defined a dimensionless quantity, $\hat{\lambda}_R$ which is given by, $\hat{\lambda}_R = U_1 k_F^N / E_F^N = U_2 k_F^S / E_F^S$. The value of the $\hat{\lambda}_R$ is taken in range $[0 : 2]$. In [129] it is shown that the value of the Rashba spin-orbit coupling $2.3eV\text{\AA}$. For this value of the RSOC, $\hat{\lambda}_R$ comes out as ~ 1.18 which is of the same order as considered in our thesis. We borrow all the expressions for our numeric computation from the previous chapter (Chapter 2).

In all our results presented below, we plot normalized conductance, G as appears in Eq.(2.23) (where the actual conductance is normalized by the conductance of pure metallic junctions) as a function of the biasing energy, E scaled by the magnitude of the gap amplitude, Δ_0 . It may be noted that the magnitude of the barrier strength at the interface will decide whether RSOC will enhance or decrease the value of the low energy conductance [130].

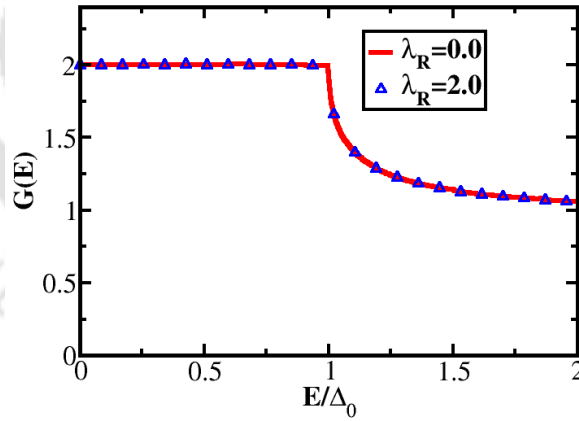


Figure 3.1: The variation of the normalized conductance, G for a s-wave superconductor as a function of E/Δ_0 for different strengths of RSOC with $U_0 = 0$ (transparent barrier). There is no visible effect of RSOC. The value 2 denotes the conductance equal to $4e^2/h$.

In Fig.(3.1), G is shown as function of E/Δ_0 for a s-wave superconductor as the strength of RSOC is varied corresponding to a transparent barrier, that is, $U_0 = 0$. The Fermi energy of the superconducting region is taken as, $E_F^S = E_F^N$. The plots are normalized to a conductance for a metal-metal junction with no interfacial potential (perfect contact) and all the curves have same normalization.

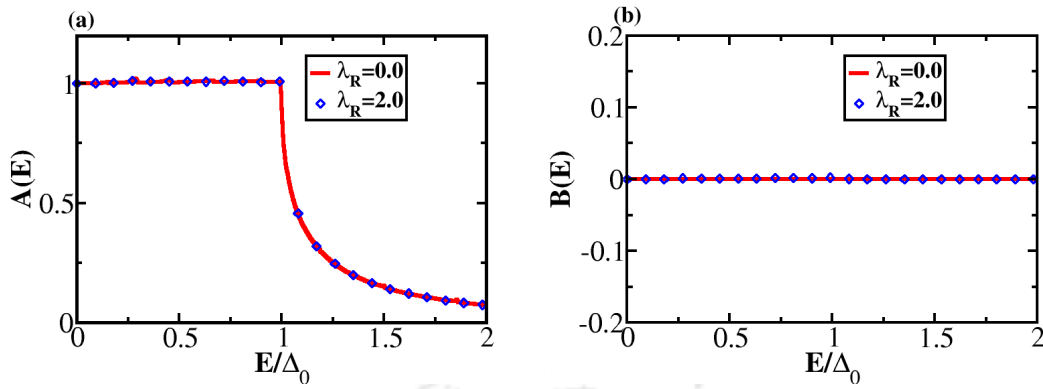


Figure 3.2: The variation of the AR in (a) and NR in (b) for *s*-wave superconductor as a function of E/Δ_0 for a transparent barrier.

In Fig.(3.1), the value of conductance at low energies, namely, $E < \Delta_0$, shows a constant value 2 and for $E > \Delta_0$ it gradually decreases and acquires a value same as that of the metallic junction.

To understand the physics behind this feature it is most convenient to compare the contributions coming from the Andreev reflection (AR) and the normal reflection (NR). Thus we show the variation of the amplitude of AR and NR as the function of the biasing energy in Fig.(3.2). From Fig.(3.2a) it is clear that for transparent case, all electrons with energies $E < \Delta_0$ incident from metallic lead make Cooper pairs near the interface and get transmitted into the superconducting region. As a result, the probability of Andreev reflection is perfectly 1 (see Fig.(3.2a)) and the probability of the normal reflection is nil (see Fig.(3.2b)). Hence, the normalized conductance is obtained as 2.

Now with the inclusion of Rashba spin-orbit coupling, we have observed that the conductance plots remain unchanged irrespective of the strength of RSOC although the momenta of electrons and the holes get modified. Since the junction separating the normal and the superconducting regions is transparent, there is no normal reflection. Hence all the electrons experience Andreev reflection and thus accounts for the normalized conductance value of 2 at low energies ($E \leq \Delta_0$).

Next we show the results for an opaque barrier where we have considered $U_0 = E_F^N$. For the opaque barrier the conductance of the NS junction significantly gets suppressed as large number of the incoming electrons get specularly reflected back into the metallic side and only some of the electrons get Andreev reflected. Further a sharp peak is noted at $E \sim \Delta_0$ as shown in Fig.(3.3). To understand the reason behind this, we have plotted amplitude of the AR and the NR as a function of the biasing energy in Fig.(3.4). With increasing biasing energies, more incoming electrons get transmitted to the superconducting region via Andreev reflection (see Fig.(3.4a)) and the probability of normal reflection gets diminished (see Fig.(3.4b)). As a result, the conductance increases as the biasing energy is

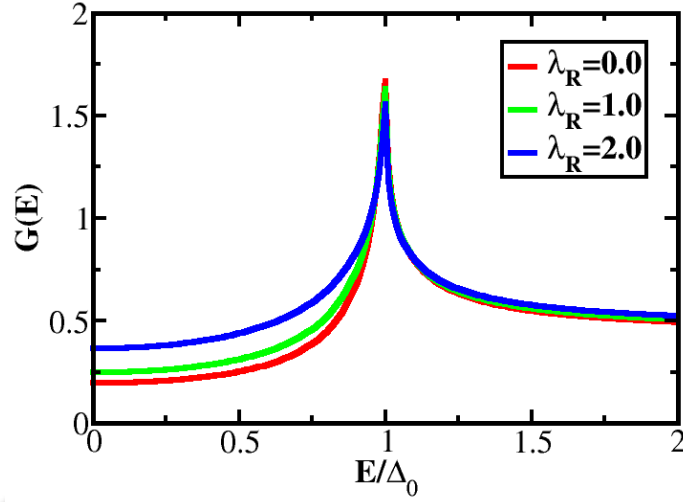


Figure 3.3: The variation of the conductance, G for a s -wave superconductor as a function of E/Δ_0 for different strengths of RSOC with $U_0 = E_F^N$ (opaque barrier).

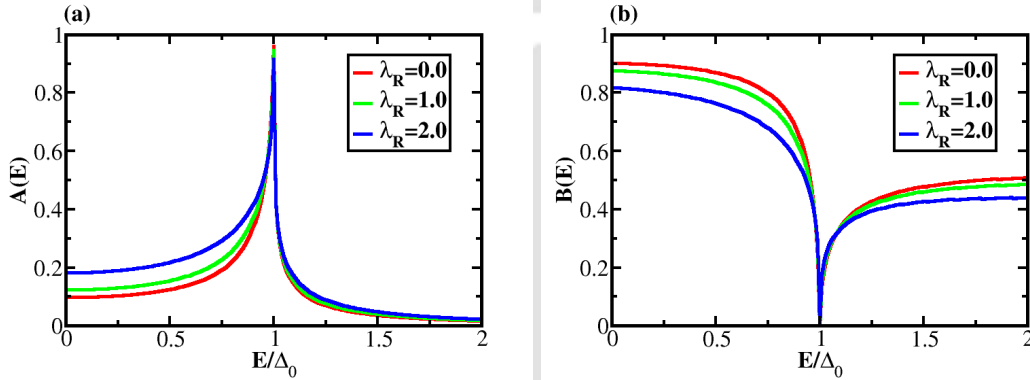


Figure 3.4: The variation of the (a) AR and the (b) NR for a s -wave superconductor as a function of E/Δ_0 for an opaque barrier.

enhanced. When the biasing energy attains a value same as the superconducting gap, that is, $E = \Delta_0$ the maximum number of electrons get Andreev reflected and the probability of normal reflection becomes almost zero. Thus at $E = \Delta_0$ (evident from Fig.(3.3)) a peak is obtained.

Now with the inclusion of the RSOC, the low bias conductance increases, although the enhancement is small, yet noticeable (see Fig.(3.3)). It is evident from Fig.(3.4a) that in case of an opaque barrier, with the inclusion of the RSOC, the probability of AR increases, whereas that of the NR decreases. Thus a scrutiny of Fig.(3.3) yields that RSOC augments the conductance spectrum for a finite opacity ($U_0 \neq 0$). Hence we show the variation of the zero bias conductance, as a function of Rashba strength, $\hat{\lambda}_R$ in Fig.(3.5). It shows the enhancement of the zero bias conductance with increasing strength of the RSOC parameter for an opaque

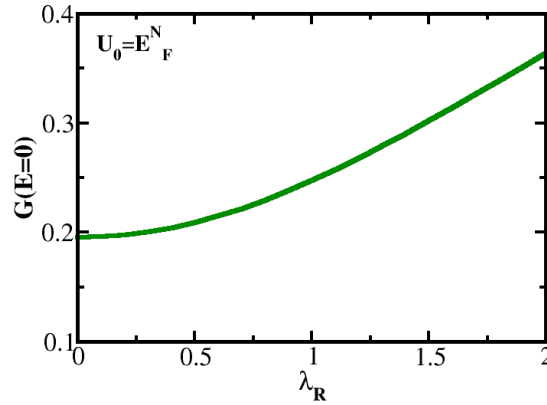


Figure 3.5: The variation of the zero bias conductance, $G(E = 0)$ for a s -wave superconductor as a function of RSOC strength, $\hat{\lambda}_R$.

barrier. We provide a microscopic justification of this feature below.

The transmission of carriers across a NS junction with an opaque barrier, that is, NIS junction, is proportional to the product of the densities of the electronic states of the normal metal and the superconducting materials. With the density of states being a constant for the metal, the transmission through the junction is dominated by the superconducting density of states ($N_S(E)$), where the latter shows a spike at the superconducting gap, Δ_0 (remember $N_S \sim E/\sqrt{E^2 - \Delta_0^2}$). This density of states shows up in the conductance characteristics ($\sim dI/dV$) of the NIS junction via a spike in the spectrum which is identified as the Andreev peak. Thus an enhancement of the AR amplitude (which is followed by suppression of the NR amplitudes) takes place due to gain of the density of states.

Similar explanation will hold throughout our thesis wherever we note an enhancement in the AR amplitude. To make the presentation crisp, we have not provided the above justification each time, and instead alluded to the modifications in AR (and NR) amplitudes to explain the behaviour of the conductance profile.

3.3 Other pairing symmetries

As we have already discussed that the superconducting order parameters has an important role to play in the shape and features of the conductance spectrum, we have considered other pairing symmetries, such as the p -wave and d -wave superconducting correlations. Even though we are mainly concerned with s -wave superconductivity in both NS and NIS junctions, a brief tour to the unconventional pairing scenarios in an exercise of worth due to following reasons. In case of an inhomogeneous superconductor, multiple Andreev reflection leads to the formation of sub-gap states, Andreev bound states corresponding to excitation

energies below the superconducting gap. These states provide different features and thus play a crucial role for understanding the inhomogeneous superconductors. We are particularly interested in examining the interplay of RSOC and the barrier transparency for p - and d -wave superconductors. There is a significant difference in the features of the conductance spectrum for these superconductors compared to that of the conventional s -wave superconductors. We discuss them below.

3.3.1 p -wave superconductor

Here we use the results of our derivation presented in chapter 2. We study the tunneling conductance as the function of E/Δ_0 for a p -wave superconductor in Fig.(3.6a) and Fig.(3.6b) for a transparent and an opaque barrier. Note that, for transparent barrier, $G(E) = 2$ for all subgap energies, $E < \Delta_0$, due to the Andreev reflection occurring with the probability one which is exactly same as that of the s -wave superconductor. But for an opaque barrier case, it shows different features. A broad peak at subgap energies is obtained, which is associated with the surface Andreev bound states (SABS) that exist in chiral p -wave superconductors [126]. It is shown that chiral p -wave superconductors host SABS with a linear dispersion as a function of momentum parallel to the edge, resulting a much broader zero bias conductance peak (ZBCP) [116, 125, 126]. Here we would like to recall that there are no subgap surface bound states in case of a s -wave superconductor, and the tunneling conductance at $E < \Delta_0$ is strongly suppressed in presence of large opacity, that is for large U_0 .

Fig.(3.6a) shows that for transparent case with the inclusion of Rashba spin-orbit coupling there is no change in conductance although the momenta of the electrons and holes are modified. Same conclusion as earlier can be drawn here; since there is no barrier between the normal and the superconducting regions, all electrons experience Andreev reflection and the hence the probability of normal reflection is perfectly zero. Thus the normalized conductance at $E < \Delta_0$ shows the value 2. But for an opaque barrier Fig.(3.6b), with increasing strength of RSOC, the conductance increases. Here also, for an opaque barrier with the inclusion of RSOC, the amplitude of AR increases and the amplitude of the NR decreases. Thus the RSOC contributes in enhancing the conductance. Further, it is understood that, with the inclusion of RSOC, the surface ABS is not affected which is the signature of the p -wave pairing symmetry.

3.3.2 d -wave superconductor

Next we study the tunneling conductance as the function of E/Δ_0 for a d -wave superconductor in Fig.(3.7). It may be noted from Eq.(2.8) that the d -wave order

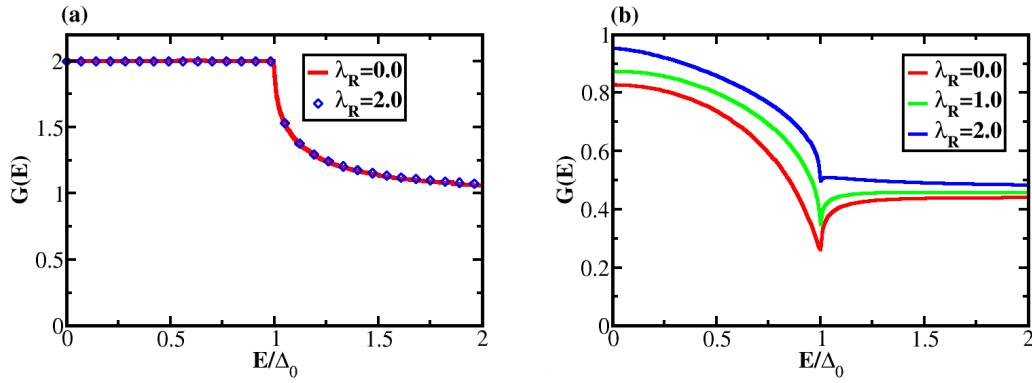


Figure 3.6: The variation of the conductance, G for a p -wave superconductor as a function of E/Δ_0 for different strengths of RSOC for (a) $U_0 = 0$ (transparent barrier) and (b) $U_0 = E_F^N$ (opaque barrier).

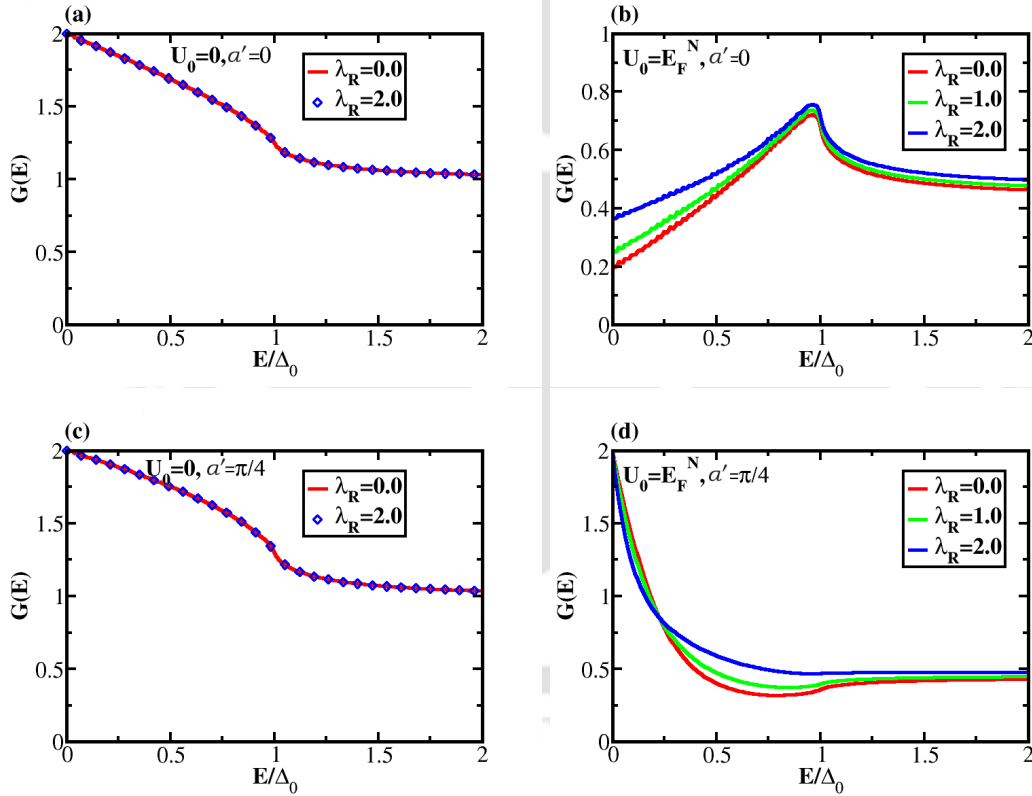


Figure 3.7: The variation of the conductance, G for a d -wave superconductor as a function of E/Δ_0 for different strengths of RSOC with (a) $a' = 0$ and $U_0 = 0$, (b) $a' = 0$ and $U_0 = E_F^N$, (c) $a' = \pi/4$ and $U_0 = 0$, (d) $a' = \pi/4$ and $U_0 = E_F^N$.

parameter can have any arbitrary phase (given by a' (see Fig.(2.1b))). For concreteness, one can consider $a' = 0, \pi/4$ etc. Here we study the conductance characteristics for a d -wave superconductor with $a' = 0$ and $a' = \pi/4$ (for definition of a' , see Fig.(2.1)b). Fig.(3.7a) and Fig.(3.7b) show the conductance characteristics with $U_0 = 0$ and $U_0 = E_F^N$ for $a' = 0$. In Fig.(3.7c), Fig.(3.7d) we consider $a' = \pi/4$

case.

In case of a transparent barrier, the tunneling conductance for both the $a' = 0$ and $a' = \pi/4$, there is only Andreev reflection and $G(E)$ is nearly independent on a' and monotonically decreasing from 2 as E increases. Now with the inclusion of RSOC, there is no change in conductance for both $a' = 0$ and $a' = \pi/4$ as there is no specular reflection. One may notice an interesting fact that s and d -wave superconductors show dissimilarities in their conductance profile though both correspond to singlet Cooper pairing. In case of s -wave superconductor, the electrons with different incident angles are subjected to an isotropic gap in the superconducting region. We find that in case of an opaque barrier, for all incident angles, the contribution of the AR is maximum and along with the contribution of the NR being minimum at $E \sim \Delta_0$. So when we integrate the conductance for all incident angles, we get a large value of the conductance peak at $E \sim \Delta_0$. But for a finite opacity, in the case of a d -wave superconductor with $a' = 0$, the electrons with different incident angles experience different superconducting gaps (see Eq.(2.8)). So the electrons with different incident angles show maximum contributions at different biasing energies. Therefore the contribution to the conductance coming from different incident angles yield a reduced value for the AR peak at $E = \Delta_0$ (see Fig.(3.7b)). Hence, while the s -wave superconductor has a sharp peak at $E \sim \Delta_0$, the d -wave shows a moderate peak.

The situation is further different for the d -wave superconductor corresponding to $a' = \pi/4$ and opaque barrier. A sharp peak is obtained for this case. Here we obtain a maximum value at $E = 0$ owing to the fact that the contribution of the AR is maximum at $E = \Delta_0$. It is known that the tunneling conductance characteristics for a d -wave case corresponding to $a' = \pi/4$ host a peak at zero energy. It is known as zero bias conductance peak (ZBCP) which is a signature of zero energy surface Andreev boundstates (SABS) [122, 131-133]. It can be shown that ZBCP occurs at $a' = \pi/4$ for all incident angles due to the fact that $\Delta_+ = -\Delta_-$ [128, 134].

Now with the inclusion of RSOC for an opaque barrier, we find that for $a' = 0$, the conductance increases with increasing RSOC, while for $a' = \pi/4$, it increases with increasing RSOC after a certain threshold value of the biasing energy. The only exception is observed for the d -wave superconductor corresponding $a' = \pi/4$.

All of these results have a natural explanation from the behavior of the AR and NR amplitudes, a_σ and b_σ respectively, which are functions of energy, RSOC, barrier transparency, the asymmetry angle of the d -wave parameter and various other parameters that are going to be discussed in the subsequent sections. In Eq.(2.25), a larger a_σ enhances G_σ , while a larger b_σ is detrimental for it. As we have emphasized earlier, there is no *a priori* intuition how the interplay of these factors with RSOC behave in deciding the behavior of conductance at $E \sim 0$ (that is much less than Δ_0) and $E \sim \Delta_0$.

As said earlier, it can be seen that the conductance profiles as the function of E/Δ_0 for different symmetries of the superconducting order parameters are different. The difference is due to the fact that corresponding to different pairing symmetries, the AR becomes maximum and NR becomes minimum at different values of E/Δ_0 . But for all the superconducting order parameter symmetries, discussed here, the dependence of the tunneling conductance on the RSOC are almost identical.

3.4 Fermi surface mismatch

Usually for Andreev reflection across NS junction experiments, the properties of the Fermi surfaces in both sides of the contact are distinct. Particularly, the Fermi energy in a normal metal depends on the density of the charge carriers present, while the Fermi level dependence enters through the density of states (DOS) at the Fermi energy ($N(E_F)$) in the expression of the transition temperature in conventional superconductors (recall the BCS expression, $T_c \sim \hbar\omega_D e^{-1/N(E_F)V}$), ω_D being the Debye frequency and V is the (infinitesimal) interparticle interaction). Thus the Fermi energy appearing in the BTK expressions for conductance should naturally be different [135]. However, whether and how that affects the conductance characteristics and competes with the RSOC is a topic that needs to be understood. Thus in our work we have considered a parameter $\hat{\eta}$ which denotes the ratio of the Fermi energies in either side of the contact (interfacial region) (E_F^S/E_F^N) and addressed the interplay of $\hat{\eta}$ and the RSOC on the conductance behaviour. In our work we have kept E_F^N to be a constant and varied E_F^S . Physically it

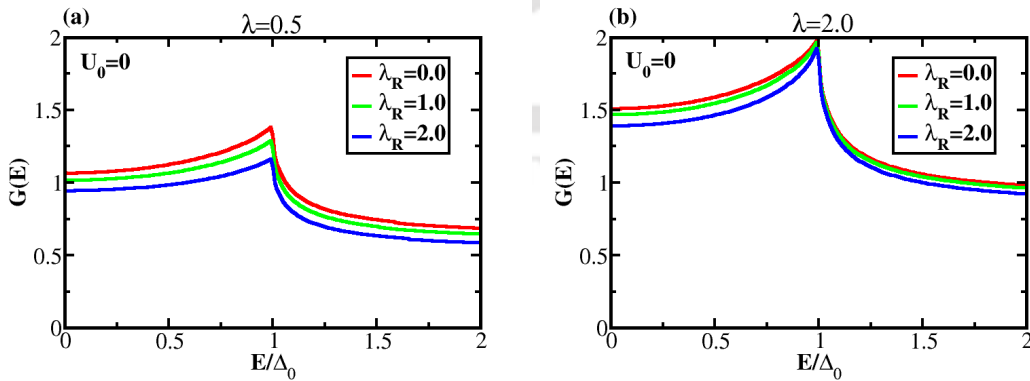


Figure 3.8: The variation of the conductance, $G(E)$ for a s -wave superconductor as a function of E/Δ_0 for (a) $\hat{\eta} = 0.5$, (b) $\hat{\eta} = 2$ with a transparent barrier ($U_0 = 0$).

implies keeping the metallic lead unaltered, while one works with different superconducting materials. Thus a competition between two different (namely, RSOC and $\hat{\eta}$) parameters in the two regions is studied on the conductance properties

of a junction. We note that the difference between the Fermi energies imposes a constraint on the angular aperture contributing to the transmission of carriers and hence to the the integral in Eq.(2.24).

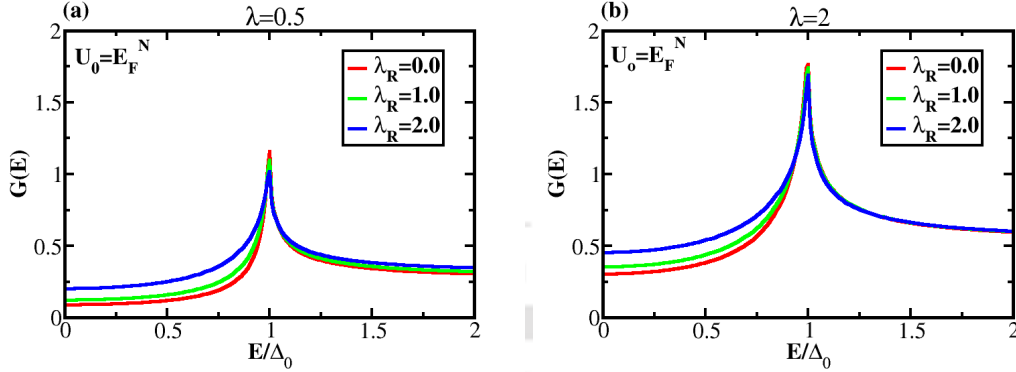


Figure 3.9: The variation of the conductance, $G(E)$ for a s -wave superconductor as a function of E/Δ_0 for (a) $\hat{\eta} = 0.5$, (b) $\hat{\eta} = 2$ with an opaque barrier ($U_0 = E_F^N$).

We discuss the case for $\hat{\eta} \neq 1$ (denoted as Fermi energy mismatch) on the tunneling conductance, in two cases, namely, $\hat{\eta} = 0.5$, and 2 for both transparent and opaque barrier. Fig.(3.8) shows the variation of $G(E)$ versus E/Δ_0 for a s -wave superconductor corresponding to transparent barriers and the scenario for the opaque barrier is shown in Fig.(3.9). So considering different Fermi energies for the carriers in the normal region and in the superconducting region, for a transparent barrier we get different nature for the conductance profile than that are obtained earlier (see Fig.(3.1)). In case of a transparent barrier, for same values of Fermi energies (no mismatch) in either side of the contact, there is no normal reflection, whereas for different Fermi surface the electrons experience the normal reflection at the interface. As a result, the conductance decreases. The figures in Figs.(3.8) and (3.9) reveal that the conductance enhances with increasing $\hat{\eta}$. We understand this as follows, for $E_F^S < E_F^N$ and for some certain values of ∂_{N1} , the ratio $\frac{k_{N1}}{k_{S1}}$ yields $\sin \partial_{S1} > 1$, which is unphysical. Thus for the above condition, there will not be any transmission into the superconducting region and hence will not contribute to the conductance. Due to this fact, $\hat{\eta} > 1$ case (that is $\hat{\eta} = 2$) shows more conductance compared to that of the $\hat{\eta} < 1$ ($\hat{\eta} = 0.5$) case.

Now with the inclusion of RSOC, for the transparent case, the conductance decreases and for the opaque barrier the conductance increases. To see what happens to the the AR and NR amplitudes for both the cases corresponding to transparent and opaque barrier with Fermi surface mismatch, we have plotted the AR and NR amplitudes as a function of biasing energy in Fig.(3.10) for a specific value of $\hat{\eta}$, namely $\hat{\eta} = 2$. However the results are true for both $\hat{\eta} = 0.5$ and 2. It is obtained that RSOC diminishes the AR amplitude and enhances the NR amplitude for transparent barrier, whereas for an opaque barrier the reverse

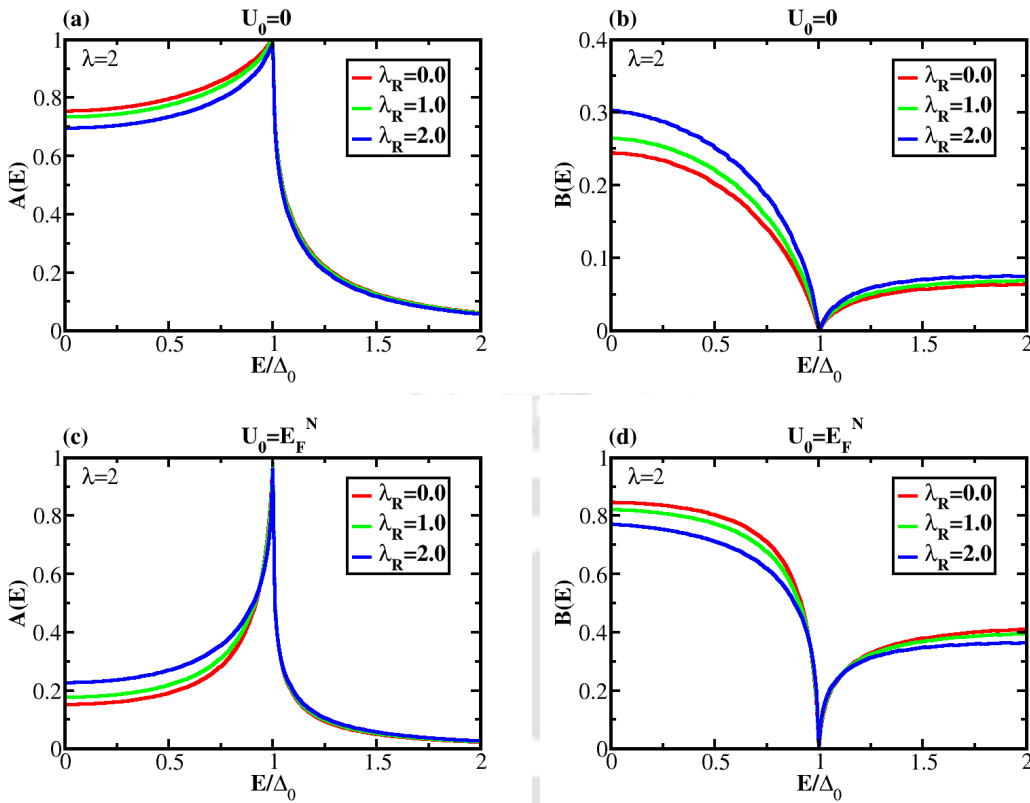


Figure 3.10: The variation of the (a) AR and (b) the NR for a s -wave superconductor as a function of E/Δ_0 for a transparent barrier ($U_0 = 0$), the variation of the (c) AR and (d) the NR for a s -wave superconductor as a function of E/Δ_0 for an opaque barrier ($U_0 = E_F^N$).

trends are obtained (that is, RSOC enhances the AR amplitude and suppresses the NR amplitude). Thus it justifies the results obtained in Fig.(3.8) and Fig.(3.9). It is clear from the ongoing discussion how the magnitude of the barrier strength at the interface decides whether RSOC enhances or diminishes the magnitude of the low energy conductance.

3.5 Finite quasiparticle lifetime

Quasiparticle lifetime is defined as the rate at which the quasiparticles decay, especially in disordered superconductors, is an important quantity that characterizes the nature of superconducting state [136]. It was shown the conductivity data of disordered MoC superconducting films [137] can only be satisfactorily explained by invoking a finite quasiparticle lifetime, τ_{QP} which is defined as,

$$\Gamma \sim \frac{1}{\tau_{QP}}$$

3.2

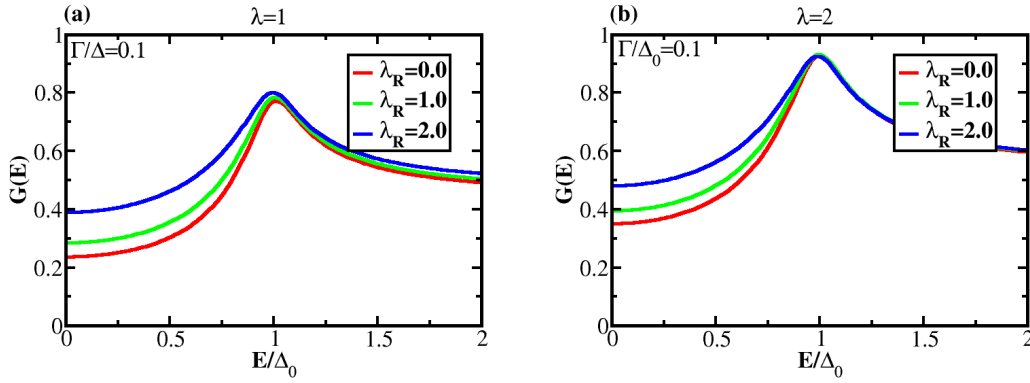


Figure 3.11: The variation of the conductance, $G(E)$ for a s -wave superconductor as a function of E/Δ_0 for an opaque barrier with (a) $\hat{\eta} = 1$ and (b) $\hat{\eta} = 2$.

where Γ renormalizes the quasiparticle energies, E by $E \pm i\Gamma$ [138, 139]. Without any loss of generality, we have considered only the positive sign in our thesis.

It should not be *a priori* evident how an inclusion of Γ (or τ_{QP}) can interfere with the RSOC present in the metallic lead and hence whether help or hinder the low energy conductance features of a NS junction. It is nevertheless predictable that a finite Γ would broaden the AR peak and bring down the peak conductance. With the insertion of finite quasiparticle lifetime, all expressions containing energy, E are renormalized as mentioned above and subsequently they are to be plugged in relevant equations to compute the conductance. In Fig.(3.11) we show the variation of G for an opaque barrier ($U_0 = E_F^N$) for a representative value of $\Gamma/\Delta_0 = 0.1$ for a s -wave superconductor. This value of Γ/Δ_0 is comparable with the value quoted in Ref. [35] for CeCoIn_5 which is a heavy fermion superconductor with a d -wave order parameter symmetry. In fact various parameters are shown to be, $\Delta_0 = 600\mu\text{eV}$, $\Gamma = 95\mu\text{eV}$. A comparison with Fig.(3.3) indicates that finite quasiparticle lifetime affects the conductance peak which broadens and the peak value diminishes. With the insertion of finite quasiparticle lifetime, the dependence of conductance spectrum on RSOC does not alter. The transparent case is an idealized version and hence left out discussion.

3.6 Normal-superconductor junction (NS) with interfacial RSOC

Here we would like to mention that we have also studied the NS junction with RSOC being present at the interface of the junction. The results obtained for the NS junction with interfacial RSOC are qualitatively almost similar as the results presented here. Only difference lies in case of a transparent barrier. For a transparent barrier, in presence of an interfacial RSOC, the low energy conductance

gets significantly suppressed and a sharp peak is obtained at $E = \Delta_0$ (for s -wave superconductor), whereas with no interfacial RSOC there is no change in the conductance features. The information of the interfacial RSOC enters in the AR and NR amplitudes through the boundary conditions as the derivative of the wave function is no longer continuous. Thus the interfacial RSOC acts as a discontinuity (δ -function potential barrier) at the interface which essentially enhances the normal reflection and diminishes the Andreev reflection components. Thus the conductance significantly decreases [140].

3.7 Normal-insulator-superconductor junction

Here we have considered a two dimensional NIS junction setup as shown in Fig.(2.2) where the normal region and the superconducting region occupy, $x \leq 0$ and $x \geq d$ respectively with the insulating region extending from $x = 0$ to d . The $x \leq 0$ and $x \geq d$ regions denote the electrodes that carry current through the junctions. The interfaces of this NIS junctions are located at $x = 0$ and $x = d$. The corresponding potential variation as a function of distance along the x - axis is given by,

$$U_\sigma(x) = U_1 \hat{n} \cdot (\vec{\sigma} \times \vec{k}) \Theta(-x) + U_2 \hat{n} \cdot (\vec{\sigma} \times \vec{k}) \Theta(d - x) + U_3 \hat{n} \cdot (\vec{\sigma} \times \vec{k}) \Theta(x - d) \quad 3.3$$

Generally to define the insulating layer the Fermi energy is considered as, $E_F^I = E_F^N - V_0$ [141]. But if the barrier potential V_0 is very high, the conductance through the junction get significantly suppressed [38]. So to overcome this issue, we have modeled the insulating barrier by an external gate voltage such that, E_F^I is ramped by the gate voltage and can be written as, $E_F^I = E_F^N + V_0$ [119]. In this case, for larger values of V_0 also, the transmission is possible.

Thus the Fermi energy $E_F(x)$ across the junction is given by,

$$E_F(x) = E_F^N \Theta(-x) + (E_F^N + V_0) \Theta(d - x) + (E_F^N + V_1) \Theta(x - d) \quad 3.4$$

where E_F^N , $E_F^I (= (E_F^N + V_0))$ and $E_F^S (= (E_F^N + V_1))$ are the Fermi energies of normal, insulating and superconducting regions respectively. and V_1 is a potential in the superconducting region which is used to tune the Fermi surface mismatch between the metal and superconducting regions.

3.7.1 Results and discussions

Before discussing the results on conductance characteristics of an NIS junction with the Fermi energy of the insulating layer as, $E_F^I = E_F^N + V_0$, we will show the results for conventionally modeled NIS junction, that is $E_F^I = E_F^N - V_0$, where

the value of the V_0 has been considered as $V_0 = 0.8E_F^N$. In the numeric computation we have considered a finite quasiparticle life time and the Fermi wavevector mismatch ($\beta \neq 1$) for the carriers. In particular, we have considered $\Gamma/\Delta_0 = 0.1$ and $V_1 = E_F^N$. Fig.(3.12) shows that in an NIS junction the conductance is severely

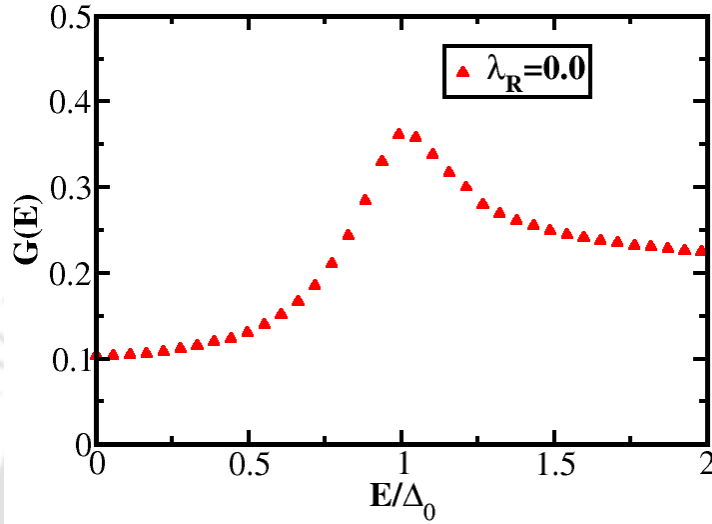


Figure 3.12: The variation of the conductance, G for a s -wave superconductor as a function of biasing energy, E/Δ_0 for a conventional NIS junction.

suppressed by the insulating layer between the metallic and superconducting region. Further, if the barrier potential V_0 becomes larger than the E_F^N , then there is no transmission through the junction. To overcome this issue, we have modeled the insulating layer in a way by an external gate voltage, such that the Fermi energy of the insulating layer is ramped by V_0 and transmission is possible through the NIS junction. Physically it means that the external gate voltage causes the local breakdown of the insulating properties of the barrier.

Now we show the results of NIS junction with the external gate voltage across the insulating layer that helps the transmission through the NIS junction. Here we discuss the results only for a s -wave superconductor. We introduce a dimensionless quantity which we will call as effective barrier potential, $\chi = k_F^I d$, where k_F^I is the Fermi wave vector and d is the barrier width of the insulating region. The Fermi wave vector of the insulating region is proportional to, V_0 (see Eq.(3.4)). As we shall see, this effective barrier potential, $\chi \sim \sqrt{V_0}d$ is going to play a key role in the subsequent analysis.

In Fig.(3.13), the tunneling conductance, G is shown as function of χ for a s -wave superconductor as the RSOC strength is varied. We can see that the tunneling conductance oscillates as the effective barrier potential increases irrespective of the presence of the Rashba coupling. These oscillations in conductance

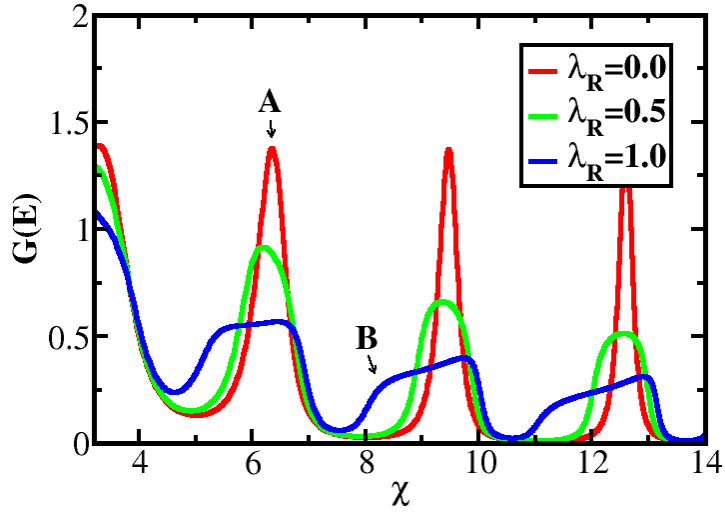


Figure 3.13: The variation of the conductance, G for a s -wave superconductor as a function of χ ($k_F^l d$) corresponding to zero bias condition ($E/\Delta_0 = 0$) for different strengths of RSOC. The other parameters are $V_1 = E_F^N$, $\Gamma/\Delta_0 = 0.1$.

profile correspond to Fabry Perot- like oscillations observed in various junction devices [119, 142, 143]. In fact, the oscillation frequency of the conductance profile depends on the parameters of the insulating region lying between the normal and the superconducting leads.

The periodic behavior of conductance as a function of χ can be explained from the definition of P_i 's (see Eqn.(2.40)) and is suggestive of obtaining a desired value of conductance for a certain value of the effective barrier potential. In a Fabry-Perot (FP) interferometer, the phenomenon of multiple beam interference takes place when a photon bounces back and forth between two semi-transparent parallel surfaces. Each time the photon rebounds from one of the surfaces, a portion of it is reflected back, and the remaining is transmitted. So a single beam splits into multiple beams which interfere with each other and provide an oscillatory intensity profile for the transmitted beam as the separation of the two surfaces (or even the light intensity) is varied. In solid state physics, the same phenomenon, that is, the electrons interfere while they travel between the two interfaces and thus create the oscillations in the conductance spectrum as a function of the distance between the two interfaces or the barrier potential between the two interfaces (or a product of both). Similar oscillations are obtained in our conductance profile due to both electron interference. The Rashba coupling has an interesting effect on the conductance profile. Fig.(3.13) reveals that Rashba coupling modulates the interference pattern in an interesting way. RSOC broadens the conductance peaks and the peak value diminishes. As the strength of RSOC is made larger,

there is shift in minima and maxima (peak) positions.

Let us see how authentic are our envisions made on the conductance oscillations. We shall consider realistic values to examine the predicted periodicity of the conductance and its dependence for the junction parameters that are similar in magnitude with those mentioned in experiments. For a Fermi energy, E_F to have a value of few eV , the Fermi wavevector can be obtained using, $k_F = \sqrt{\frac{2mE_F}{\hbar^2}}$. Taking $E_F \sim 1eV$ and m same as the bare electronic mass, k_F comes out as $5.14 \times 10^9 m^{-1}$. So if the width of the insulating region is a few nanometres, then the product of the Fermi wave vector and the width of the insulating region, that is, $k_F^I d$ has an approximate (dimensionless) value of 5. In our computation, we have chosen the values of χ over a slightly broader range, namely, [3 : 14]. Thus the parameters used for our computation here correspond to experimentally relevant values and hence can be verified in experiments. In this context, we would like to mention that in our work we have fixed the width of the barrier region, and varied the external gate voltage across the insulating layer. That is why the quantity χ starts from a non-zero value.

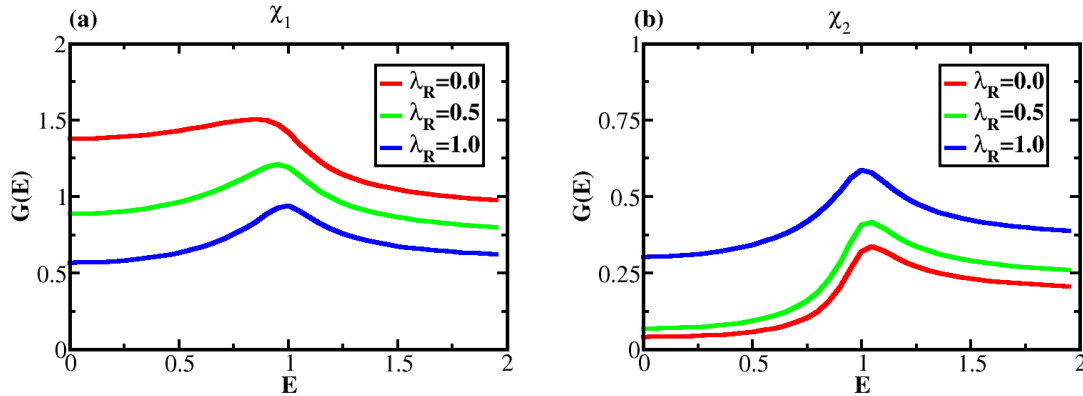


Figure 3.14: The variation of the conductance, G for a s -wave superconductor as a function of E/Δ_0 for different strengths of RSOC for two values of the χ , namely, (a) χ_1 and (b) χ_2 .

Now we show the conductance as the function of biasing voltage, E , (in units of the superconducting gap, that is, E/Δ_0) for different values of RSOC for two different regions of the effective barrier potential, χ_1 and χ_2 in Fig.(3.14). χ_1 denotes the values of effective barrier potential where the peaks of the (RSOC free) conductance occur and χ_2 denotes the effective barrier potentials where the minima of the conductance (RSOC free) are located. Specifically, we focus on region A (χ_1) and region B (χ_2) (shown in Fig.(3.13)). These values of χ show contrasting features, that is, for an effective barrier potential to have a value, say, χ_1 , the value of conductance decreases with RSOC, whereas for χ_2 the reverse happens. The reason behind these feature can be explained from Eqn.(2.40). We know that

the conductance is the function of AR and NR amplitudes and these amplitudes are functions of the P_i 's (see Eqn.(2.40)). We may assume that, the P_i functions have a phase part (exponential term) and an amplitude part. Now with the inclusion of RSOC both of them will change because the momenta involved in all x_i 's are now modified in presence of RSOC. As a result, the peak positions shift and peak values change. The interesting fact is that the modulation of oscillation patterns in presence of RSOC is such that, in certain ranges of the effective barrier potential, RSOC enhances the conductance, and for other ranges it diminishes the conductance. Thus it is evident that the magnitude of the effective barrier potential decides whether RSOC will enhance or decrease the value of the conductance through a NIS junction. Hence we show the variation of the tunneling

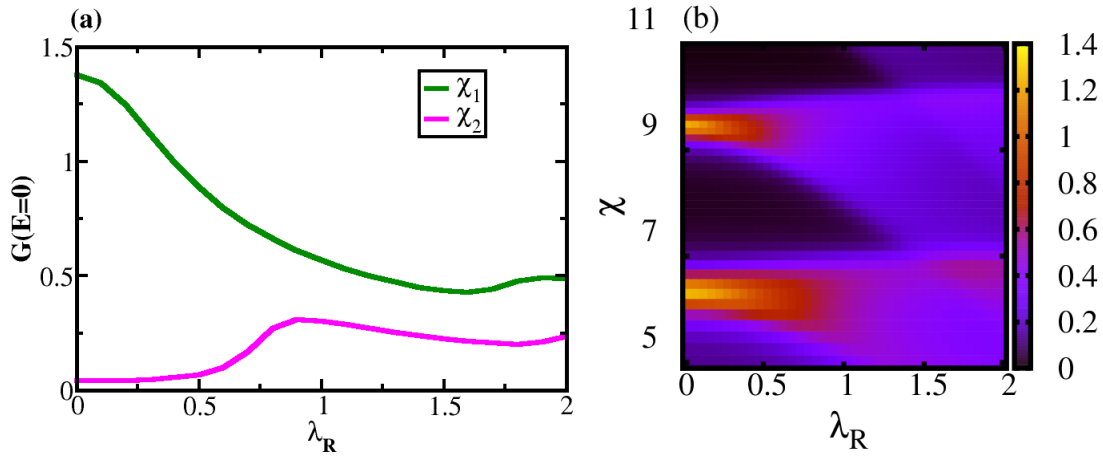


Figure 3.15: (a) The variation of the conductance, $G(E = 0)$ for a *s*-wave superconductor as a function of RSOC strength λ_R , (b) the color maps of the zero bias conductance ($G(E = 0)$) as the function of λ_R and χ .

conductance, G as a function of Rashba strength, λ_R for different values of χ in Fig.(3.15a). The features reveal that for the effective barrier potential to be χ_1 , the RSOC diminishes the tunneling conductance and for χ_2 , it enhances the conductance. In Eq.(2.25), for the barrier potential to be χ_1 , with increasing RSOC, the contribution of the AR amplitude (the term coming from a_o) decreases and the amplitude of the NR contribution (the term coming from b_o) increases. But for χ_2 , where the tunneling conductance increases with RSOC, the reverse happens. That is, the amplitude of NR decreases and the amplitude of AR increases. Thus a scrutiny of Fig.(3.15) yields that the Rashba free case dominates when the effective barrier potential lies in the vicinity of χ_1 . Similarly for the points in the vicinity of χ_2 , the RSOC augments the conductance spectrum. Further we have shown the colour map of the zero bias conductance as the function of both RSOC strength and the effective barrier potential, χ in Fig.(3.15b), where the oscillation features as the function of χ and the conductance variation as the function of

RSOC which are discussed above are clearly visible. These results are summarized in Table.(3.1) where the behavior of amplitudes of AR and NR with RSOC are tabulated. So the dependency of the tunneling conductance on the RSOC strength is crucially dependent on the effective barrier potential.

Table 3.1: *Behavior of amplitudes of the Andreev reflection (AR) and the normal reflection (NR) with RSOC strength.*

case	χ_1	χ_2
AR	Decreases with RSOC	Increases with RSOC
NR	Increases with RSOC	Decreases with RSOC

If we look into the Eq.(2.25), it is clear that a larger a_σ enhances G_σ , while a larger b_σ decreases it. So all our results can be explained from the behavior of AR and NR amplitudes. We must emphasize that there is no *a priori* intuition how the interplay of this factor, namely χ with RSOC shall ascertain the behavior of the conductance.

3.8 Conclusions

We shall now highlight the key results obtained by us. It is clear that for a transparent barrier, if there is no Fermi surface mismatch, the conductance is not responsive to the Rashba coupling for all pairing symmetries. But in presence of a Fermi surface mismatch, the conductance is sensitive to RSOC. For a transparent barrier with the Fermi surface mismatch, RSOC diminishes the low energy conductance for all pairing symmetries, whereas for an opaque barrier case, RSOC enhances the low energy conductance, irrespective of taking into account of the Fermi surface mismatch. For different pairing symmetries, the conductance as a function of the biasing energy shows different behaviour, in the sense that the conductance peaks occur at different energies for different pairing symmetries and thus the tunneling spectroscopy of an NS junction is an effective tool to acquire information on the superconducting leads. We also find that the tunneling conductance depends on the quasiparticle lifetime. It broadens the conductance peaks and diminishes their values.

Besides, we have investigated the tunneling conductance of a device consisting of a NIS junction. The key results can be highlighted as follows. We observe an oscillatory behavior for the tunneling conductance spectrum as a function of the effective barrier potential (containing both V_0 and d). The spin-orbit term shows interesting effect on the oscillation pattern, in the sense that it shifts the minima and maxima positions. The modification of the oscillation patterns is such that, in some region of the effective barrier potential, RSOC enhances the conductance,

while for others it diminishes the same. These results are shown to have a simple explanation in terms of amplitudes of the normal and Andreev reflections.

As stated earlier, the strength of the RSOC and the effective barrier potential can be tuned using an external gate voltage. Hence our studies on the conductance spectrum have the prospects of being important inputs to the experimental studies which aim to achieve desired conductance of an NS or NIS junction devices.



Chapter 4: Thermoelectric properties of NIS junction

The phenomenon of quantum transport through the junction devices has generated a tremendous wave in the multidisciplinary research for developing electronic devices based on nano-structures. Currently thermoelectric junctions are gaining increased attention due to the recent measurement of the Seebeck coefficient [11–14] in small scale junction devices. Measurement of the Seebeck coefficient provides a useful experimental approach to exploring the electronic structure of the molecules bridging the electrodes. In the past, a growing number of studies on junction devices in the field of thermometric, thermoelectric, solid state cooling and shot noise have been carried out in details [15–18]. The normal metal-insulator-superconductor (NIS) junction devices have interesting applications in these fields and they have been used in a wide range of experiments and applications [8, 10]. Since the temperature range of the superconductor based junction device for application purposes is limited by the transition temperature of the superconducting sample, this junction device is mainly for low temperature applications.

The current progress in the field of thermoelectric physics offers a new perspective for the creation of self-cooling nano devices. Since cooling and preservation of materials are the most important concerns of industries, fabrication of low cost cooling devices are of paramount significance. The technological advancement in enhancing heat transfer that facilitates a cooling effect in different industrial applications has grown in leaps and bounds. In various sectors, such as aerospace, automobile, electronic industries, nuclear reactors and fuel cells, efficient cooling techniques can contribute immensely to important technical improvements. Influenced by the importance of enhancement of heat transfer, we study a different mechanism to achieve tunable cooling using nano-scale junction devices.

The achievement to attain extremely low temperatures and advancement in the miniaturization of devices started the search for on-chip solid state refrigerator [144] which can be useful for sensors cooled to temperatures near 100mK in many next generation analytical and astronomical equipment. For example, such a refrigeration is used to cool germanium thermometer and high energy resolution detector in space [145]. In sub-kelvin range, the solid state cooling is mainly based on quantum mechanical tunneling through superconductor based junction devices. When this junction is biased at a voltage near the superconducting gap energy, the thermal current of the charge carriers removes heat from the cold- temperature reservoir and thus further cools the cold reservoir. Thus these junctions can be used to create very low temperature thermoelectric refrigerators.

The superconducting energy gap provides an energy selective cooling in this

context. This heat transfer through the junction enables the refrigeration that can cool electrons from 300mK to $\sim 100\text{mK}$ [146] and this phenomenon is used in different devices like high sensitivity detectors and quantum devices [147]. The performance of these refrigerators is somewhat limited owing to the competitive process, such as the heat removed from the normal metal and heating of the superconductor, thereby running the risk of destruction of superconductivity.

The violation of the surface inverse symmetry at the interfaces of the junction induces Rashba spin-orbit coupling (RSOC) across the interfacial region. Since both the electric charge and the thermal current are very sensitive to the strength of RSOC, and owing to the tunability of RSOC parameter, a Rashba coupled NIS junction may be a good candidate for fabrication of tunable thermoelectric cooling devices.

Motivated by the above, we perform an extensive investigation of thermoelectric properties and the performance of a NIS junction in the presence of RSOC. We are particularly interested in examining an interplay of RSOC term with the effective barrier potential pertaining to the insulating regime.

The chapter is organized as follows. In Section(4.1) we provide a derivation of the formula for the current flowing through the junctions by using a modified BTK approach. The calculation of the Seebeck coefficient is described in Section(4.1.1). The theory of thermoelectric nano-refrigeration and the working principles for the refrigeration phenomena are presented in Section(4.1.3). The results on the Seebeck coefficient and the corresponding discussions are in Section.(4.2). In Subsection(4.2.1) we present the results on the efficiency of the system as a thermopower device. In Section(4.3) we present the results of the thermoelectric cooling and their corresponding discussions. The results on the performance of this junction device as a nano refrigerator are discussed in Subsection(4.3.1). In Section(4.4) we summarize our results and highlight our findings.

4.1 Charge and thermal current through NIS junction

We consider a two dimensional setup of NIS junction as shown in Fig.(4.1). The normal region and superconducting regions occupy $x \leq 0$ and $x \geq d$ respectively where the insulating region extends from $x = 0$ to d . The $x \leq 0$ (normal electrode) and $x \geq d$ (superconducting electrode) are maintained at different temperatures, $T^N = T - \delta T/2$ and $T^S = T + \delta T/2$ respectively. The interfaces of the NIS junctions are located at $x = 0$ and $x = d$. As we already discussed that due to the difference in crystal potential in the metallic, insulating and superconducting regions, there will be the presence of Rashba spin-orbit coupling across the interface. The form

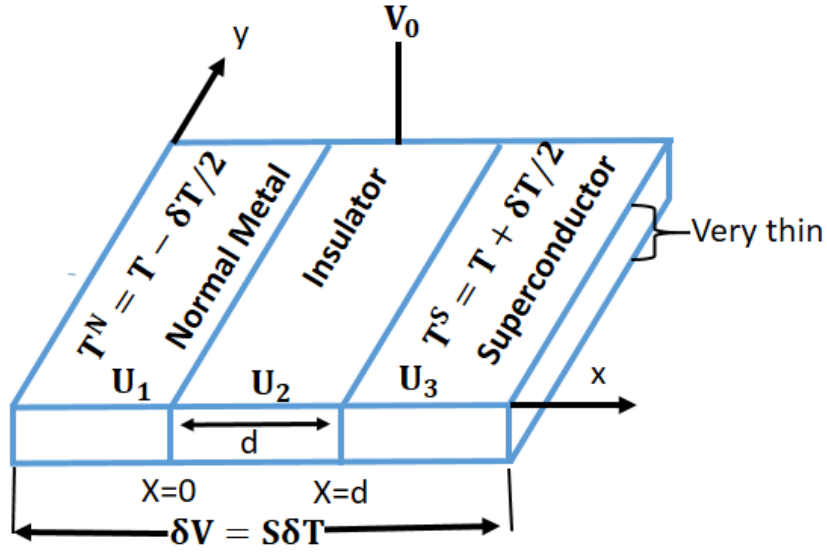


Figure 4.1: Schematic Diagram of the NIS junction setup as a thermopower device.

of the potential is described in Eqn.(3.3) in chapter 3. In the BTK approach, the electrons contributing to the current are only those whose velocities are directed towards the junction, that is, $v_x > 0$. The expression for the charge current through the NIS junction using BTK theory can be found to have the following form,

$$I_{NS}(E_F^N, T^N, E_F^S, T^S) = eA_r \sum_{\sigma} \int \int \tau_{\sigma}(E, \partial_{N1}) [f^N(E_f^N, T^N) - f^S(E_F^S, T^S)] N(E) v_x dE \cos \partial_{N1} d\partial_{N1} \quad 4.1$$

where $N(E)$ denotes the density of states, v_x is the velocity of electron, A_r is the area of contact, and f^N, f^S are the Fermi distribution functions for the metallic lead and the superconducting leads respectively. $\tau_{\sigma}(E, \partial_{N1})$ is the transfer probability. As the normal state resistance, R_N is defined by, $R_N = \frac{1}{2e^2 N_0 v_F^N A_r}$ (2 is the spin degeneracy factor, N_0 is the density of states at Fermi level, v_F^N is the Fermi velocity), the electrical charge current takes the following form,

$$I_{NS}(E_F^N, T^N, E_F^S, T^S) = \frac{1}{2eR_N N_0 v_F^N} \sum_{\sigma} \int \int \tau_{\sigma}(E, \partial_{N1}) [f^N(E_f^N, T^N) - f^S(E_F^S, T_S)] N(E) v_x dE \cos \partial_{N1} d\partial_{N1} \quad 4.2$$

where

$$\tau_{\sigma}(E, \partial_{N1}) = 1 - |b_{\sigma}(E, \partial_{N1})|^2 + \frac{\cos \partial_{N2}}{\cos \partial_{N1}} |a_{\sigma}(E, \partial_{N1})|^2 \quad 4.3$$

a_σ is amplitude of Andreev reflection, b_σ is amplitude of normal reflection and ∂_{N1} , ∂_{N2} are the reflection angles of electrons and holes in the normal region.

For a 2D free electron gas denoting parabolic energy dispersion, the density of states is constant and the velocity, $v_x \sim E^{1/2}$. Thus, we can write the current through the junction by the following form,

$$I_{NS}(E_F^N, T_N, E_F^S, T_S) = \frac{1}{2eR_N N_0 \sqrt{E_F^N}} \sum_\sigma \int \int \tau_\sigma(E, \partial_{N1}) [f^N(E_F^N, T^N) - f^S(E_F^S, T^S)] N_0 \sqrt{E} dE \cos \partial_{N1} d\partial_{N1} \quad 4.4$$

The flow of electrons can also transports thermal energy through the junction which is responsible for the thermal current. The thermal current is defined as the rate at which the thermal energy flows from the left lead to the right lead. The electronic charge current and the electronic thermal current being analogous, we are allowed to write the outbound energy flow rate from the normal lead to the superconducting lead as [17],

$$J_{NS} = \frac{1}{2e^2 R_N \sqrt{E_F^N}} \sum_\sigma \int \int (E - E_F^N) \tau'_\sigma(E, \partial_{N1}) [f^N(E_F^N, T^N) - f^S(E_F^S, T^S)] \sqrt{E} dE \cos \partial_{N1} d\partial_{N1} \quad 4.5$$

where τ'_σ is given by form [148],

$$\tau'_\sigma(E, \partial_{N1}) = 1 - |b_\sigma(E, \partial_{N1})|^2 - \frac{\cos \partial_{N2}}{\cos \partial_{N1}} |a_\sigma(E, \partial_{N1})|^2 \quad 4.6$$

It may be noted that the transfer probability of current and heat transport is different as the hole moving backwards contribute to the current but takes away energy. Similarly, the reverse, that is the rate at which the superconducting lead receives the thermal energy is written as,

$$J_{SN} = \frac{1}{2e^2 R_N \sqrt{E_F^N}} \sum_\sigma \int \int (E - E_F^S) \tau'_\sigma(E, \partial_{N1}) [f^N(E_F^N, T^N) - f^S(E_F^S, T^S)] \sqrt{E} dE \cos \partial_{N1} d\partial_{N1} \quad 4.7$$

Please note that the integral is over an angular aperture, ∂_{N1} and the energy, E .

4.1.1 Seebeck coefficient

A temperature difference between two dissimilar electrical conductors produces a voltage difference between the two substances. This phenomenon is known as Seebeck effect. Seebeck coefficient is a measurement of the amount

of potential induced in the device for unit temperature difference. It is thus a measure of the performance of thermocouples when a temperature gradient exists across it. Importantly, the magnitude and the sign of the Seebeck coefficient quantify the asymmetry of the electron distribution in the vicinity of the Fermi level. Metals usually have Seebeck coefficients which are of the order of the tens of $\mu\text{V}/\text{K}$, while for semiconductors, it is typically 2 to 3 magnitudes larger.

Since the metallic lead and the superconducting leads are subjected to a temperature difference, δT (shown in Fig.(4.1)), there will be a voltage difference, δV (say) between the two leads. The thermopower or the Seebeck coefficient, S is defined as the response of voltage to this temperature difference when zero electrical current passes through the junction. Hence we can write it as follows,

$$S = \left(\frac{\delta V}{\delta T} \right)_{I=0} \quad 4.8$$

Simply said, the Seebeck effect is a conversion of a thermal energy to electrical energy.

We consider the left and right electrodes serve as independent temperature reservoirs where the left electrode is fixed at a temperature, $T^N = T - \delta T/2$ and the right electrode is fixed at a temperature $T^S = T + \delta T/2$. The population of electrons in the left and the right leads are described by the Fermi-Dirac distribution function, f^N and f^S respectively where we assume that the Fermi energies satisfy $E_F^N = E_F^S$ at zero external bias.

Let us now consider an extra infinitesimal current is induced by an additional voltage, δV and the temperature difference, δT exists across the junction in an open circuit condition. The current induced by δT and δV are given by,

$$(dI)_T = I(E_F^N, T^N, E_F^S = E_F^N, T^S = T^N + \delta T) \quad 4.9$$

$$(dI)_V = I(E_F^N, T^N, E_F^S = E_F^N + e\delta V, T^S = T^N) \quad 4.10$$

Since that the current cannot flow in an open circuit, $(dI)_T$ counter balances $(dI)_V$ which allows us to write,

$$dI = (dI)_T + (dI)_V = 0 \quad 4.11$$

where the expression for the $(dI)_T$ and $(dI)_V$ can be obtained from Eqn.(4.4). With δT being small, we may expand the Fermi wave functions about a certain (absolute) temperature T in Taylor series, and retaining only the first order terms after shifting all energies by Fermi energies of the respective electrodes, we have

for the normal regime,

$$f^N(E - e\delta V, T - \delta T/2) = f_T(E) - e\delta V \frac{\partial f}{\partial E} - \frac{\delta T}{2} \frac{\partial f}{\partial T} = f_T(E) - e\delta V \frac{\partial f}{\partial E} + E \frac{\delta T}{2T} \frac{\partial f}{\partial E} \quad 4.12$$

and for the superconducting regime,

$$f^S(E, T + \delta T/2) = f_T(E) + \frac{\delta T}{2} \frac{\partial f}{\partial T} = f_T(E) - E \frac{\delta T}{2T} \frac{\partial f}{\partial E} \quad 4.13$$

The first order expansion of the Fermi-Dirac distribution function in $(dI)_T$ and $(dI)_V$ yields the following expression for the Seebeck coefficient, S ,

$$S = \frac{\delta V}{\delta T} = \frac{\sum_{\sigma} \int \int \tau_{\sigma}(E, \partial_{N1}) \frac{\partial f}{\partial E} E \sqrt{E + E_F^N} dE \cos \partial_{N1} d\partial_{N1}}{eT \sum_{\sigma} \int \int \tau_{\sigma}(E, \partial_{N1}) \frac{\partial f}{\partial E} \sqrt{E + E_F^N} dE \cos \partial_{N1} d\partial_{N1}} \quad 4.14$$

4.1.2 Figure of Merit

The efficiency of the device depends upon a quantity called as 'Figure of Merit' (FM). To get a clear idea of the efficiency, one should compute the FM, ZT which is given by,

$$Z_T = \frac{S^2 G}{K} T \quad 4.15$$

where S is Seebeck coefficient, G is the charge conductance, K is the thermal conductance of the carriers, and T is the absolute temperature. G can be calculated from the relation, $G = \frac{dI_{NS}}{dV}$ and is given by the following equation,

$$G = \frac{1}{2eR_N \sqrt{E_F^N}} \sum_{\sigma} \int \int \tau_{\sigma}(E, \partial_{N1}) \left[\frac{f^N(E_f^N, T^N)}{dV} - \frac{f^S(E_f^S, T_S)}{dV} \right] \sqrt{E} dE \cos \partial_{N1} d\partial_{N1} \quad 4.16$$

Again shifting all the energies by the Fermi energies, the above expression assumes the following form,

$$G = \frac{1}{2eR_N \sqrt{E_F^N}} \sum_{\sigma} \int \int \tau_{\sigma}(E, \partial_{N1}) \left(-\frac{\partial f}{\partial E} \right) \sqrt{E + E_F^N} dE \cos \partial_{N1} d\partial_{N1} \quad 4.17$$

The thermal conductance K , can be calculated from the relationship $K = \frac{dJ_{NS}}{dT}$ where J_{NS} is the thermal current flowing from the normal region to the superconducting region. The thermal current due to the carriers is the thermal energy carried by electrons while traveling between the electrodes driven by both dT and dV . Analogous to the extra current as in Eqn.(4.11), the extra electron's thermal

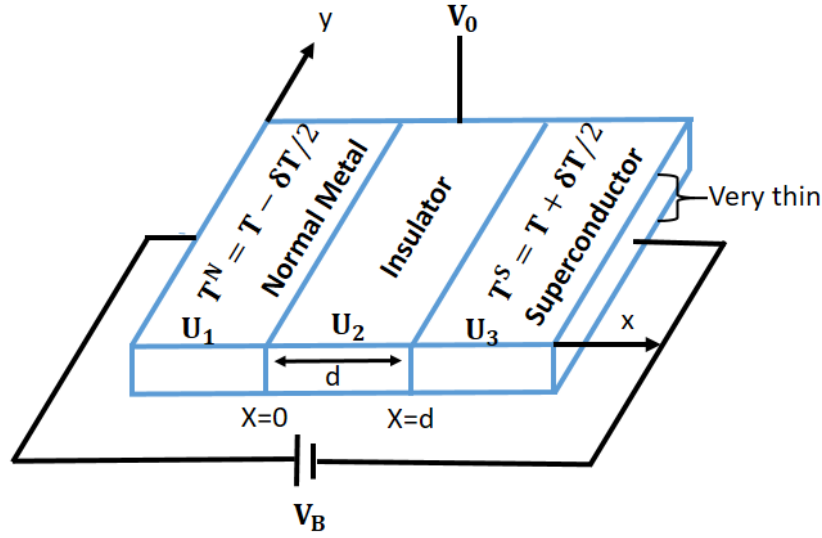


Figure 4.2: Schematic Diagram of the NIS junction setup as a cooling device. It may be noted that a bias voltage V_B is introduced for thermoelectric cooling.

current is given by,

$$dJ_{NS} = (dJ_{NS})_T + (dJ_{NS})_V \quad 4.18$$

where

$$\begin{aligned} (dJ_{NS})_T &= J_{NS}(E_F^N, T^N; E_F^S = E_F^N, T^S = T^N + \delta T) \\ (dJ_{NS})_V &= J_{NS}(E_F^N, T^N; E_F^S = E_F^N + e\delta V, T^S = T^N) \end{aligned} \quad 4.19$$

are the fractions of the thermal current driven by δT and δV , respectively. It can be noted that δV is generated by the Seebeck effect owing to the temperature difference that exists between the junctions. Both $(dJ_{NS})_T$ and $(dJ_{NS})_V$ can be calculated from Eqn.(4.22). The thermal conductance can be defined as $K = dJ_{NS}/dT$, which again derives contribution from two components, namely,

$$K = K^T + K^V \quad 4.20$$

where $K^T = (dJ_{NS})_T/dT$ and $K^V = (dJ_{NS})_V/dT$. We note that K^T and K^V denote thermal conductance owing to the temperature difference, δT and voltage difference, δV .

4.1.3 Thermoelectric cooling

As said earlier, the left electrode, that is the metallic lead serves as the cold reservoir and the right one (superconducting) serves as hot the reservoir. The junction device is connected to an external bias voltage, $V_B = (E_F^N - E_F^S)/e$, which

drives the carriers to flow from the metallic lead to the superconducting lead. Thus the electron removes the heat energy from the normal lead, subsequently transfers it to the superconducting lead which further makes the cold reservoir (metallic electrode) cooler. The energy conservation allows us to write,

$$J_{NS}(E_F^N, T^N; E_F^S, T^S) + I_{NS}(E_F^N, T^N; E_F^S, T^S)V_B = J_{SN}(E_F^N, T^N; E_F^S, T^S) \quad 4.21$$

As, in our calculations we have shifted energies by the Fermi energies of the respective electrodes, the final form of the thermal currents are given by,

$$J_{NS} = \frac{1}{2e^2 R_N \sqrt{E_F^N}} \sum_{\sigma} \int \int (E - eV_B) t'_{\sigma}(E, \partial_{N1}) [f(E - eV_B, T^N) - f(E, T^S)] \sqrt{E + E_F^N} dE \cos \partial_{N1} d\partial_{N1} \quad 4.22$$

and

$$J_{SN} = \frac{1}{2e^2 R_N \sqrt{E_F^N}} \sum_{\sigma} \int \int E t'_{\sigma}(E, \partial_{N1}) [f(E - eV_B, T^N) - f(E, T^S)] \sqrt{E + E_F^N} dE \cos \partial_{N1} d\partial_{N1} \quad 4.23$$

This normal-insulator-superconductor (NIS) junction can be regarded as the electronic cooling device only when $J_{NS} > 0$. This implies that it is capable of removing the heat from the cold reservoir, thereby making it cooler.

The performance of this junction as a self-cooling device can be measured by the coefficient of the performance (COP) where COP is defined as the ratio of the heat removed from the cold reservoir to the electrical power needed for driving the system. The COP for electronic thermal current, namely, COP is given by [17],

$$COP = \frac{J_{NS}}{I_{NS} V_B} = \frac{J_{NS}}{J_{NS} - J_{SN}} \quad 4.24$$

4.2 Results and discussions: Thermopower

For convenience, before getting ahead into the discussions of our results, again we would like to mention the values of the parameters used in our numerical computation. We have considered, $E_F^N = 150\Delta_0$. To see the effects of RSOC, we have defined a dimensionless quantity, $\hat{\eta}_R$ which is given by, $\hat{\eta}_R = U_1 k_F^N / E_F^N = U_2 k_F^I / E_F^I = U_3 k_F^S / E_F^S$. The value of the $\hat{\eta}_R$ is taken in range [0 : 2] in our numeric computation. The Rashba free case is included for comparison. The operating temperature range is set as such that, $T < T_c$ (T_c being the superconducting temperature). We have already mentioned that, to make a close connection with experiments, where disorder effects (although small in cleaner samples) cannot

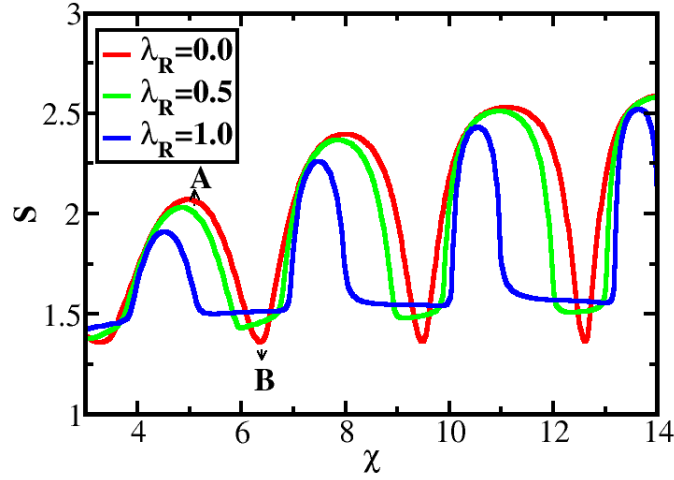


Figure 4.3: The variation of the Seebeck coefficient, S as function of effective barrier potential, χ . The oscillations are artifacts of electron interferences.

be skipped, finite quasiparticle lifetimes should be incorporated. In all our calculations we have invoked a Γ factor [138] that renormalizes the quasiparticle energies, E by $E \pm i\Gamma$. To remind ourselves, $\Gamma = \frac{1}{\tau_{QP}}$ where τ_{QP} is the finite quasiparticle lifetime. The value of Γ is taken as $0.1\Delta_0$.

In the following, we shall emphasize how a 'full control' on the thermoelectric response can be achieved by tuning the parameters of the NIS junction device, with the tunability of the Rashba coupling strength already being discussed. We define a dimensionless effective barrier potential, $\chi = k_F^I d$ where k_F^I and d are the Fermi wave vector and the width of the insulating region respectively. The Fermi wavevector of the insulating region is proportional to its barrier potential, V_0 via $E_F^I = E_F^N + V_0$. In the subsequent analysis we shall see that this effective barrier potential, $\chi \sim d \sqrt{V_0}$ (with $E_F^I \sim k_F^{I^2}$) is going to play a decisive role in the computation of the Seebeck coefficient, S . The parameters that are possible to tune experimentally belong to that of the insulating regime, namely the width, d and the barrier potential, V_0 .

In Fig.(4.3), the Seebeck coefficient, S is shown as a function of χ where the temperature, T is fixed at $T = 0.3\Delta_0$. S is a dimensionless quantity since $e = 1$, $k_B = 1$. We can see that the S (a measure of the thermopower) oscillates with a period of oscillation, η as the effective barrier potential is increased, where η has a certain value that depends on the barrier properties (see discussion below). In fact the oscillation frequency of the Seebeck coefficient depends only on the parameters pertaining to the insulating region of the NIS junction. The periodic behavior of the Seebeck coefficient as a function of χ is due to the electron interference phenomena that are reflected in the oscillatory terms in the definition of P_i^I s (see

Eqn.(2.40)). This oscillations are suggestive of obtaining a desired value of S for a certain value of the effective barrier potential, χ . To remind such variation is also obtained for the electrical conductance through a NIS junction.

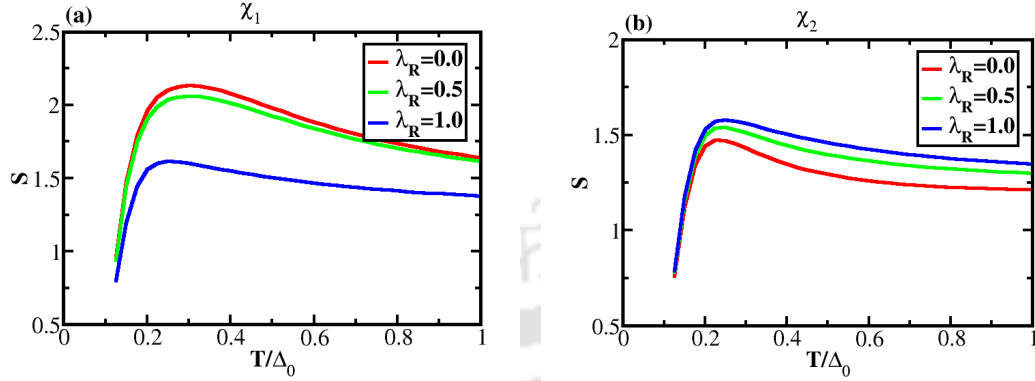


Figure 4.4: The variation of the Seebeck coefficient, S as a function of temperature scaled by superconducting gap, T/Δ_0 for two different values of χ , namely, (a) χ_1 , (b) χ_2 .

Moreover, the RSOC term which represents another tunable quantity in experiments, has interesting effects on the Seebeck profile. Fig.(4.3) reveals that the Seebeck coefficient, S is highly sensitive to the value of the RSOC, though the oscillations occur irrespective of the strength of the Rashba coupling. The Rashba term modulates the interference pattern in an interesting way. With the inclusion of RSOC there is shift in the maxima (peak) positions whereas the minima are replaced by valley type features. Further with the increasing strength of RSOC, the peak values of the Seebeck coefficient decreases, whereas the minima shows increased values. From Fig.(4.3) it is clear that the peak value of the Seebeck coefficient increases with χ for all values of the RSOC strength. The reason behind these features can be explained from Eqn.(2.40). We know that the Seebeck coefficient is the function of AR and NR amplitudes and these amplitudes are functions of the P_i 's (see Eqn.(2.40)). Remember that, the P_i functions are complex numbers which have phases (exponential term) along with amplitudes. Now, with the inclusion of RSOC both the components of P_i (amplitude and phase) will be changed because the momenta appearing in all χ_i 's (product of momenta and angles related to incidence, reflection and transmission of electrons (see Eqn.(2.40))) get modified in presence of RSOC. As a result with the inclusion of RSOC the peak positions shift and the corresponding peak value changes.

The interesting fact lies in the modulation of oscillation patterns in presence of RSOC in such a way that in certain ranges of the effective barrier potential, RSOC enhances and for other ranges it diminishes the Seebeck coefficient. This implies that, tuning of the RSOC parameter and the effective barrier potential provides an opportunity for achieving a desired value of thermopower. This should have

implications in experiments in the following sense. A certain application may demand a certain amount of thermopower. An NIS junction with a tunable Rashba coupling at the interfaces along with an adjustable insulating barrier may be able to deliver that.

Now we show the Seebeck coefficient as a function of temperature, T , (in units of the superconducting gap, that is, T/Δ_0) for different values of RSOC for two different regions of the effective barrier potential, namely, χ_1 and χ_2 in Fig.(4.4). χ_1 denotes the values of effective barrier potential where the peaks of the RSOC free Seebeck coefficient take places and χ_2 denotes the same where the minima of the Seebeck coefficient (RSOC free) occur. These two values of the effective barrier potential play a vital role in subsequent discussions of this chapter. Specifically we focus on the region A ($\chi = \chi_1$) and region B ($\chi = \chi_2$) (shown in Fig.(4.3)). These values of χ show contrasting characteristics, that is, S decreases with RSOC for the effective barrier potential to have a value $\chi = \chi_1$ and increases for the other case, that is, $\chi = \chi_2$. Thus it is apparent that the magnitude of the effective barrier potential reserves the right to decide whether RSOC will enhance or decrease the magnitude of the thermopower of our NIS junction.

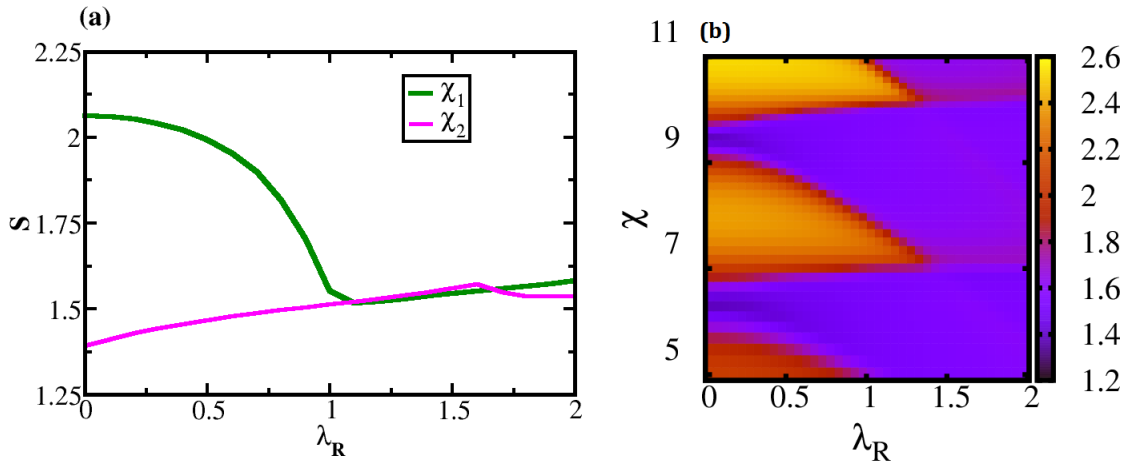


Figure 4.5: (a) The variation of the Seebeck coefficient, S as function of λ_R . (b) The variation of S as function of both λ_R and χ .

Finally we consider the variation of the Seebeck coefficient, S as a function of Rashba strength, λ_R for two different values of χ in Fig.(4.5a) which, as earlier, correspond to χ_1 and χ_2 (where contrasting behaviour is seen). The features reveal that S at χ_1 decreases with a hump before becoming (almost) constant eventually. This corresponds to the peak value of the Seebeck coefficient which overall shows a decreasing trend as the RSOC is enhanced. This situation is strikingly different for $\chi = \chi_2$ as shown in Fig.(4.5a). It shows S at χ_2 has an increasing behaviour with the strength of the Rashba coupling, though the enhancement is small.

Further we have presented a color map which shows the variation of the Seebeck coefficient as the function of both \hat{n}_R and χ in Fig.(4.5b). As earlier, in this Figure also, the above discussion is reflected. This re-emphasizes that the Seebeck coefficient has an interesting trend with the variation of the Rashba strength and has been addressed by us in details.

4.2.1 Figure of Merit

Here we show results of the performance of the NIS junction as a thermopower device. Fig.(4.6) shows the Figure of Merit as a function of barrier potential for different values of the strength of Rashba coupling, the temperature being fixed at $T = 0.3\Delta_0$. A measure of the performance and the efficiency of the NIS junction as a thermopower device is defined by the Figure of Merit (ZT) (see Eq. (4.15)). As earlier, the oscillations are obtained in ZT and the inclusion of RSOC shows

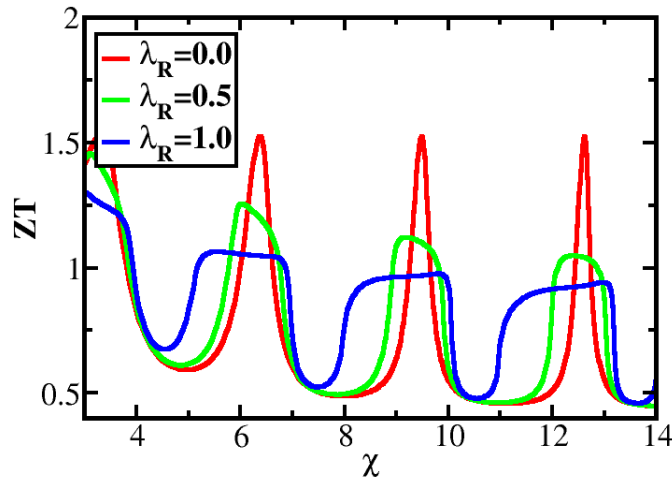


Figure 4.6: The variation of the Figure of Merit (ZT) as a function of effective barrier potential, χ for different strengths of RSOC, \hat{n}_R .

an interesting effect on the interference pattern. Fig.(4.6) reveals that the Figure of Merit, ZT is highly sensitive to the strength of RSOC term though the oscillations persist irrespective of the magnitude of RSOC parameter. The Rashba term modulates the interference pattern in the following way. Same as the earlier case, there are shifts in minima (dip) and maxima (peak) positions as RSOC is included. The reason behind such features can be explained from the expressions of P'_i s (Eqn.(2.40) which we have explained earlier. Further it can be observed that FM is out of phase with S (see Fig.(4.3) and Fig.(4.6)). So when the effective barrier potential, χ has a value $\chi = \chi_1$, S has maximum, while the FM has minimum. For $\chi = \chi_2$, the reverse happens. Next we show the Figure of Merit as a

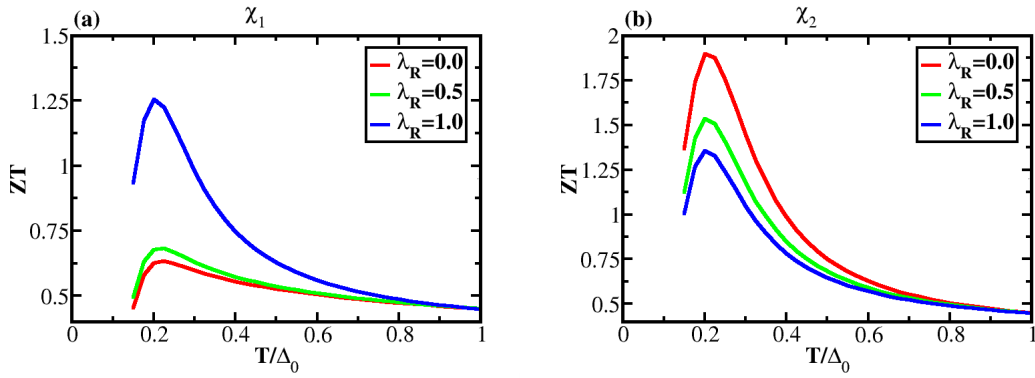


Figure 4.7: The variation of the Figure of Merit (ZT) as a function of temperature, T/Δ_0 for two different regions of the effective barrier potential, χ , namely, (a) χ_1 . (b) χ_2 .

function of temperature, T , (in the units of superconducting gap, that is, T/Δ_0) for different values of the RSOC strengths for two different regions of the effective barrier potential, namely, χ_1 and χ_2 in Fig.(4.7). We observe that, with temperature, the efficiency of the system as a thermopower device has a non-monotonic dependence, that is, it initially increases at lower temperatures ($T \ll \Delta_0$), and reaches a peak value at a certain $T \sim 0.25\Delta_0$, beyond which it decreases. These two values of χ show contrasting characteristics, that is, ZT increases with RSOC for the effective barrier potential $\chi = \chi_1$ and decreases for the other case, that is, $\chi = \chi_2$. These results are just the opposite compared to the behaviour of the thermopower, S obtained earlier. However as before the value of RSOC influences ZT for an NIS junction.

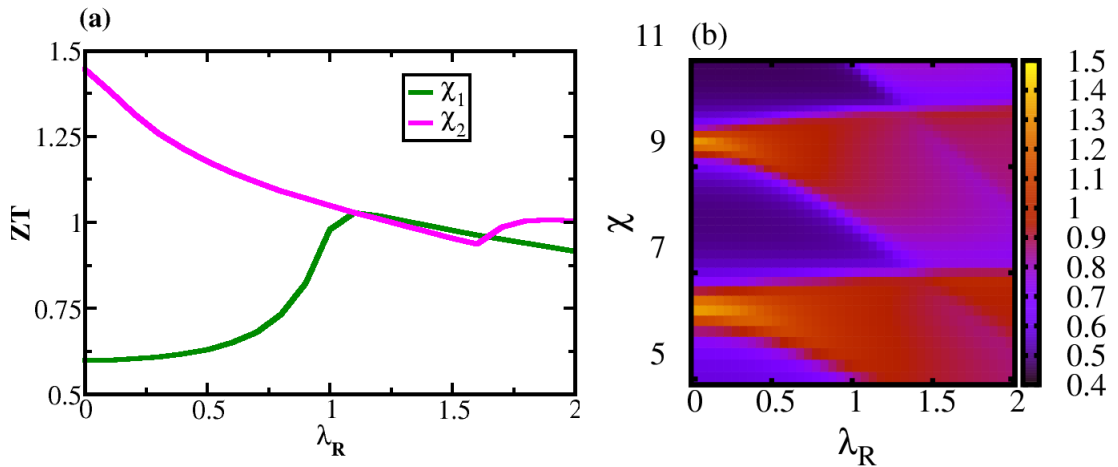


Figure 4.8: (a) The variation of ZT as a function of λ_R , (b) The variation of ZT as function of both λ_R and χ .

Finally, to complete our enumeration of the tunability of an NIS junction, the Figure of Merit is plotted as a function of the Rashba coupling strength, $\hat{\lambda}_R$ for two different values of χ (that is, χ_1 and χ_2) in Fig.(4.8a). Fig.(4.8a) reveals that when the effective barrier potential corresponds to $\chi = \chi_1$, the Figure of Merit, increases upto a certain value of the RSOC parameter and then decreases. But for $\chi = \chi_2$, the reverse happens. Further the variation of the Figure of merit as the function of both Rashba spin-orbit coupling and χ are presented in Fig.(4.8b). These results comprehensively underscore the asymmetry of the maxima (peak) and minima (dip) of ZT owing to modification in the amplitude and the phase of oscillations caused by the inclusion of the Rashba term.

4.3 Results and discussions: Thermoelectric cooling

Here we study a tunable thermoelectric cooling device based on the Rashba coupled NIS junction. The main advantage of this study is that it provides the possibility for fabricating the nano-scale refrigerators, where owing to the size reduction in the physical dimension of the device, the Joule heating and the photon radiation can be minimized.

We remind ourselves that when an external biasing voltage V_B is applied across the junction, electrons flow from the left electrode (metal) to the right electrode (superconductor) which carry not only the charge current, but also the thermal current. It can be noted that the phenomenon of the thermoelectric refrigeration requires an electrical power of magnitude $I_{NS} V_B$ to remove heat from the left electrode, both I_{NS} and V_B being the charge current and the bias voltage respectively. The nano-refrigeration works only for the range of the driving voltage corresponding to $J_{NS} > 0$.

To get an idea about the role of effective barrier potential on the thermal current, we present the variation of a dimensionless quantity, $2J_{NS}e^2R_N/\Delta_0^2$ as a function of χ (a tunable quantity in our system) in Fig.(4.9). The driving voltage is fixed at $V_B = 0.5\Delta_0$, where the refrigeration works. The temperature difference between the two electrodes is fixed at $\delta T = 0.02\Delta_0$ ensuring that δT is really small and temperature is fixed at $T = 0.5\Delta_0$. As expected, similar to the charge current and the Seebeck coefficient, it shows Fabry Perot like oscillations as the effective barrier potential is varied [119, 143, 149] and hence highlights the interference properties of the carriers. The sharpness of the peaks in the Rashba free case suggests that the barrier potential has to be precisely chosen for achieving the maximum thermal current and hence thermoelectric cooling. A slight detuning of the effective barrier potential will cause a fall in the value of thermal current.

These modulations are suggestive of obtaining a desired value of thermal current and hence a thermoelectric cooling.

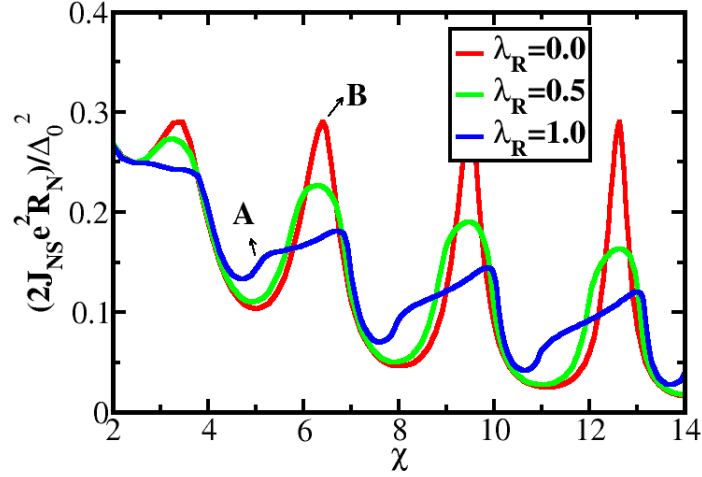


Figure 4.9: The variation of the thermal current (J_{NS}), rendered dimensionless by $2J_{NS}e^2R_N/\Delta_0^2$ as a function of the effective barrier potential, χ .

Fig.(4.9) reveals that the thermal current is very sensitive to the other tunable quantity of our work, namely the Rashba coupling. It has an interesting effect on the interference pattern of the thermal current. Same as earlier, there is a shift of the maxima and the minima positions, accompanied by the modification of their values. The reasons have already been discussed. Further in presence of RSOC, the peak values decrease with increasing strengths of the effective barrier potential. An additional observation is the interplay of the effective barrier potential and the RSOC to assume decisive roles in determining the magnitude of the thermal current in the following sense. For certain ranges of the effective barrier potential, the RSOC enhances the thermal current, while for other certain ranges the reverse happens. With the inclusion of RSOC, the modifications in the oscillation pattern are such that, in some region the thermal current is enhanced by the Rashba term and in some other region it diminishes the thermal current. The involvement of the barrier potential and the RSOC parameter in shaping up the current characteristics should have important implications for the experiments. An NIS junction with a tunable Rashba coupling along with an insulating barrier provides a good possibility to attain controlled refrigeration.

Next we show the variation of the thermal current as the function of the biasing voltage for the effective barrier potential, χ to assume values χ_1 (corresponding to peak positions of the Seebeck coefficient) and χ_2 (for the corresponding minima) in Fig.(4.10). It is clear that for zero bias, the rate of the thermal energy extracted from the cold reservoir is negative. To achieve a cooling effect, a lower threshold

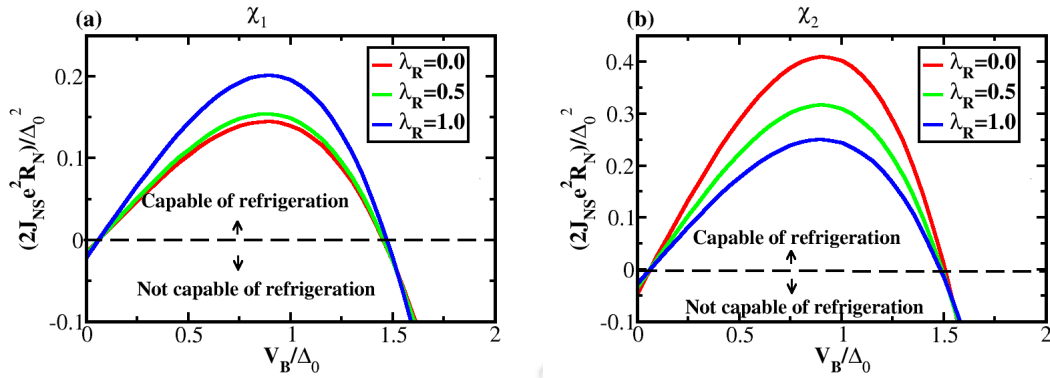


Figure 4.10: The variation of $2J_{NS}e^2R_N/\Delta_0^2$ as function of driving voltage, V_B (scaled by the superconducting order parameter, Δ_0) for two different values of χ , namely, (a) χ_1 , (b) χ_2 . The upper and lower critical values of the biasing voltage where refrigeration works are shown.

voltage of the battery, namely, V_{lower} is required. Thus, when $V_B < V_{lower}$, the refrigeration phenomenon will fail. Also an upper threshold voltage, V_{upper} is also present beyond which the refrigeration effect ceases to exist. Moreover, the lower and the upper thresholds do not depend on the RSOC parameter and the effective barrier potential as evident from all the plots becoming non-zero at same values of V_{lower} and V_{upper} , namely, $V_{lower} \sim 0.06\Delta_0$ and $V_{upper} \sim 1.5\Delta_0$. For a narrow range of the driving voltage (having values in the vicinity of the magnitude of the superconducting order parameter), the cooling process is efficient. The maximum refrigeration occurs at around, $V_B \sim 0.9\Delta_0$. Further it is clear from Fig.(4.10a) and Fig.(4.10b), cooling phenomena show different trends with RSOC with regard to $\chi = \chi_1$ and $\chi = \chi_2$.

Let us take an example for illustration of the cooling effects. Consider the $\hat{\eta}_R = 1$ case which shows maximum cooling effects for an effective barrier potential, χ to have a value χ_1 (see Fig.(4.10a)). For the driving voltage, V_B fixed at $0.9\Delta_0$ and $\Delta_0 \sim 0.002eV$ (a realistic value), one achieves a cooling of the metal by approximately 7.3K (see footnote ¹), whereas corresponding to the Rashba free case ($\hat{\eta}_R = 0$) ($J_{NS} \sim 0.075$ in units of Δ_0^2/e^2R_N), one obtains a cooling by approximately 6.1K. Thus the Rashba coupling augments the cooling effects. On the contrary for an effective barrier potential such that $\chi = \chi_2$ (Fig.(4.10b)), one obtains a cooling by $\sim 10.3K$ for the Rashba free case, while for $\hat{\eta}_R = 1$ the metallic lead is cooled down by approximately 7.3K. In the latter case, the Rashba term hinders cooling effects. It may be noted that in either of the cases, assuming the Rashba coupling to assume values in the range of $[0 : 1]$, the cooling effects obtained by us are measurable.

¹Corresponding to $V_B = 0.9\Delta_0$, J_{NS} is 0.1 in units of Δ_0^2/e^2R_N . Multiplying 0.1 by Δ_0^2 (with $\Delta_0 = 0.002eV$) and using $1K = 8.62 \times 10^{-5}eV$ one gets 7.3K.

The variation of the thermal current as the function of RSOC parameter for two different values of effective barrier potential have been presented in Fig.(4.11a) where the driving voltage V_B is fixed at $0.5\Delta_0$. As earlier, we have considered these

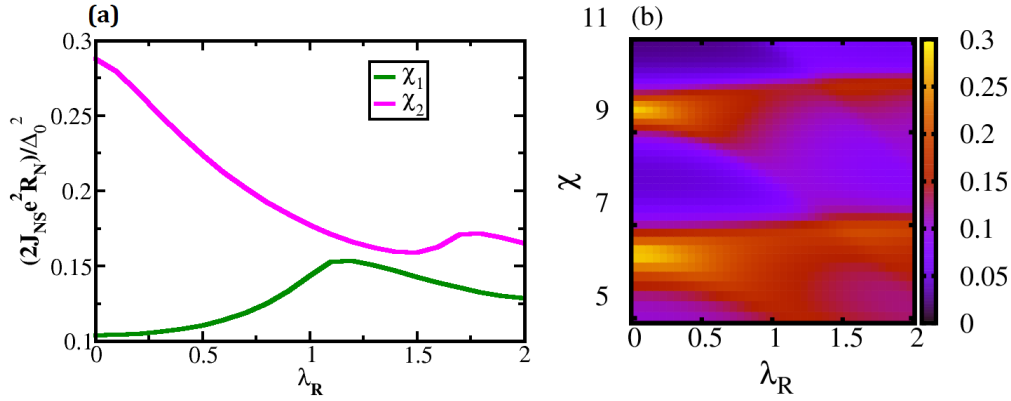


Figure 4.11: (a) The variation of $2J_{NS}e^2R_N/\Delta_0^2$ as function of RSOC strength, $\hat{\lambda}_R$. (b) The variation of $2J_{NS}e^2R_N/\Delta_0^2$ as function of both $\hat{\lambda}_R$ and χ .

values of χ (namely, χ_1 and χ_2) to show the contrasting nature of the behavior of the thermal current in presence of RSOC. It is clear that up to a certain value of RSOC, it enhances the thermal current for the effective barrier potential to have value equal to χ_1 and for it to have a value χ_2 , up to a certain strength of the RSOC parameter, the reverse happens. For large values of the RSOC strength, both the plots show a decreasing trend. Finally we have shown the variation of the thermal current as the function of both RSOC and χ in Fig.(4.11b). Although tunable, RSOC rarely becomes very large, and thus the lower to moderate values of RSOC parameter is of experimental importance. Even though we have varied the Rashba term over a broad range, we observe interesting physics to be occurring in low RSOC regime also.

4.3.1 Coefficient of Performance (COP)

Here we show results for the performance of the NIS junction as a self-cooling device. To recapitulate, a measure of the performance and the efficiency of the NIS junction as a thermoelectric nano-refrigerator is defined by the coefficient of performance (COP) (see Eq. (4.24)). Fig.(4.12) shows COP as the function of the effective barrier potential (χ) for different values of RSOC, where biasing voltage being fixed at $V_B = 0.15\Delta_0$. The inclusion of RSOC has an interesting effect on the interference pattern. Similar conclusions as earlier can be drawn on the interplay of RSOC and the barrier potential in the determining of the behavior of COP. Thus to obtain a desired value of COP, one can play with the value of χ ($= k_F^1 d$ which can be controlled by external means as emphasized in our work). This

should have enormous experimental relevance. Comparison between Fig.(4.9a) and Fig.(4.12a) reveals that the cooling effect and the performance of the cooling effect have contrasting behaviour as a function of effective barrier potential. This implies that for maximum cooling, the COP is minimum and vice versa. This result makes sense as more external power is needed to remove heat from the cold reservoir, thereby implying that maximum cooling corresponds to minimum COP .

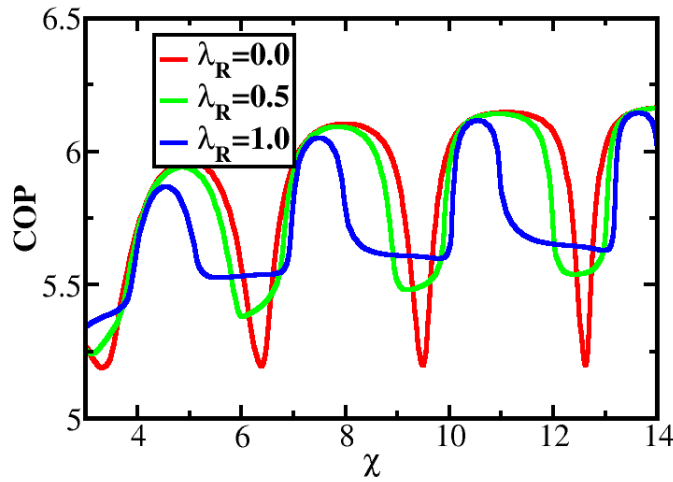


Figure 4.12: The variation of COP as function of χ for different strength of RSOC.

In Fig.(4.13) we present the variation of COP as a function of the biasing voltage for two different values of the effective barrier potential, χ (namely, some χ_1 and χ_2). Fig.(4.13) reveals that only at very low biasing voltage the COP depends on the

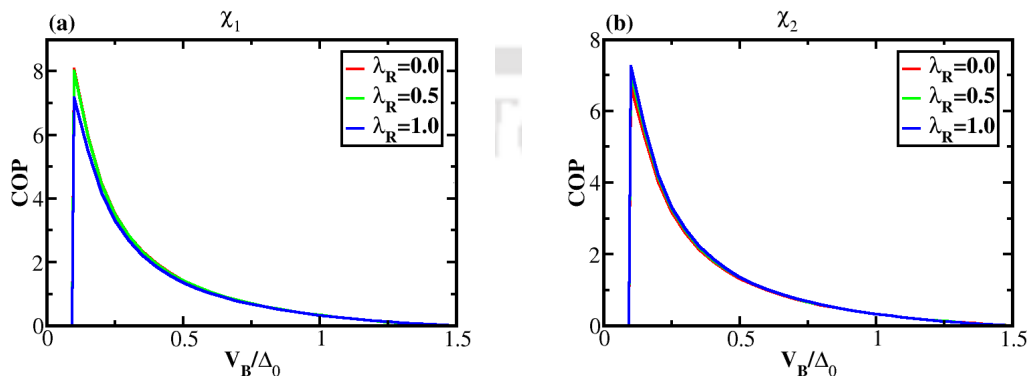


Figure 4.13: The variation of COP as function of biasing voltage, V_B (scaled by the superconducting order parameter, Δ_0) for two different χ values (namely (a) χ_1 and (b) χ_2).

RSOC parameter, where the maxima of COP take occur. Further it also shows that

for a narrow range of the biasing voltage the nano refrigeration works. It is clear that when the driving voltage exceeds the value $1.5\Delta_0$, the refrigeration vanishes irrespective of the RSOC strength and the effective barrier potential. Hence fixing the parameters to suitable values will yield a desired efficiency.

Finally to complete our enumeration of the tunability of the NIS junction with regard to its refrigeration properties, the COP as a function of the RSOC parameter, for a value of the biasing voltage where the maxima occur, is shown in Fig.(4.14a). The COP as a function of the RSOC parameter shows a different

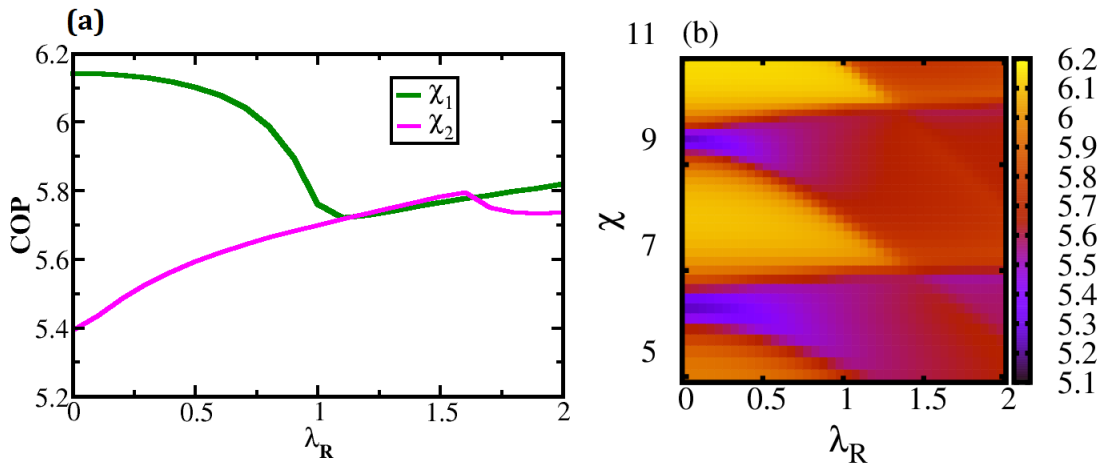


Figure 4.14: (a) The variation of COP as function of λ_R , (b) The variation of COP as function of both λ_R and χ .

nature for two different values of effective barrier potential, namely, χ_1 and χ_2 . Finally the variation of the COP as the function of both RSOC and χ is shown in Fig.(4.14b). It re-emphasizes the different nature of COP as the function of RSOC for different regions of effective barrier potential. The preceding discussion makes it amply clear that λ_R and χ which are assumably under control in an experimental setup, have critical roles to play in the phenomenon of nano refrigeration.

4.4 Concluding remarks

We have investigated the thermoelectric properties of a spin orbit coupled device consisting of a normal-insulator-superconductor junction where the insulating layer is characterized by the barrier width, d and the barrier potential, V_0 . The key results are highlighted as follows. We find an oscillatory feature for the thermopower as a function of the effective barrier potential. These results show interesting interplay with Rashba coupling, in the sense that the thermopower increases with RSOC for certain ranges of this potential, while for others the reverse happens. Beside these, we have investigated the efficiency of the system as a thermopower device. Further, we have studied the nano-refrigeration properties

of this junction. The working condition for the refrigeration is $J_{NS} > 0$ and it is restricted by a narrow range of the biasing voltage, that is, for values lower and higher than that specified in the preceding section, the refrigeration phenomenon does not work. An oscillatory nature for both the thermal current and the coefficient of performance as a thermoelectric cooling device has been obtained as a function of the effective barrier potential. The interplay of the RSOC strength and the effective barrier potential is crucial to determine the magnitude of the thermal current that is removed from the normal metal and its performance as a cooling device. Since the strength of RSOC and the effective barrier potential can be tuned externally, our studies on the thermoelectric properties can be an important input to experimental studies which aim to provide the desired thermoelectric properties of an NIS junction device.



Chapter 5: Charge transport through graphene based NS junction

One of the most explored topics in the field of condensed matter physics is the study of the graphene [35, 150, 151] which is a two dimensional single layer of hexagonal lattice of carbon atoms. The conduction and the valance bands in graphene touch each other along the six Dirac points where the quasiparticle excitations show a linear Dirac-like energy dispersion. The unique geometrical structure of graphene has generated tremendous interest in different field of applications, such as, electronics [49, 150, 151], opto-electronics [152, 153], and spintronics [154–157]. Further, some other interesting phenomena such as, anomalous quantum Hall effect [50], chiral tunneling [58, 158], Klein paradox [58, 159] have been obtained in graphene. Moreover, the superconducting features can be induced in graphene by possible intercalation with dopant molecules [79] or via proximity effects [80,81]. Such prospects provide a newer scopes of fabricating devices based on hybrid structures of graphene based superconductors. It has been predicted that [160], due to the Dirac-like energy spectrum of its quasiparticles, a graphene normal-superconductor (NS) junction can exhibit specular-Andreev reflection in contrast to the usual retroreflection observed in conventional NS junctions. This leads to qualitatively different tunneling conductance features compared to the conventional NS junctions [38].

With the progress of spintronics in the recent past, the capability of controlling the spin degree of freedom in guided transport with unprecedented accuracy has gained significance. The phenomenon of spin-orbit coupling (SOC) is key to success of this rising field. In low dimensions, usually, in case of two dimensional electron gases (2DEG), where the surface inversion symmetry is violated, a special type of spin-orbit coupling, namely the Rashba spin-orbit coupling (RSOC) [39] becomes important and hence cannot be skipped in the context of charge transport. As we have seen in the preceding chapters, the Rashba coupling was an important ingredient to the quantum transport in junction devices, it will continue to be prominent in our ongoing discussion on graphene as well.

The tunability of the RSOC strength via an external gate voltage [42] provides an additional impetus. In particular, there are feasible techniques to strengthen the SOC strengths in graphene, such as via adatoms [87], by functionalization with methyl groups [89], using proximity effect of a three dimensional topological insulators [88, 142] etc. Recently it is observed that the strength of the RSOC can be increased up to 100meV via Au intercalation at the graphene-Ni interface [90]. Further a large Rashba splitting about 225 meV in epitaxial graphene layers on the surface of Ni [91] and a giant RSOC at the graphene-Ir surface from Pb

intercalation have been observed [161]. Further in Ref. [44] it is shown that how a double gated structure and a solid electrolyte surrounding the gates can be used to obtain enhanced RSOC strengths. In particular, the electrolyte gating enables 6-fold tuning of Rashba coefficient.

There could be another type of SOC that can be realized in graphene, namely, the intrinsic SOC (ISOC). Kane and Mele predicted that the presence of both the spin-orbit couplings may be responsible for a new topological state, namely, the quantum spin Hall (QSH) state. But due to very small SOC strengths (typically $0.01 - 0.05 meV$) [85], the QSH phase has eluded experimental confirmation. Nevertheless, it is suggested that the adsorption of adatoms such as, Indium (In), Thallium (Tl) [87] and Osmium (Os) [134] can enhance the intrinsic SOC significantly. Motivated by the above, we have executed an extensive study of the conductance characteristics of a Kane-Mele normal-superconductor nano-junction (same as an adatom decorated graphene NS junction) in the presence of both kind of SOCs by employing the BTK formalism. We have computed spin resolved charge transport and explored how the spin-orbit couplings (induced by adatoms) assume roles in shaping up the conductance characteristics of such a Kane-Mele junction. In particular, we ask whether one 'helps' or 'hinders' the other in the low energy transport phenomenon which is mostly of interest in this context.

The chapter is organized as follows. In Section (5.1.1) we present results for the conductance characteristics of a Kane-Mele NS junction and corresponding discussions. The results on the Kane-Mele junction with an insulating barrier in between, that is the NIS junction are presented in Section (5.2.1). In Section (5.3) we summarize our results and highlight our findings.

5.1 Graphene based NS junction

We consider an NS junction in a graphene sheet placed along the XY plane, where the left electrode of the sheet is a normal ($x \leq 0$) and the right one ($x \geq 0$) is of a superconducting material. The $x \geq 0$ region is considered to have been produced by proximity effect by an external superconductor. For simplicity, only the conventional s -wave pairing symmetry has been considered here.

The effective Hamiltonian for graphene including the SOCs is written as,

$$\begin{aligned}
 H = & -t_1 \sum_{\langle ij \rangle} a_i^\dagger b_j + i\hat{\eta}_I \sum_{\langle\langle ij \rangle\rangle} V_{ij} (a_i^\dagger \sigma_z a_j \\
 & + b_i^\dagger \sigma_z b_j) + i\hat{\eta}_R \sum_{\langle ij \rangle} a_i^\dagger (\vec{\sigma} \times \hat{d}_{ij}) \cdot \hat{n} b_j + \hat{\eta}_v \sum_i a_i^\dagger a_i \\
 & - \hat{\eta}_v \sum_i b_i^\dagger b_i + h.c.
 \end{aligned}
 \tag{5.1}$$

The first term is the nearest neighbour (NN) hopping term, with a hopping strength t_1 , the second term is an intrinsic spin-orbit coupling term given by the next-nearest neighbours (NNN) hopping, where $\hat{\eta}_l$ is the strength of the intrinsic spin-orbit coupling. $\langle\langle ij \rangle\rangle$ denotes the summation over NNN sites, along with $V_{ij} = +(-)$ if the hopping is clock(anti clock) wise. The third term is the nearest neighbour Rashba term, where \hat{d}_{ij} is the unit vector connecting NN sites i and j , $\vec{\sigma}$ is the vector of Pauli matrices and $\hat{n} = \hat{x}$ is unit vector along the interface normal. The latter is an assumption as \hat{x} lies perpendicular to the interface. $\hat{\eta}_v$ is an on-site energy which is different on the two sites within the cell. This is called as the staggered term which creates the sublattice asymmetry. In particular we have considered ” $+\hat{\eta}_v$ ” energy at site A and ” $-\hat{\eta}_v$ ” energy at site B. Operators a_i^\dagger (b_i^\dagger) create and a_i (b_i) annihilate an electron at R_i sites of the A(B) sublattice. Elaborate discussions on the Kane-Mele Hamiltonian are included in Chapter 2.

The Fermi energy variation across the junction system is,

$$E_F(x) = E_F^N \Theta(-x) + E_F^S \Theta(x) \quad \text{5.2}$$

where E_F^N and E_F^S are the Fermi energies of the normal and the superconducting leads. E_F^S is defined by, $E_F^S = E_F^N + V_0$, where V_0 has been used for characterizing the Fermi surface mismatch.

It is important to note that though in the presence of the RSOC and ISOC, there are opening of gaps in the electronic dispersion (insulating regime) at the valley points (K and K'), the incident particles will still be able to pass through the insulating gap under certain conditions. These condition can be given as the following. If the condition (i) $B_i^2 > 4A_i C_i$ (see Eqn.(2.57)) is violated then the values of the intrinsic and the Rashba coupling terms should follow the condition (ii) $(\hat{\eta}'_{lv}{}^2 + \hat{\eta}'_{R}{}^2) < (E_N^F \pm E)^2$, such that the transmission is possible. The terms $\hat{\eta}'_{lv}$ and $\hat{\eta}'_R$ are given by, $\hat{\eta}'_{lv} = \hat{\eta}_v - \sigma 3\sqrt{3}\hat{\eta}_l$ and $\hat{\eta}'_R = 3\hat{\eta}_R/2$ (see Eqn.(2.56) and Eqn.(2.57)) respectively. If these conditions are violated then there will not any transmission. In a sense these conditions may be contemplated to distinguish the topological insulators from that of the ordinary insulators. The inset of Fig.(1) of Ref. [83] may be seen where a diamond shaped region in the $\hat{\eta}_R$ (in units of $\hat{\eta}_l$) vs. $\hat{\eta}_v$ (scaled by $\hat{\eta}_l$) is identified as the topological phase where the conduction is possible only via the edge states, while the bulk remains insulating. For our computation of transport using the BTK formalism, the above inequality yields a condition for transmission, which, when violated ensures no conductance.

5.1.1 Results and Discussions on Kane-Mele NS junction

We have investigated the tunneling conductance of a graphene based normal and superconductor junction device in the presence of Rashba and the intrinsic

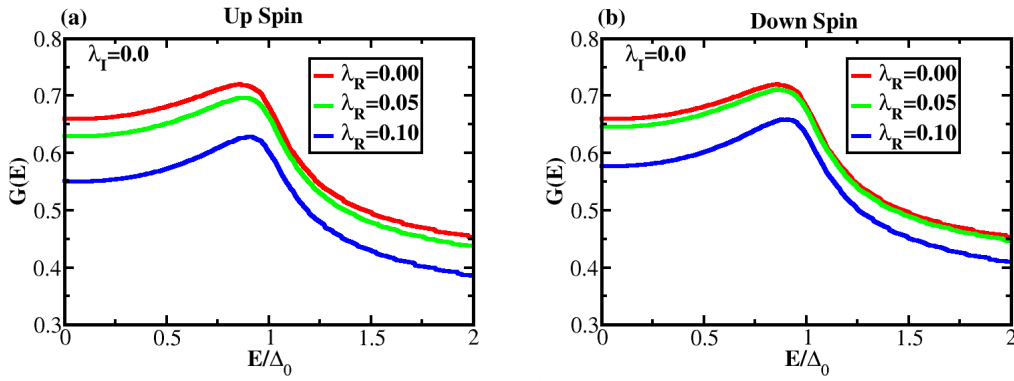


Figure 5.1: (a) The variation of conductance for the up spin, G_{up} as a function of biasing voltage (scaled by the superconducting order parameter), E/Δ_0 , (b) The variation of conductance for the down spin, G_{down} as the function of E/Δ_0 .

sic spin-orbit couplings possibly induced by transition metal adatoms (or other means). This mimics a Kane-Mele nano-junction which includes the effects of the spin-orbit couplings in a pristine graphene. These metal adatoms are adsorbed by the graphene nanoribbon and they are capable of enhancing the strengths of the spin-orbit couplings owing to the following reason. The electrons from the outer orbitals of the adatoms are distributed among the surrounding Carbon atoms of the graphene nanoribbon leaving behind a net positive charge. To screen this positive charge, the electrons conglomerate in the vicinity of an adatom. This electron cloud results in an inhomogeneous electric field which is possibly responsible for an enhanced (Rashba) spin-orbit coupling. In our work, the strengths of the spin-orbit couplings, namely $\hat{\lambda}_R$ and $\hat{\lambda}_I$ are taken as parameters and the transport properties are computed for different choices of these parameters (see discussion below). As emphasized, physically this entails decorating the graphene nanoribbon with different adatoms that are capable of including spin-orbit couplings of larger magnitude.

For the numerical calculation of the conductance, we have employed the results obtained in Chapter 2 via BTK formalism. Before going ahead into the discussion of the results, we include a note on the values of various parameters used in the computation of the conductance. To put things in perspective, we have considered reasonable values of the parameters. The Fermi energy has been taken as $50\Delta_0$ ($\sim 500meV$). The potential V_0 , used for Fermi energy mismatch, has been taken as $5E_F^N$. From these values of the Fermi energies, we have calculated the Fermi velocity and subsequently, the hopping parameter, t_1 . The strengths of the nearest neighbour hopping, that is, $\hat{\lambda}_R$ and the next nearest hopping, $\hat{\lambda}_I$ have been considered in units of t_1 . The value of $\hat{\lambda}_R$ and $\hat{\lambda}_I$ are varied in the range $[0 : 0.1t_1]$ ($0.1t_1 \sim 0.2 - 0.3eV$) and $[0 : 0.03t_1]$ ($0.03t_1 \sim 0.1eV$) respectively. In Ref. [91] it is shown that a large Rashba splitting about $225meV$ in epitaxial

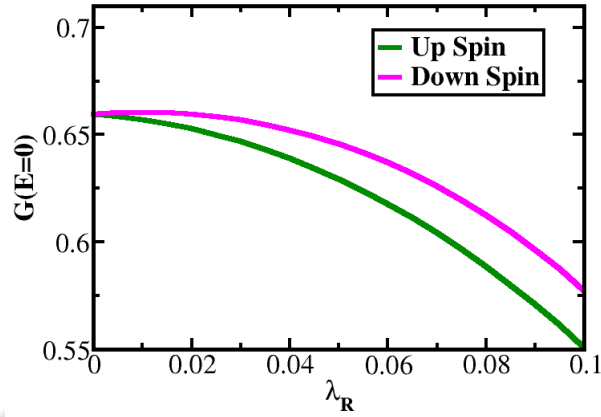


Figure 5.2: The variation of the spin resolved conductance, as a function of RSOC strength, when ISOC term is kept at zero ($\hat{\eta}_I = 0$).

graphene layers on the surface of Ni yields $\hat{\eta}_R \sim 0.1 t_1$. Further, it is proposed that the adsorption of adatoms, such as, Indium (In), Thallium (Tl) [87] and Osmium (Os) [134] can enhance the intrinsic SOC significantly. For example, $\hat{\eta}_I = 0.2 eV$ reported in [134] implies to be of the order of $0.1 t_1$. Thus the values of the RSOC and ISOC strengths in our thesis are experimentally achievable. The staggered potential (that distinguishes A and B sublattices via different on-site energies) term has been considered as $\hat{\eta}_v = 0.1 t_1$. To include the finite quasiparticle lifetime, we have considered, $\Gamma = 0.1 \Delta_0$.

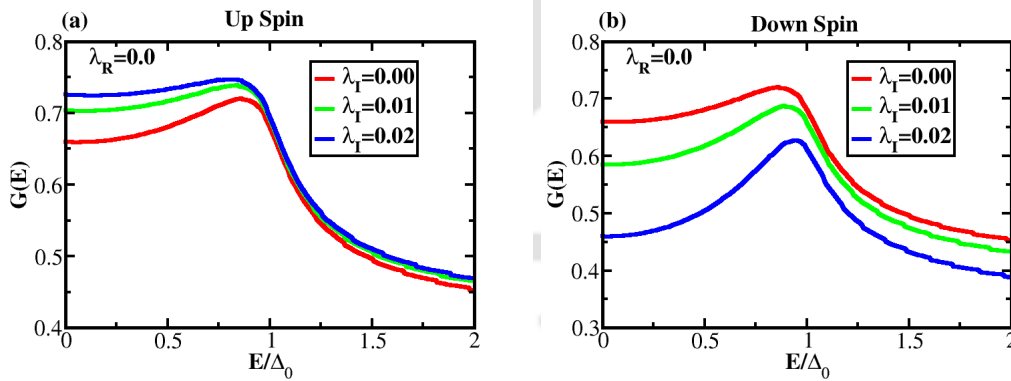


Figure 5.3: (a) The variation of conductance for the up spin, G_{up} , as a function of biasing voltage scaled by the superconducting order parameter, E/Δ_0 , (b) The variation of conductance for the down spin, G_{down} as the function of E/Δ_0 .

In order to realize a competition between the spin-orbit couplings, namely $\hat{\eta}_R$ and $\hat{\eta}_I$, it is contextual to see each of their effects alone. In Fig.(5.1), the spin resolved conductance, G_σ is shown as a function of the biasing energy scaled by the superconducting order parameter, E/Δ_0 , while strength of the RSOC term is varied and the strength of the intrinsic term is kept fixed at zero. The Rashba

free case (pristine graphene) is included for comparison. As expected, the Andreev peak (though the peak is broadened due to the finite quasiparticle life time effects) is observed at $E = \Delta_0$. It is noticed that the conductance for $E < \Delta_0$ is more sensitive to the RSOC compared to that for larger biasing energies, namely, $E > \Delta_0$. In this context we would like to mention that in case of a generic NS junction (parabolic energy dispersion), both spins show identical values for the conductance whereas, the Kane-Mele junction shows the corresponding values to be different. In case of the generic NS junction, it is observed that,

$$G_{\sigma}(E, \partial_{N1}) = G_{-\sigma}(E, -\partial_{N1}) \quad ; \quad G_{\sigma}(E, -\partial_{N1}) = G_{-\sigma}(E, \partial_{N1}) \quad \text{5.3}$$

Thus when we integrate the angle resolved conductance over all possible values of the incident angle, up and down spin shows exactly the same conductance. But in case of graphene based NS junction the above conditions are violated. These facts can be easily understood if we look at Eqn.(2.61). Thus the integration over the incident angles assumes different values for up and down spins, which eventually causes a difference in the spin resolved conductance. Fig.(5.1) reveals

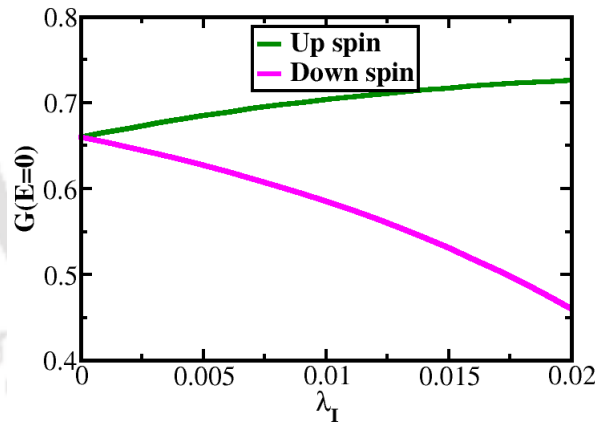


Figure 5.4: The variation of spin resolved conductance, as the function of ISOC strength, $\hat{\lambda}_I$.

that upon increasing strength of the RSOC term, the values of conductance for the both spins decreases.

In Fig.(5.2) we have shown conductance as a function of the strength of the RSOC for different spins. Now the features of charge transport corresponding to different spins can be lucidly observed. This result originates from the behaviour of the AR and the NR and may be explained as follows. From Eqn.(2.25) it is clear that the contribution from the AR term enhances, and the NR term hinders the conductance. We found that for both spins, RSOC enhances the NR term and decreases the AR term. This justifies the results obtained in Fig.(5.2). As we have

discussed earlier, the choice of different adatoms may replicate a similar scenario as depicted above which justifies our considering a range of values for the RSOC.

To ascertain the role of the intrinsic term alone, in Fig.(5.3a) and Fig.(5.3b) we have plotted G_σ vs E/Δ_0 , where the strength of the ISOC term is varied and the RSOC term is kept fixed at zero. The inclusion of the ISOC term shows interesting results in the sense that ISOC enhances the conductance for up spin and diminishes the same for down spin. Naively, we would have thought that the

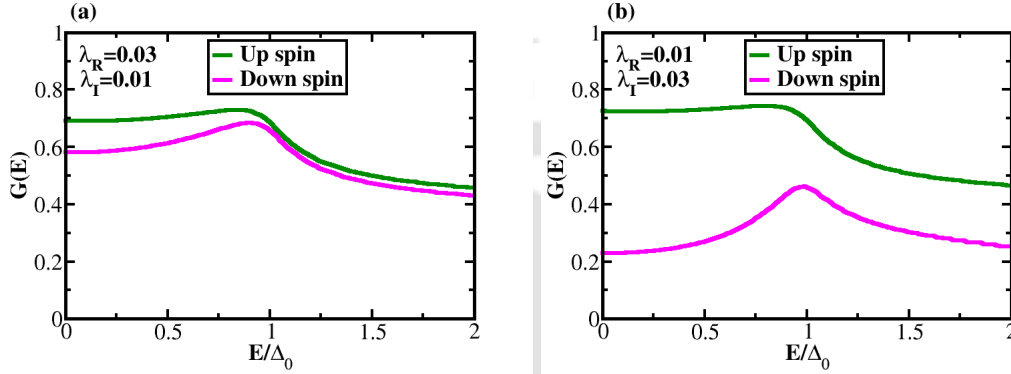


Figure 5.5: The variation of the spin resolved conductance as the function of E/Δ_0 for (a) $\hat{\eta}_R > \hat{\eta}_I$, (b) $\hat{\eta}_R < \hat{\eta}_I$.

RSOC term is responsible for the spin resolved conductance, and having only the ISOC term we should get transport independent of the spin degree of freedom. However with the inclusion of only ISOC, the conditions (see Eqn.(5.3)) discussed in above paragraph are not satisfied which can be understood from Eqn.(2.61). Further, in Eqn.(2.53), the quantity $\hat{\eta}'_{I\nu}$ in the Hamiltonian is accompanied by both the intrinsic and the staggered term, and hence it should augment the difference between the spin polarized transport. The conductance as a function of the ISOC strength (in absence of RSOC) is shown in Fig.(5.4) where we have assumed a zero bias condition. Fig.(5.4) reveals that for up spins, the conductance increases with increasing strength of ISOC, whereas for down spin, the reverse happens. A natural explanation for the observed behaviour is as in the following. This result can be understood again from the behaviour of AR and NR. For an up spin, with increasing strength of ISOC, the contribution of NR decreases and AR increases, whereas opposite trends are obtained for the down spin.

The above results distinguish two types of spin-orbit couplings, namely, in the presence of ISOC, each spin has opposite effects with regard to AR and NR, that is the AR contribution is lowered for the down spin and enhanced for the up spin (reverse happens for NR), while in the presence of RSOC both spins show similar behaviour towards the respective AR and NR contributions.

Next we check what happens to the spin resolved conductance in the presence of both the spin-orbit couplings, that is, now we consider a full Kane-Mele Hamil-

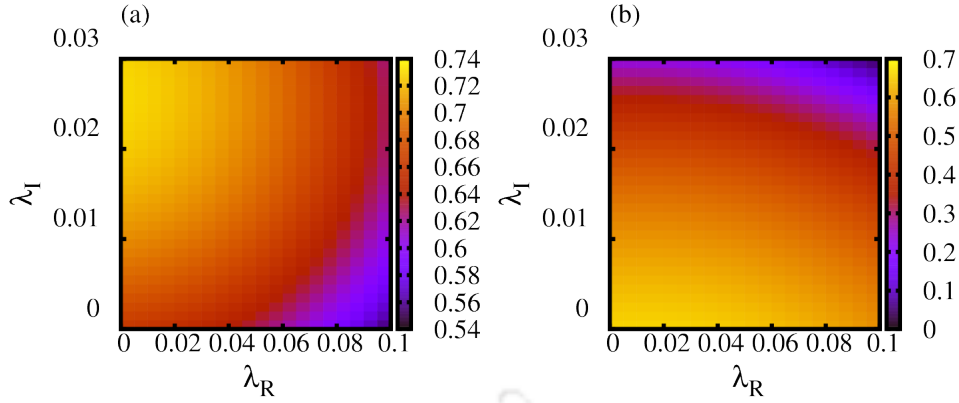


Figure 5.6: The color maps of the spin resolved conductance as the function of $\tilde{\lambda}_R$ and $\tilde{\lambda}_I$ for (a) up spin and (b) down spin.

tonian. In this regard, we have considered two different representative cases, namely, (i) $\tilde{\lambda}_R > \tilde{\lambda}_I$, and (ii) $\tilde{\lambda}_R < \tilde{\lambda}_I$ and the conductance characteristics as a function of E/Δ_0 are shown in Fig.(5.5). The two cases assess whether the relative magnitudes of the RSOC and ISOC terms have any effect on the conductance spectra. Corresponding to both cases, the conductance corresponding to the up spin is greater than that for the down spin. Rest of the features can easily be explained from the results presented earlier, that is those corresponding to $\tilde{\lambda}_R$ or $\tilde{\lambda}_I$ alone.

Next we have shown the spin resolved conductance as the function of both the spin-orbit couplings in Fig.(5.6) with the biasing energy being fixed at $E = 0$. The color plots yield a map showing values of the conductance corresponding to up and down spins for a range of values of the RSOC and the ISOC terms. In case of the up spin, for lower values of the RSOC and higher values of ISOC strengths, the conductance shows large values, whereas in case of down spin, at lower values of the ISOC strength, the conductance becomes large. These maps yield an apriori knowledge of the magnitude of the conductance at low biasing energies for different spins corresponding to a variety of choices of $\tilde{\lambda}_R$ and $\tilde{\lambda}_I$. As it should be possible to correlate the strengths of SOCs to presence of different adatoms, a careful scrutiny of the periodic table may yield useful information on tunable conductance properties of these junction devices.

5.2 Kane-Mele NIS junction

Next we introduce an insulating barrier in between and study a Kane-Mele NIS junction. The schematic diagram of the junction setup has been shown in Fig.(2.5) of the 2nd chapter where the left electrode is a normal ($x \leq 0$) and the right electrode ($x \geq d$) is of a superconducting material with the insulating layer extending from $x = 0$ to $x = d$. The Fermi energy variation across the junction

system is assumed as,

$$E_F(x) = E_F^N \Theta(-x) + E_F^I \Theta(d - x) + E_F^S \Theta(x - d) \quad 5.4$$

where E_F^N and E_F^S are the Fermi energies of the normal and the superconducting leads. E_F^I is the Fermi energy of the insulating barrier which is modeled by, $E_F^I = E_F^N + V_0$.

5.2.1 Results and Discussions on Kane-Mele NIS junction

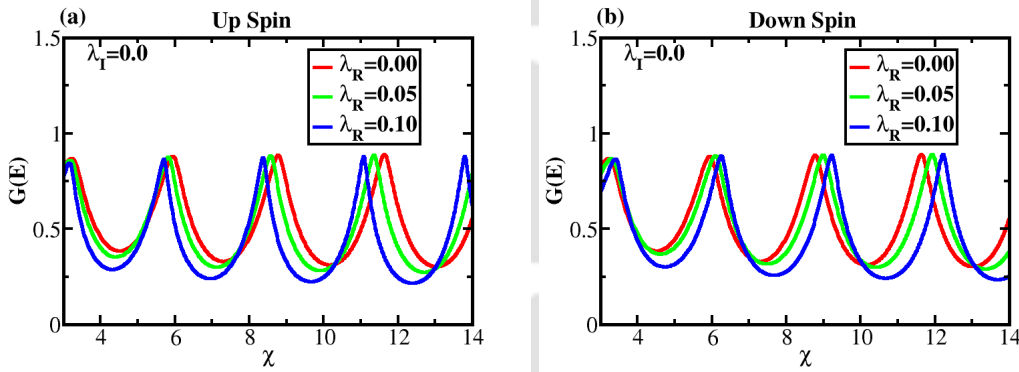


Figure 5.7: The variation of conductance for (a) the up spin, G_{up} and for (b) the down spin, G_{down} as a function of χ with $\hat{n}_I = 0$.

Here we show results for the conductance characteristics of a graphene based NIS junction. As earlier we introduce a dimensionless effective barrier potential, $\chi = k_F^I d$ where k_F^I is the Fermi wave vector and d is the barrier width of the insulating region.

To realize the competition between \hat{n}_R and \hat{n}_I , initially, as earlier, we shall present each of their effects alone. In Fig.(5.7), the spin polarized conductance, G_σ is shown as a function of the effective barrier potential, χ , while the strength of the RSOC term is varied with the strength of the intrinsic term being kept fixed at zero.

As expected, same Fabry-Perot like oscillations are obtained due to the electron interferences. With the inclusion of RSOC it is clearly seen that for an up spin, the peak positions of the conductance have shifted to the left (to lower χ values) compared to that of the RSOC free case, whereas for the down spin, the shifting of the peak positions occur towards the right (larger χ values). Further, with the insertion of RSOC, the minima of the conductance decrease, while the peak values remain almost same. The oscillation pattern with RSOC in graphene based junctions is quite different from that of the generic NIS junction (parabolic energy dispersion). The reason behind of it can be explained as follows. In case

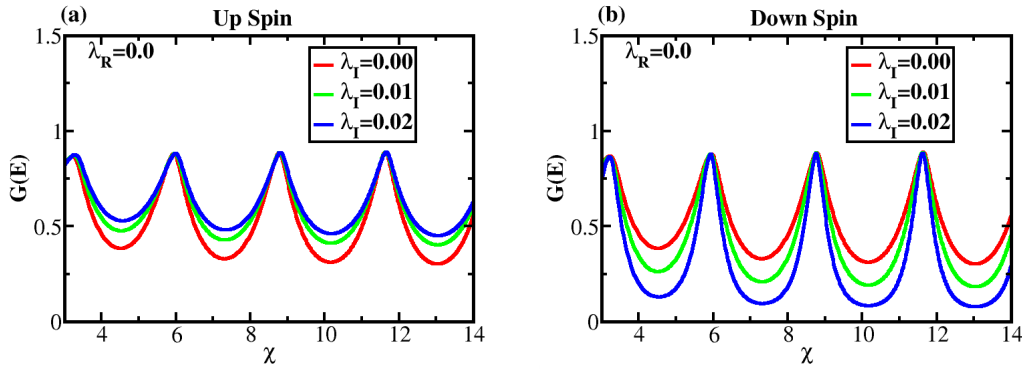


Figure 5.8: The variation of conductance for (a) the up spin, G_{up} and for (b) the down spin, G_{down} as a function of χ with $\hat{\lambda}_R = 0$.

of a generic NIS junction, the BTK formalism is based on the continuity of the solutions of the Schrodinger equation (a second order differential equation) and their derivatives at the interfaces. However, in case of graphene one deals with the Dirac equation (first order differential equation) and hence a single boundary condition is sufficient which ensures the continuity of the wavefunctions at the interfaces. Thus the modification of the oscillation pattern in presence of RSOC should be different which are reflected in Fig.(5.7) and Fig.(3.13).

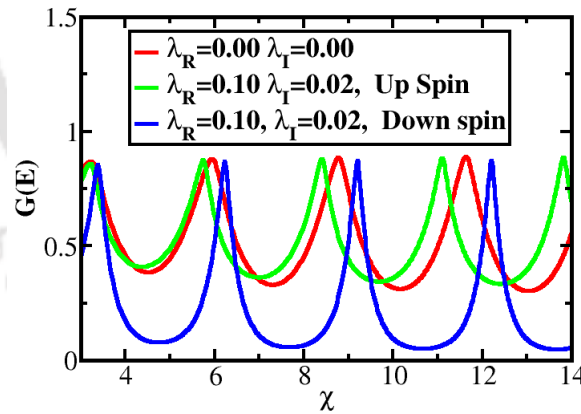


Figure 5.9: The variation of spin resolved conductance as a function of χ for a full Kane-Mele Hamiltonian.

To assess the role of the intrinsic term alone, in Fig.(5.8a) and Fig.(5.8b) we have plotted the G_σ as a function of the χ while strength of the ISOC term is varied and the strength of the RSOC term is kept fixed at zero. Again the peak values of the conductance are unaltered though the conductance near the dip is sensitive to the value of ISOC. It reveals that for an up spin, the conductance near the dips increases with ISOC and for down spin, the reverse happens. This result can be explained from the behaviour of the AR and the NR amplitude which we have

already discussed.

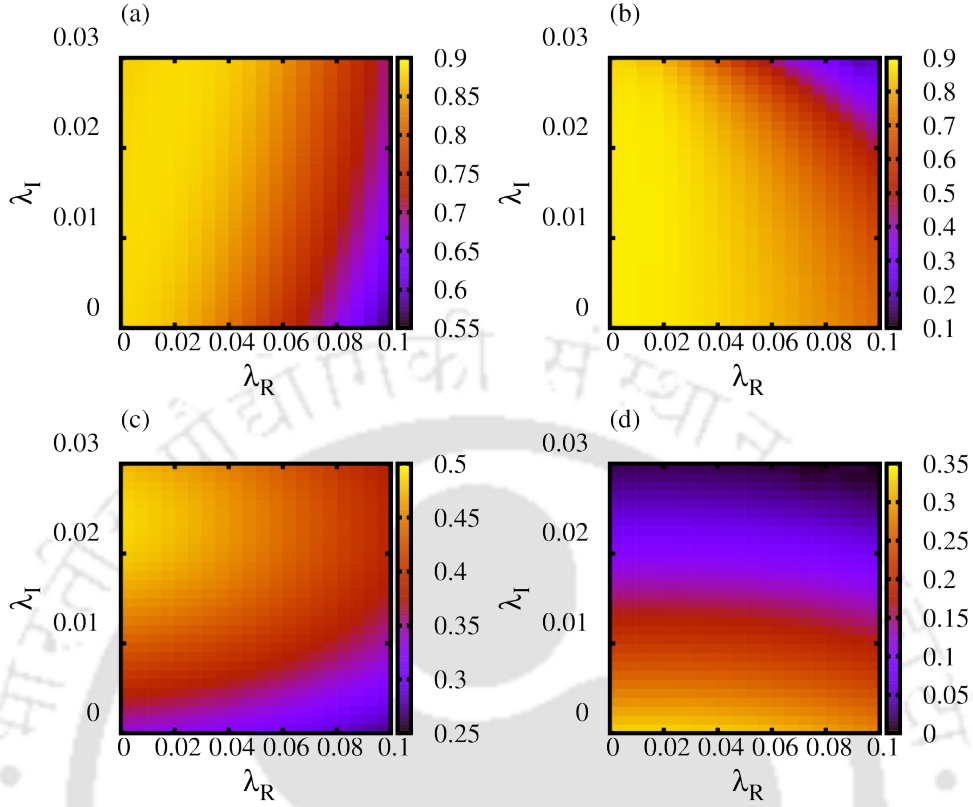


Figure 5.10: The variation of spin resolved conductance as a function of SOC strength for (a) up spin and χ_1 , (b) down spin and χ_1 , (c) up spin and χ_2 , (d) down spin and χ_2 .

Next we check what happens to the spin resolved conductance as function of χ in the presence of both the spin-orbit couplings, that is, now we consider a full Kane-Mele Hamiltonian. In this regard, we have considered particular values, such as, $\hat{\lambda}_R = 0.1t_1$ and $\hat{\lambda}_I = 0.02t_1$. The conductance characteristics of the full Kane-Mele junction as a function of χ is shown in Fig.(5.9). The features can easily be explained from the results presented above, that is those corresponding to $\hat{\lambda}_R$ or $\hat{\lambda}_I$ alone.

Finally to complete our enumeration of the tunability of a Kane-Mele NIS junction, we have shown the spin resolved conductance as the function of both spin-orbit couplings in Fig.(5.10) with the biasing energy is fixed at $E = 0$ for two different values of effective barrier potential, χ . Mainly we have considered χ_1 and χ_2 , where χ_1 denotes the value of the effective barrier potential for which the peaks occur and χ_2 denotes the corresponding value where the minima occur. These maps give an idea of the magnitude of the conductance corresponding to a variety of choices of $\hat{\lambda}_R$ and $\hat{\lambda}_I$. As the strengths of SOCs are correlated to presence of different adatoms, a careful choice of (heavy) element from the periodic table may provide useful information on tunable conductance of these junction devices.

5.3 Conclusion

In summary, we have investigated the spin resolved transport properties of a Kane-Mele NS junction by employing BTK theory. Hence we have studied the conductance properties in details with regard to each of the RSOC and ISOC contribution to the spin dependent transport. We have found that the RSOC hinders the tunneling conductance for both the spins, whereas ISOC augments the conductance for an up spin and hinders for the down spin.

Further, we have investigated the tunneling conductance of a Kane-Mele NIS junction. The key results can be highlighted as follows. We observe an oscillatory behavior for the tunneling conductance spectrum as a function of the effective barrier potential. The spin-orbit terms show interesting effects on the oscillation pattern. The RSOC term shifts both the peak and dip positions causing an overall shift of the pattern. With the inclusion of RSOC, there is no change in peak values, whereas the conductance near the dip decreases for both the spins. Further ISOC term does not shift the peak positions, though it enhances the conductance for the up spin near the dip and diminishes it for the down spin.

Summarizing the above observations it may be inferred that as the strength of the SOC terms can be manipulated via different adatoms or using gate voltages etc, we conclude that a tunable conductance remains an experimental possibility.

Chapter 6: Thermoelectric effects of Kane-Mele NIS junction

The recent development in feasible fabrication techniques for graphene, has allowed for exploratory studies of this system. From the application point of view, graphene is a potential candidate due to its high mobility. Further in graphene the carrier density can be controlled by external gate voltage, which makes it a good candidate for fabrication of devices. In order to apply graphene to electric devices, it is an important topic to study the characteristics of charge and heat transport.

Recently, the thermal and thermoelectric properties of graphene structure have gained much attention because of the large Seebeck coefficient and high thermal conductivity obtained in graphene sheets [76–78]. Previously, due to the experimental limitations in accessing nano-scale devices, the charge and spin dependent thermoelectric properties were often ignored [162, 163]. But recently improved techniques in low temperature measurements devices provides an opportunity of experimental observation of thermoelectric physics. Very recently Zuev et al [77] and Wei et al. [133] have performed theoretical and experimental investigation of the thermoelectric effects of graphene sheets.

In a parallel front, the quantum transport through the junction devices are gaining increased attention in the field of modern research for developing the nano-devices at atomic/molecular level. The junction devices have interesting applications in the fields of thermoelectric, thermometric, solid state cooling etc. In the past a good number of studies on junction has been performed in these fields [7, 17, 18] and the junction devices are very useful in wide range of experiments and applications [8–10]. The recent development in the field of thermoelectric physics in small scale junction devices provides a new direction for fabricating self-cooling devices, thermopower devices etc.

We have already discussed that two types of spin-orbit couplings (SOC) are proposed in graphene by Kane and Mele. Though the strengths of the spin-orbit couplings are very small, it is possible to induce enhanced SOC strengths in graphene via different techniques, such as, such as via adatoms [87], using proximity effect of a three dimensional topological insulators [50, 88], by functionalization with methyl groups [89] etc. Moreover the tunability of RSOC strength via an external gate voltage provides an additional impetus in the field of spintronics. It is worth to mention that SOC's are very significant and hence cannot be skipped in the context of transport. Since both the charge and thermal current are very sensitive to the strength of SOC's and owing to the tunability of the SOC parameters, a Kane-Mele NIS junction can be a good candidate for a tunable

thermoelectric device.

Motivated by the above, we have performed an extensive study of the thermoelectric effect of a Kane-Mele normal-insulator-superconductor (KMNIS) nano-junction by employing the modified Blonder-Tinkham-Klapwijk (BTK) theory. Physically the scenario corresponds to adatom decorated graphene NIS junction to account for finite strengths of the spin-orbit couplings. We have computed the spin resolved thermopower, Figure of Merit, thermal current, coefficient of performance and explored how the spin-orbit couplings (induced by adatoms or otherwise) assume roles in shaping up the thermoelectric properties of such a junction.

For better readability, let us comment on the organization of our work. To make notations clear, we briefly describe the system in section(6.1). Formulae of Seebeck coefficient and thermal current are depicted in subsection(6.1.1) and in subsection(6.1.2) respectively. The results on the thermopower and thermoelectric cooling of this junction device are discussed in section(6.2). In section(6.3) we summarize our results and highlight the tunability of the junction device with regard to its thermoelectric properties.

6.1 Kane-Mele NIS junction

In Fig.(2.5) the schematic diagram of the junction setup has been shown where the left electrode is a normal ($x \leq 0$) and the right electrode ($x \geq d$) is a superconducting material with the insulating layer is extending from $x = 0$ to $x = d$. As earlier, the insulating layer is modeled by an external gate voltage such that the Fermi energy is ramped by V_0 . It is considered that the $x \geq d$ region of the junction system has been produced by proximity effect by an external superconductor.

The effective Hamiltonian for Kane-Mele system is given in Eqn.(5.1) and the simplification of Kane-Mele Hamiltonian is elaborately discussed in Chapter 2. The Fermi energy variation across the junction system is assumed as,

$$E_F(x) = E_F^N \Theta(-x) + E_F^I \Theta(d - x) + E_F^S \Theta(x - d) \quad 6.1$$

where E_F^N and E_F^S are the Fermi energies of the normal and the superconducting leads. E_F^I is the Fermi energy of the insulating barrier which is defined by, $E_F^I = E_F^N + V_0$.

The expression for the charge current through the KMNIS junction using BTK theory can be found to have the following form,

$$I_{NS\sigma}(E_F^N, T_N, E_F^S, T_S) = eA_r v_F^N \int \int \tau_\sigma(E, \partial_{N1}) [f^N(E_F^N, T^N) - f^S(E_F^S, T_S)] N(E) dE \cos \partial_{N1} d\partial_{N1} \quad 6.2$$

where $N(E)$ denotes the density of states, v_F^N is the Fermi velocity, A_r is the area of contact, and f^N, f^S are the Fermi distribution functions for the normal and the superconducting leads respectively. $\tau_\sigma(E, \partial_{N1})$ is the transfer probability. where $\tau_\sigma(E, \partial_{N1}) = 1 - |b_\sigma(E, \partial_{N1})|^2 + \frac{\cos \partial_{N2}}{\cos \partial_{N1}} |a_\sigma(E, \partial_{N1})|^2$, a_σ is amplitude of Andreev reflection, b_σ is amplitude of normal reflection. The derivation for finding the amplitudes of normal and Andreev reflections are presented in chapter 2. As the normal state resistance, R_N is defined by, $R_N = \frac{1}{2e^2 N_0 v_F^N A_r}$ (2 comes due to the spin degeneracy, N_0 denotes the density of state at Fermi level), the electrical charge current takes the following form,

$$I_{NS_\sigma}(E_F^N, T_N, E_F^S, T_S) = \frac{1}{2eR_N N_0} \int \int \tau_\sigma(E, \partial_{N1}) [f^N(E_F^N, T^N) - f^S(E_F^S, T_S)] N(E) dE \cos \partial_{N1} d\partial_{N1} \quad 6.3$$

where the energy dependent quantity,

$$N(E) = \frac{|E_F^N + E|W}{\pi \hbar V_F^N} \quad 6.4$$

is the number of transverse modes in graphene sheet of width W [160].

6.1.1 Seebeck coefficient

We consider the left and right electrodes serve as independent temperature reservoirs where the left electrode is fixed at temperature, $T^N = T - \delta T/2$ and the right electrode is fixed at temperature $T^S = T + \delta T/2$. The population of electrons in the left and the right lead is described by the Fermi-Dirac distribution function, f^N and f^S respectively, where $E_F^N = E_F^S$ at zero external bias.

The temperature difference between two dissimilar materials produces a voltage difference between the two substances and this phenomenon is known as Seebeck effect. Seebeck coefficient is a measurement of the amount of potential induced in the device for unit temperature difference and defined by, $S = \delta V / \delta T$.

Let us now consider an extra infinitesimal current induced by an additional voltage, δV and the temperature difference, δT across the junction in an open circuit. The current induced by δT and δV are given by, $(dI)_T = I(E_F^N, T^N, E_F^S = E_F^N, T^S = T^N + \delta T)$ and $(dI)_V = I(E_F^N, T^N, E_F^S = E_F^N + e\delta V, T^S = T^N)$. Suppose that the current cannot flow in an open circuit, thus $(dI)_T$ counter balances $(dI)_V$. It allows us to write,

$$dI = (dI)_T + (dI)_V = 0 \quad 6.5$$

where the expression for the $(dI)_T$ and $(dI)_V$ can be obtained from Eqn.(6.3). Now first order expansion of Fermi-Dirac distribution function in $(dI)_T$ and $(dI)_V$ while the energy is shifted by Fermi energy, yields the expression for the spin dependent

Seebeck coefficient,

$$S_\sigma = \frac{\delta V}{\delta T} = \frac{\int \int dE d\partial_{N1} \cos \partial_{N1} E (E_F^N + E) \iota_\sigma(E, \partial_{N1}) \frac{\partial f}{\partial E}}{eT \int \int dE d\partial_{N1} \cos \partial_{N1} (E_F^N + E) \iota_\sigma(E, \partial_{N1}) \frac{\partial f}{\partial E}} \quad 6.6$$

Now the charge and spin Seebeck coefficients are usually defined by [164],

$$S_{ch} = \frac{1}{2}(S_{up} + S_{down}) ; S_{sp} = \frac{1}{2}|S_{up} - S_{down}| \quad 6.7$$

which can be computed from Eqn.(6.6) for $\sigma = up/down$.

The efficiency of the device depends upon a quantity called as 'Figure of Merit' (FM). To get a clear idea of the efficiency, one should compute the spin dependent FM which is given by,

$$Z_\sigma T = \frac{S_\sigma^2 G_\sigma}{K_\sigma} T \quad 6.8$$

where S_σ is Seebeck coefficient, G_σ is electrical conductance, K_σ is thermal conductance, and T is absolute temperature. G_σ can be calculated from the relation $G_\sigma = \frac{dI_{NS\sigma}}{dV}$ and is given by the form,

$$G_\sigma = \frac{1}{2eR_N E_F^N} \int \int \iota_\sigma(E, \partial_{N1}) \left(-\frac{\partial f}{\partial E}\right) (E + E_F^N) dE \cos \partial_{N1} d\partial_{N1} \quad 6.9$$

The thermal conductance K_σ , can be calculated from the relationship $K_\sigma = \frac{dJ_{NS\sigma}}{dT}$ where $J_{NS\sigma}$ is the thermal current flowing from the normal region to the superconducting region. In the next subsection we shall discuss how the thermal current and the thermal conductance can be calculated.

In addition, the charge FM ($Z_{ch}T$) and spin FM ($Z_{sp}T$) are defined as [164–166],

$$Z_{ch}T = \frac{S_{ch}^2 (G_{up} + G_{down})T}{K_{up} + K_{down}} ; Z_{sp}T = \frac{S_{ch}^2 |G_{up} - G_{down}|T}{K_{up} + K_{down}} \quad 6.10$$

6.1.2 Thermoelectric cooling

As said earlier, the left electrode, that is the normal lead serves as the cold reservoir and the right one serves as hot reservoir. The junction device is connected to an external bias voltage, $V_B = (E_F^N - E_F^S)/e$, which drives the electrons to flow from the normal lead to the superconducting lead. Thus the electron removes the heat energy from the normal lead and transfers it to the superconducting lead which further makes the cold reservoir (normal) cool. The thermal current from

normal to superconducting leads is given by,

$$J_{NS_\sigma} = \frac{1}{2e^2 R_N E_F^N} \int \int (E - eV_B)(E + E_F^N) \tau'_\sigma(E, \partial_{N1}) [f^N(E - eV_B, T^N) - f^S(E, T^S)] dE \cos \partial_{N1} d\partial_{N1} \quad 6.11$$

Similarly,

$$J_{SN_\sigma} = \frac{1}{2e^2 R_N E_F^N} \int \int E(E + E_F^N) \tau'_\sigma(E, \partial_{N1}) [f^N(E - eV_B, T^N) - f^S(E, T^S)] dE \cos \partial_{N1} d\partial_{N1} \quad 6.12$$

while energies are shifted by Fermi energy and τ'_σ is given by the form,

$$\tau'_\sigma(E, \partial_{N1}) = 1 - |b_\sigma(E, \partial_{N1})|^2 - \frac{\cos \partial_{N2}}{\cos \partial_{N1}} |a_\sigma(E, \partial_{N1})|^2 \quad 6.13$$

This normal-insulator-superconductor (NIS) junction can be regarded as the electronic cooling device only when $J_{NS_\sigma} > 0$, which implies that it is capable to remove the heat from the cold reservoir, thereby making it cooler.

Hence the thermal conductance, $K_\sigma = \frac{dJ_{NS_\sigma}}{dT}$ is given by the form,

$$K_\sigma = \frac{1}{2e^2 R_N E_F^N} \int \int (E - eV_B)(E + E_F^N) \tau'_\sigma(E, \partial_{N1}) \left[\frac{f^N(E - eV_B, T^N)}{dT} - \frac{f^S(E, T^S)}{dT} \right] dE \cos \partial_{N1} d\partial_{N1} \quad 6.14$$

The performance of this junction as a self-cooling device can be measured by the coefficient of the performance (COP) where COP is defined as the ratio of the heat removed from the cold reservoir to the electrical power needed for driving the system. The COP for electronic thermal current, namely, COP_σ is given by,

$$COP_\sigma = \frac{J_{NS_\sigma}}{I_{NS_\sigma} V_B} = \frac{J_{NS_\sigma}}{J_{NS_\sigma} - J_{SN_\sigma}} \quad 6.15$$

6.2 Results and Discussions

We have investigated the thermoelectric effect of a graphene based normal-insulator-superconductor (NIS) junction device in the presence of Rashba and intrinsic spin-orbit couplings assumably induced by the transition metal adatoms, where the effects of the spin-orbit couplings are mimicked by the Kane-Mele model [82, 83]. Here we include a note on the values of various parameters used for our numerical computation. We have assumed, $E_F^N = 50\Delta_0$. In this chapter we shall keep χ to be fixed, unlike the earlier cases, where the thermoelectric behaviour

as a function of χ has received wide attention. Here our focus is to tune both the RSOC and ISOC terms and concentrate on the interplay of these two spin-orbit couplings on the thermoelectric properties. However we have considered a particular value of χ where the conductance (charge) records the maximum value. Fermi velocity and the hopping parameter t_1 can be calculated from the Fermi energy through the relations $E_F = \hbar v_F k_F$ and $v_F = \frac{3t_1 a}{2\hbar}$. The strength of the NN hopping, \hat{n}_R and the NNN hopping, \hat{n}_I are considered in units of t_1 and varied in the range $[0 : 0.17t_1]$ and $[0 : 0.02t_1]$ respectively. In our work, the strength of the \hat{n}_R and \hat{n}_I are taken as parameters and the thermoelectric effects are computed for various choices of these parameters. Physically, it implies decorating the graphene nanoribbon by adatoms which induce the SOC couplings. Finally the staggered term is taken as $\hat{n}_v = 0.1t_1$.

6.2.1 Seebeck Coefficient and Figure of Merit

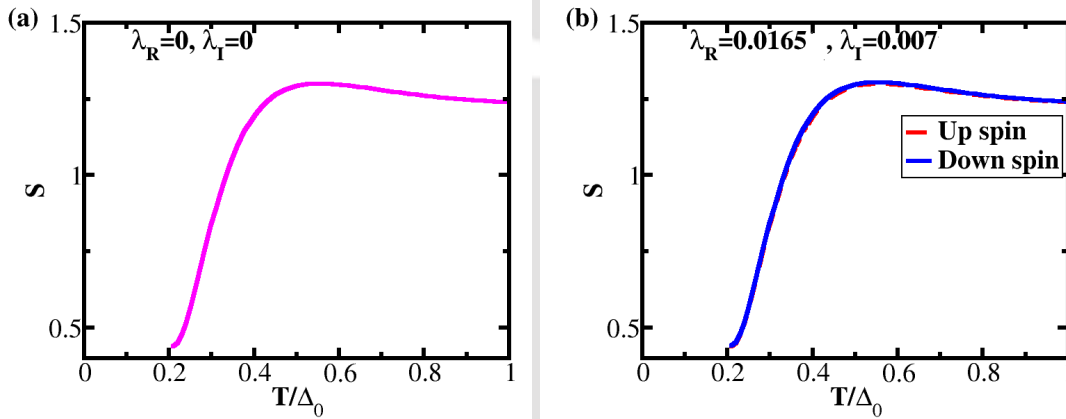


Figure 6.1: The variation of the Seebeck coefficient, S as a function of temperature, T (scaled by superconducting order parameter, Δ_0) (a) for pristine graphene, (b) for Au decorated graphene. The values of the spin-orbit coupling are shown in the figure.

Initially we show the results of Seebeck coefficient for a pristine graphene ($\hat{n}_R = 0, \hat{n}_I = 0$). The variation of the Seebeck coefficient, S as function of the temperature (in units of superconducting gap, Δ_0) for a pristine graphene is shown in Fig.(6.1a). This is included for comparison with that of Fig.(6.1b). The Seebeck coefficient, S is dimensionless (since $e = 1$ and $k_B = 1$). It is understood that the Seebeck coefficient increases initially with temperature and after attaining a certain value it decreases very slowly. In this regard we should remind ourselves that the temperatures should be in a range such the superconductivity is not destroyed. From BCS theory it can be shown that the relationship between superconducting temperature and the superconducting order parameter is $T_c \sim (0.5 - 0.6)\Delta_0$. Now to get an idea about the role of spin-orbit couplings

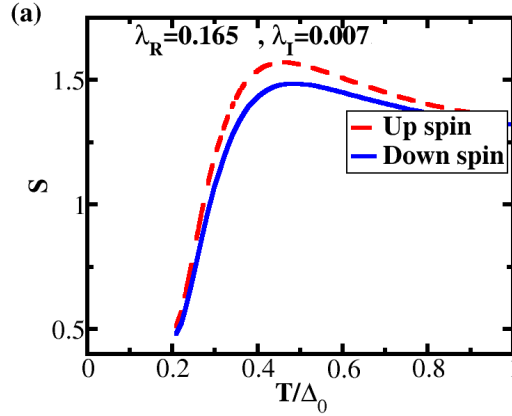


Figure 6.2: The variation of the Seebeck coefficient, S as a function of temperature, T/Δ_0 for a larger RSOC parameter by one order greater magnitude compared to that of the Au decorated graphene.

on value of the thermopower, in Fig.(6.1b) we present the variation of the spin resolved Seebeck coefficient, S as function of the temperature (in units of superconducting gap, Δ_0) for an Au decorated graphene. From the first principal calculations, in the Au decorated graphene the values of the following parameters are, $\beta_I = 0.007t_1$ and $\beta_R = 0.0165t_1$ [87] and one does not notice any significant change in the thermopower profile. Thus, by some means if we are able to en-

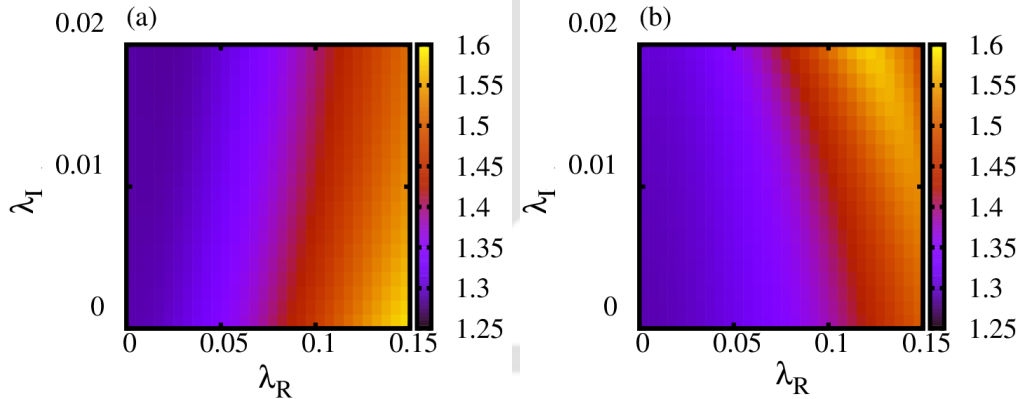


Figure 6.3: The variation of the spin resolved Seebeck coefficient, S as function of β_R and β_I for (a) up spin, (b) down spin. Reddish yellow regions indicate the parameters values needed for the achieving maximum, S .

hance the SOCs by one order of magnitude compared to the value present in the Au decorated graphene, there could be noticeable effects of SOC. Thus in Fig.(6.2) we have shown the thermopower profile with one order of greater magnitude of RSOC strengths where, indeed noticeable changes are obtained. For this reason in the later discussions we shall use these values of the SOCs strength. The interesting fact is that, in case of a normal junction (that is not graphene based) in the presence of RSOC, there is no spin resolved thermopower, which graphene

based junction devices, in presence of a bit high RSOC strengths show the spin resolved thermopower. The reason behind the spin resolved Seebeck coefficient is the same as that of the spin resolved conductance which has been explained in previous chapter. It is clearly understood that with the inclusion of the SOC parameters the Seebeck coefficient increases. Further the up spin shows larger values of thermopower compared to that of the down spin.

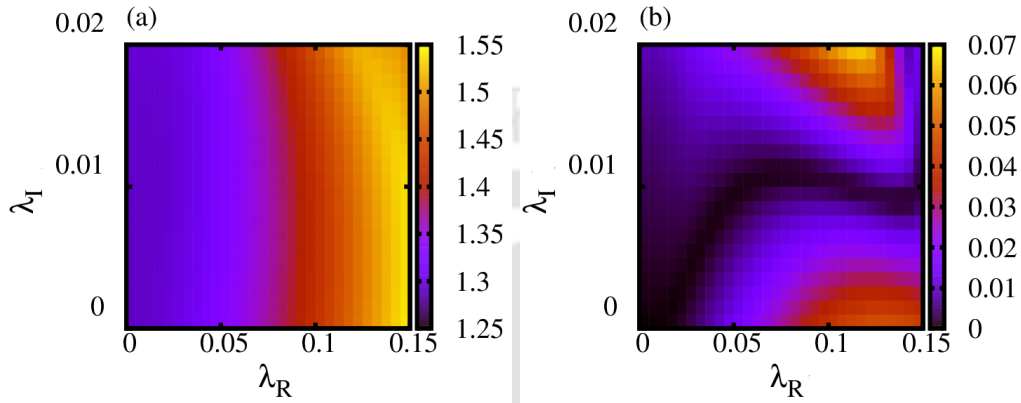


Figure 6.4: (a) The variation of the charge Seebeck coefficient as function of $\hat{\lambda}_R$ and $\hat{\lambda}_I$, (b) The variation of the spin Seebeck coefficient as function of $\hat{\lambda}_R$ and $\hat{\lambda}_I$.

To get an idea how the spin resolved Seebeck coefficient vary with both of the spin-orbit couplings, and also to get an operating regime in the parameter space, we have shown the spin resolved Seebeck coefficient as a function of $\hat{\lambda}_R$ and $\hat{\lambda}_I$ in Fig.(6.3a) and Fig.(6.3b) with temperature, $T = 0.5\Delta_0$. The color plots yield the information of the Seebeck coefficient for different values of the RSOC and the ISOC parameters. For certain values of the RSOC parameter ($> 0.1 t_1$), irrespective of the ISOC strength, both spins show higher values of thermopower, So we can infer that for both the spins RSOC enhances the thermopower.

Further we have shown results of the charge and spin Seebeck coefficients in Fig.(6.4a) and Fig.(6.4b). The charge Seebeck coefficient shows higher values for larger strengths of RSOC, and for certain values of the SOC parameters, the spin Seebeck coefficient vanishes. This map gives an idea of the magnitude of the Seebeck coefficient corresponding to a variety of choices of $\hat{\lambda}_R$ and $\hat{\lambda}_I$. As the strengths of SOC's correspond to presence of different adatoms, a careful choice of the periodic table may provide useful information on tunable thermopower of these junction devices.

Now we show the results on the 'Figure of Merit' (FM) which defines the efficiency of this system as a thermopower device. The variation of the Figure of Merit, ZT as function of the temperature (in units of superconducting gap, Δ_0) is shown in Fig.(6.5). It shows that, initially with temperature the efficiency of the system as a thermopower device increases and, after attaining a certain temperature it

decreases. The variations of the spin dependent FM, $Z_\sigma T$ as the function of the

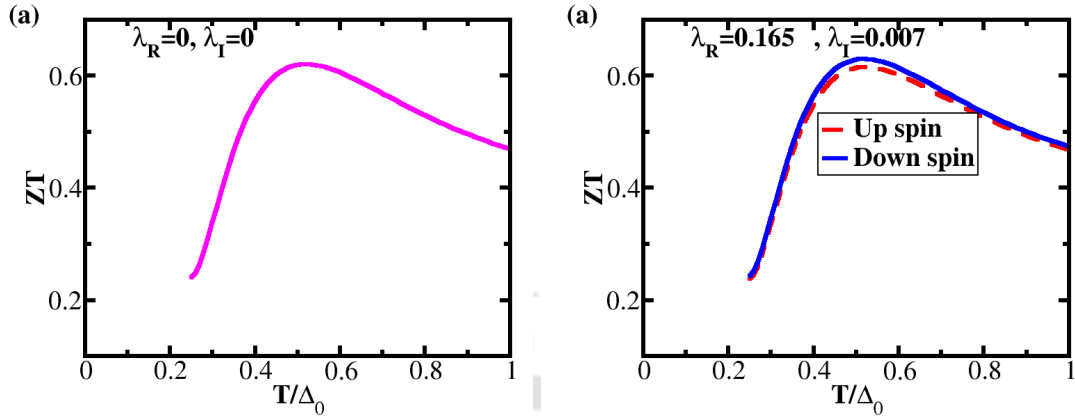


Figure 6.5: The variation of Figure of Merit, ZT as a function of temperature, T (scaled by superconducting order parameter, Δ_0) for (a) $\hat{\lambda}_R = 0$ and $\hat{\lambda}_I = 0$, (b) $\hat{\lambda}_R = 0.165t_1$ and $\hat{\lambda}_I = 0.007t_1$.

spin-orbit couplings are presented in Fig.(6.6). This map gives an idea of the FM for different spins corresponding to different choices of $\hat{\lambda}_R$ and $\hat{\lambda}_I$. Interestingly, the down spin shows more efficiency compared to that of the up spin. Further we

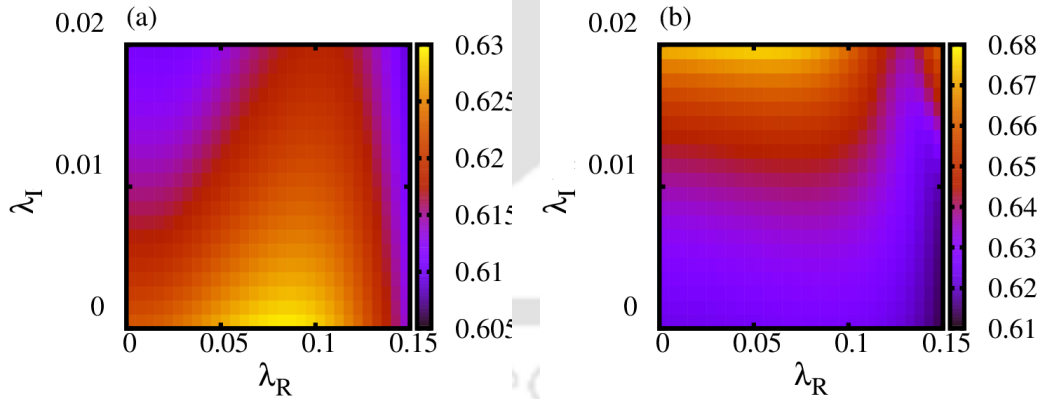


Figure 6.6: The variation of the 'Figure of Merit', ZT as function of $\hat{\lambda}_R$ and $\hat{\lambda}_I$ for (a) up spin and (b) down spin.

have shown the results for charge and spin FM in Fig.(6.7a) and Fig.(6.7b) where it is observed that for higher values of ISOC the charge FM becomes larger. The spin FM becomes zero for the lower values of the RSOC parameters irrespective of the ISOC strengths. Such regions, along with others, are shown by black patches in Fig.(6.7b). Thus these maps aid in deciding on the values of the parameters that may be used for maximizing the gain of these KMNIS junction devices.

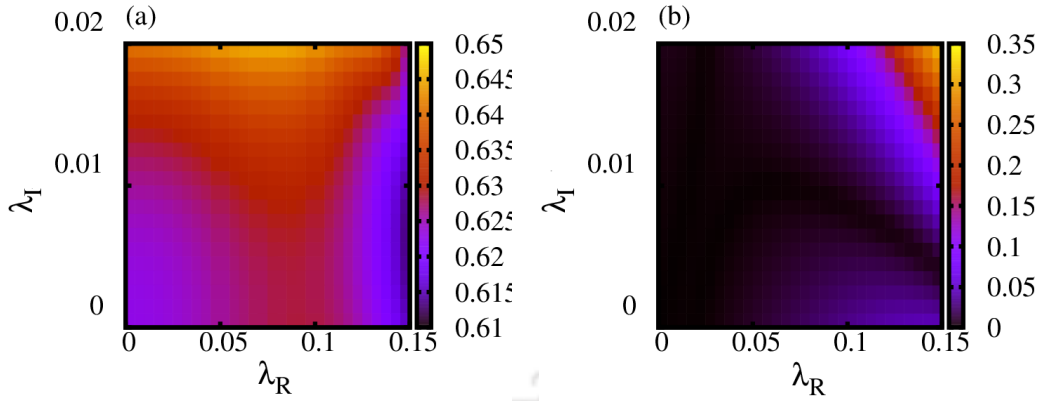


Figure 6.7: (a) The variation of the charge 'Figure of Merit', $Z_{ch}T$ as function of $\hat{\lambda}_R$ and $\hat{\lambda}_I$, (b) The variation of the spin 'Figure of Merit', $Z_{sp}T$ as function of $\hat{\lambda}_R$ and $\hat{\lambda}_I$.

6.2.2 Thermoelectric cooling and coefficient of performance

Here we show the results of the thermoelectric cooling of the KMNIS junction. To get an idea about the role of spin-orbit coupling on the thermal current, in Fig.(6.8) we present the variation of a dimensionless quantity, $2J_{NS}e^2R_N/\Delta_0^2$ as a function of biasing voltage where the temperature is fixed at $T = 0.5\Delta_0$ and the temperature difference, δT that exists across the junction is taken as, $\delta T = 0.02 \times \Delta_0$. It is evident that at zero biasing voltage, the rate of the thermal current

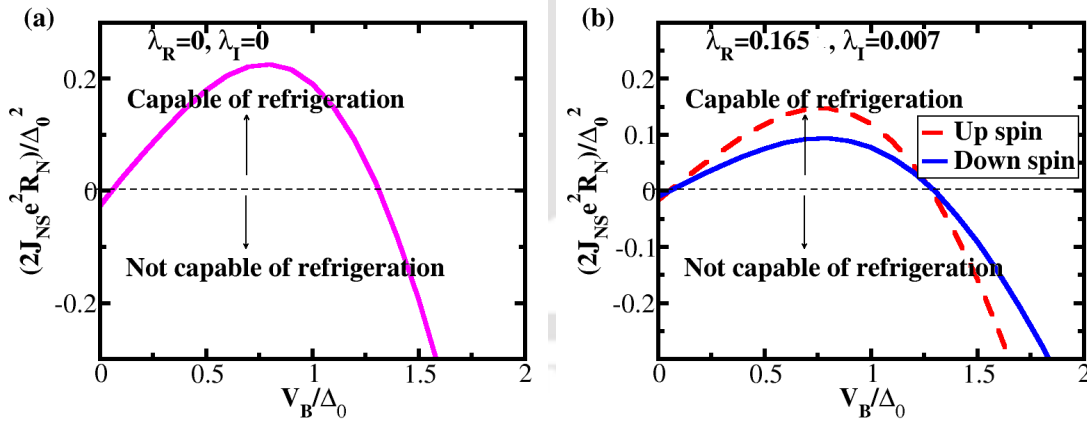


Figure 6.8: The variation of the dimensionless thermal current, $2J_{NS}e^2R_N/\Delta_0^2$ as a function of biasing voltage, V_B (scaled by superconducting order parameter, Δ_0) for (a) $\hat{\lambda}_R = 0$ and $\hat{\lambda}_I = 0$, (b) $\hat{\lambda}_R = 0.165t_1$ and $\hat{\lambda}_I = 0.007t_1$. The operating regions are indicated.

extracted from the cold (normal) reservoir is negative. Thus, to achieve cooling effects, a (lower) threshold voltage of the battery, V_{lower} is needed. That is, the thermoelectric cooling does not work, when $V_B < V_{lower}$. Also beyond an upper threshold voltage, V_{upper} , the refrigeration effect ceases to exist. From the plots it is visible that for a very small range of the biasing voltage (having values in

the vicinity of the superconducting order parameter), the thermoelectric cooling process is efficient and the maximum refrigeration occurs at around, $V_B \sim 0.9\Delta_0$. With the inclusion of SOC parameters, a significant decrease in thermal current is obtained. Moreover, we have checked that a lower threshold of the voltage, V_{lower} required to trigger the cooling effect does not depend on the choice of the SOC parameters.

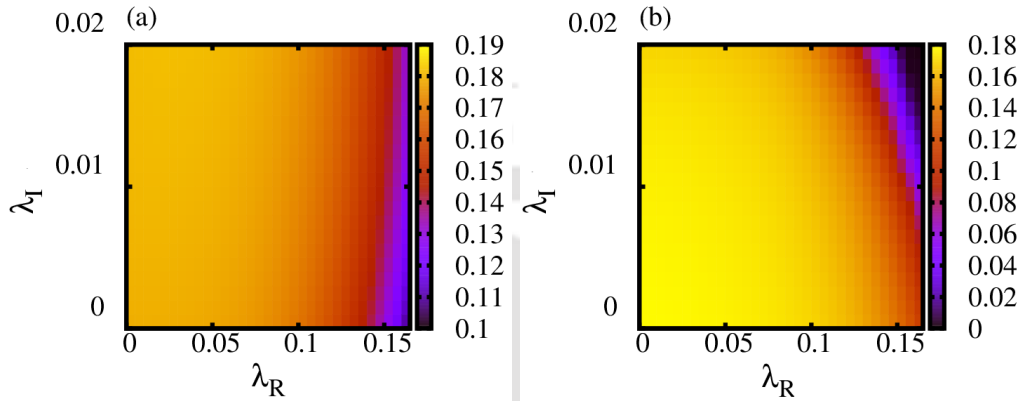


Figure 6.9: The variation of the thermal current, $2J_{NS}e^2R_N/\Delta_0^2$ as a function of $\hat{\lambda}_R$ and $\hat{\lambda}_I$ for (a) up spin and (b) down spin.

Next we have shown the spin resolved thermal current as the function of both the spin-orbit couplings in Fig.(6.9a) and Fig.(6.9b) which provides an idea of the desired range of values of the RSOC, the ISOC parameters and the corresponding thermal current. The biasing voltage is fixed at $V_B = 0.5\Delta_0$. For higher values of the RSOC parameter, the thermoelectric cooling for both spins becomes smaller. As the SOC parameters are tunable by different techniques, the color plots gives useful information on the tunable thermoelectric cooling.

Here we show the results of the performance of the KMNIS junction as a self-cooling device. To recapitulate, a measure of the performance and the efficiency of the KMNIS junction as a thermoelectric nano-refrigerator is defined by the coefficient of performance (COP). Fig.(6.10) reveals that for a narrow range of the biasing voltage, the nano refrigeration works (namely, $0.06\Delta_0 - 0.9\Delta_0$). Since Δ_0 is in *meV* range for conventional superconductor, the operating voltage is low. Further it is understood that when the driving voltage exceeds the value of the superconducting order parameter, Δ_0 , the refrigeration vanishes, irrespective of the strengths of SOC.

Finally to complete our enumeration of the tunability of a KMNIS junction, the COP is plotted as a function of the RSOC and ISOC strengths in Fig.(6.11a) and Fig.(6.11b). The color plots provide the idea of the range of values of the RSOC, the ISOC parameter and the corresponding coefficient of performance. The biasing voltage is fixed at $V_B = 0.125\Delta_0$ where the COP shows high values. It is clear

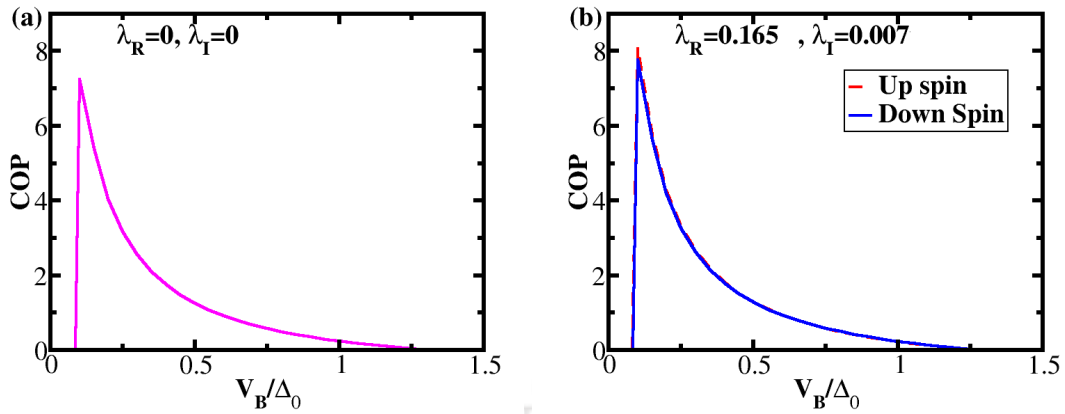


Figure 6.10: The variation of the coefficient of performance, COP as a function of biasing voltage, V_B (scaled by superconducting order parameter, Δ_0) for (a) $\hat{\lambda}_R = 0$ and $\hat{\lambda}_I = 0$, (b) $\hat{\lambda}_R = 0.165t_1$ and $\hat{\lambda}_I = 0.007t_1$.

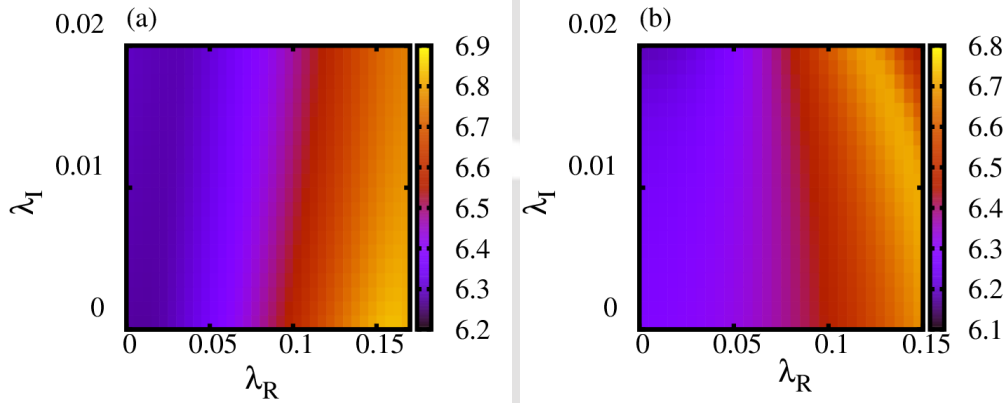


Figure 6.11: The variation of the COP as a function of $\hat{\lambda}_R$ and $\hat{\lambda}_I$ for (a) up spin and (b) down spin.

that the RSOC helps to enhance the COP for both spins. The color plots provide a helpful hint on the tunable coefficient of performance.

6.3 Conclusion

In summary, we have investigated the thermoelectric properties of a KMNIS junction in presence of spin-orbit couplings by employing BTK theory in great details. We have investigated the Seebeck coefficient and the thermoelectric Figure of Merit of this junction device and explained how SOC parameters play a role in determining these properties. Further the thermoelectric cooling of this junction device and its performance as a cooling device have been studied in details. It is clear that the thermoelectric properties are sensitive to the SOC parameters. As the strength of the SOC terms can be manipulated via different adatoms or using gate voltages etc, we may infer that it is possible to achieve a precision tuning of

the thermoelectric properties of these junction devices.





Chapter 7: Comparison between generic and graphene based junction system in charge and heat transport

In the previous chapters we have studied charge and heat transport of 2D junction systems in presence of Rashba (along with intrinsic for graphene) spin-orbit coupling considering both the usual (with parabolic energy dispersion) and graphene (having linear energy dispersion near the Fermi energy which is crucial for transport) based junction systems. In this chapter our motivation is to briefly compare the results on charge and heat transport between these two systems. We wish to make it clear that we shall not involve ourselves in a full blown comparison between the two with regard to every physical quantity that has been studied earlier. Mainly we want to check which of the two is more effective to generate electrical current, thermopower or is more useful to the phenomenon of thermoelectric cooling.

7.1 Comparison for electrical current

Initially we include a note on the values of various parameters used for our numeric computation. We have assumed the Fermi energy of the metallic lead, $E_F^N = 50\Delta_0$ where Δ_0 is the superconducting gap with a conventional *s*-wave symmetry. The Fermi energy of the superconducting lead has been taken as $E_F^S = 2E_F^N$, that is, a Fermi surface mismatch of $\hat{\eta} = 2$. To include the effect of Rashba term, the value of the dimensionless quantity, $\hat{\eta}_R$ has been taken as 0.5. Here we like to point that in previous chapters, we have taken the strength of RSOC for graphene based junction in units of t_1 . Here, to compare with the usual junction, we have taken the strength of $\hat{\eta}_R$ in units of E_F^N . As our aim is to compare both the systems, we have skipped the intrinsic and staggered terms for graphene based junction. For insertion of finite quasiparticle lifetime, we have considered, $\Gamma = 0.1\Delta_0$. Further, only *s*- wave pairing symmetry has been considered here.

First we show results for the charge conductance for NS junctions. The variation of the charge conductance as a function of the biasing energy for a usual and graphene based junctions are shown in Fig.(7.1). It reveals that the Graphene based NS junction shows larger values of the conductance compared to that of the usual NS junction. Since the BTK calculations are complex and the transport depends on a large number of parameters, it is difficult to point out one

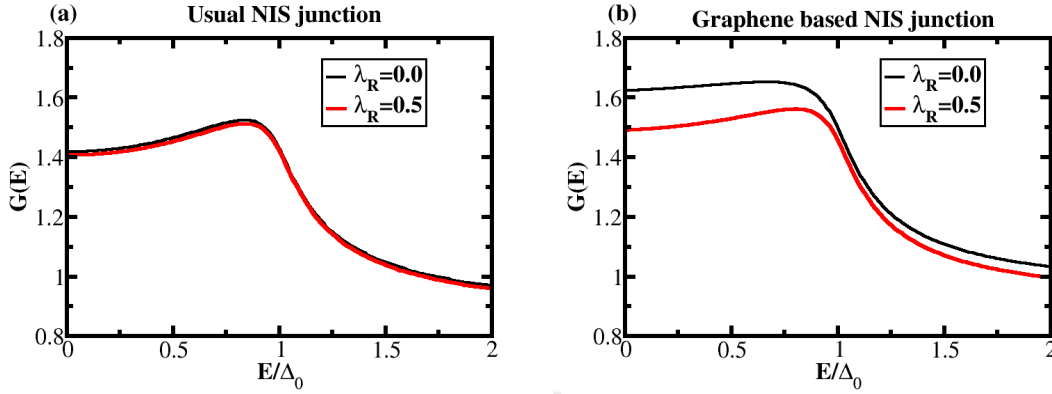


Figure 7.1: The variation of the conductance, G as a function of biasing energy, E (scaled by superconducting order parameter, Δ_0) for (a) usual NIS junction system and for (b) graphene based junction system. Graphene based NIS junctions register a slightly larger conductance.

factor contributing to this discrepancy, however an energy dependent density of states ($\text{DOS} \sim E$) for graphene (coupled with its high mobility) as opposed to a constant for parabolic dispersion is probably responsible for this graphene based junction to record larger transmission. Further for both, RSOC suppresses the conductance, while the suppression is larger in case of the graphene based Junction. Besides, we have already discussed earlier that usual NS junction does not show any spin resolved conductance with the inclusion of RSOC, whereas the graphene based NS junction shows spin polarized conductance owing to the fact $G_{\pm\sigma}(E, \pm\partial_{N1}) \neq G_{\mp\sigma}(E, \mp\partial_{N1})$, where $\pm\sigma$ refer to two spins, while $\pm\partial_{N1}$ denote angular values.

Now we show similar results for the NIS junction. The variation of the conductance as a function of effective barrier potential, χ for generic and graphene based junction systems are shown in Fig.(7.2a) and Fig.(7.2b) respectively. The Fermi energy of the superconducting lead has been considered as $E_F^S = E_F^N$ (no Fermi surface mismatch). Here we wish to mention that the insulating layer has been modeled in a different manner via an external gate voltage V_0 such that the Fermi surface is ramped up by V_0 in the insulating region and hence transport can be obtained through the junction. Without such a gate voltage for usual NIS junction, the conductance significantly decreases. But in case of a graphene based NIS junction, the conductance does not get suppressed as the usual case due to the Dirac-like energy dispersion. That is the essence of Klein tunneling. As expected, due to the Fabry-Perot oscillations, both the systems show oscillation pattern as a function of effective barrier potential, χ with the graphene based junction showing more conductance. Further with the inclusion of RSOC, for a usual NIS junction, the modifications of the conductance amplitude occur in such a way that for some region of the effective barrier potential, RSOC enhances

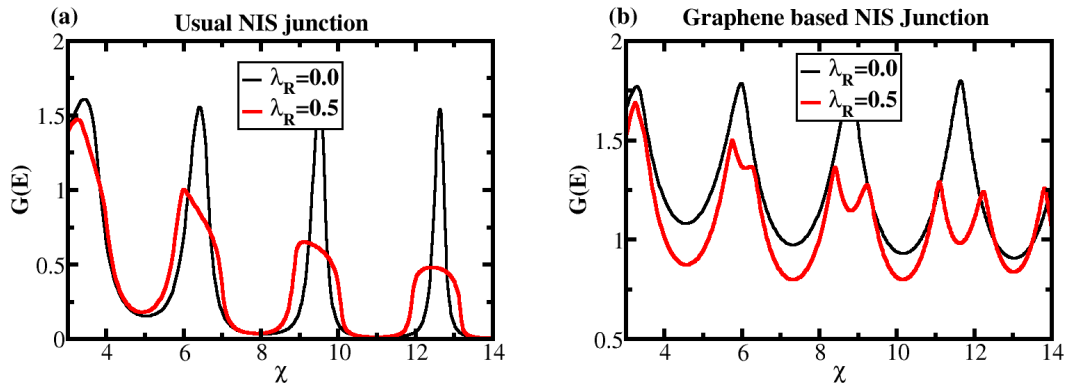


Figure 7.2: The variation of the conductance, G as a function χ , for (a) generic junction system (parabolic energy dispersion) and for (b) for graphene based junction system (linear energy dispersion).

the conductance, and for some other region, the reverse happens. However in contrary, the graphene based NIS junction does not show such modifications. As a result one gets only suppressed conductance in presence of RSOC. Further for a usual NIS junction, the oscillation patterns are exactly same for both spins in presence of RSOC. But in case of a graphene based NIS junction, the shift of peak positions occur in opposite directions for different spins in presence of RSOC (see Fig.(5.7)). Thus the variation of the total conductance as function of the biasing energy shows double peak type structure (see Fig.(7.2)).

7.2 Comparison of thermoelectric properties

Now we shift our focus on the thermoelectric properties. First we show results for the Seebeck coefficient. The variation of Seebeck coefficient as a function of temperature for parabolic and linear energy dispersions are shown in Fig.(7.3a) and Fig.(7.3b) respectively. We have considered such values for the effective barrier potential where the Seebeck coefficient records a maximum. It is evident from Fig.(7.3) that a usual NIS junction shows more Seebeck coefficient compared to that of the graphene based junction. Further, from Fig.(4.5), it is evident that for a usual junction system, for some region of effective barrier potential, RSOC enhances the Seebeck coefficient and for other regions the reverse happens. Note that this is similar to the results discussed in the previous section. However, in case of a graphene based junction we have checked that for all values of the effective barrier potential RSOC enhances the Seebeck coefficient. Besides, Fig.(7.3) reveals that the suppression of the Seebeck coefficient beyond a certain maximum value is larger in case of a usual NIS junction.

Finally We present results for the thermoelectric cooling. The variation of the

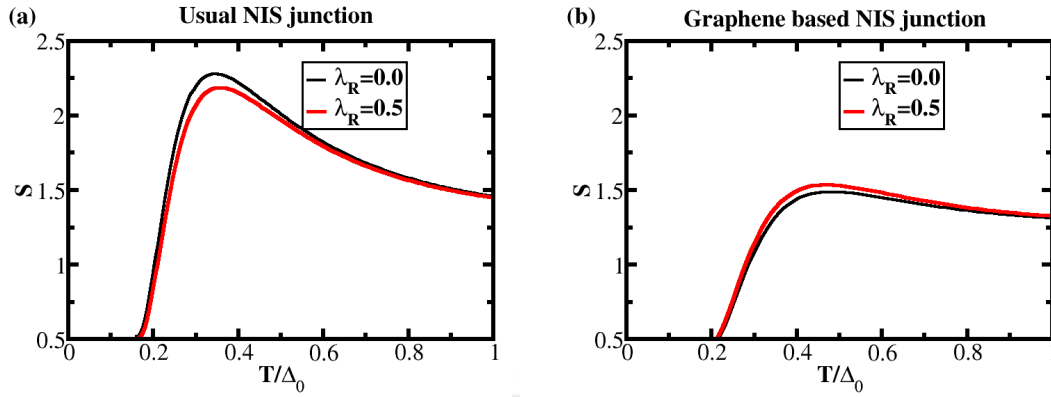


Figure 7.3: The variation of the Seebeck coefficient, S as a function of temperature, T/Δ_0 (scaled by superconducting order parameter, Δ_0) for (a) generic 2D junction system (parabolic dispersion) and for (b) graphene based junction system (linear energy dispersion). S is suppressed for the graphene based junction.

dimensionless thermal current, $(2J_{NS}e^2R_N)/\Delta_0^2$ as a function biasing voltage for parabolic and linear energy dispersions are shown in Fig.(7.4a) and Fig.(7.4b) respectively. We have again considered a particular value of the effective barrier potential, where the thermal current records a maximum value. The biasing voltage, V_B and the temperature, T are fixed at $V_B = 0.5\Delta_0$ and $T = 0.5\Delta_0$ respectively. It is evident from Fig.(7.4) that graphene based junctions show slightly larger thermal current which makes it more potential candidate for thermoelectric cooling compared to the usual NIS junction devices. Further in case of a usual NIS junction, whether the RSOC enhances or hinders the thermal current depends on the value of the effective barrier potential, whereas for a graphene based NIS junction, RSOC always diminishes the thermal current.

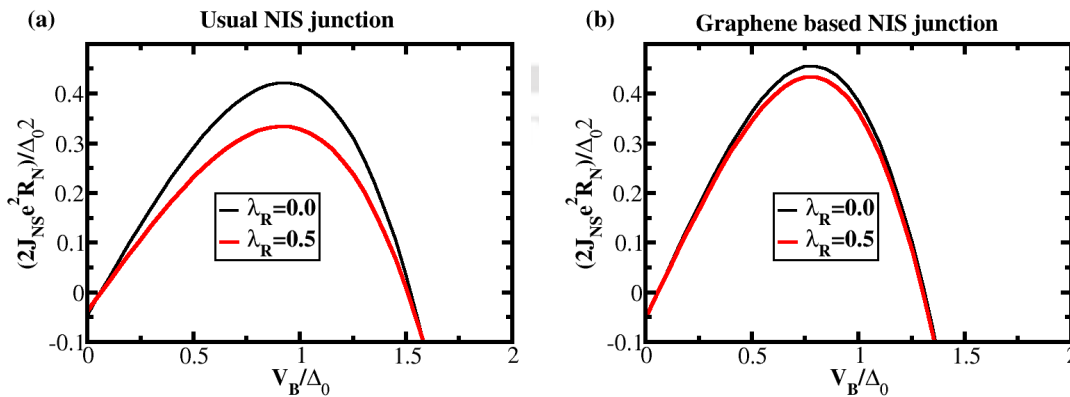


Figure 7.4: The variation of the dimensionless thermal current, $(2J_{NS}e^2R_N)/\Delta_0^2$ as a function of biasing voltage, V_B/Δ_0 (scaled by superconducting order parameter, Δ_0) for (a) generic 2D junction system (parabolic dispersion) and for (b) graphene based junction system (linear energy dispersion). The operating region is smaller for (b).

7.3 Conclusion

The comparison between a usual generic and a graphene based junction system shows that the graphene junctions shows more conductance compared to that of the generic system. For the usual NIS junction, the Fabry Perot oscillations show distinctive features with regard to the effective barrier potential, while the same is missing for the graphene based NIS junction. In the sense, in case of a usual NIS junction, the modification of oscillations pattern is such a way, that one can find some regions of effective barrier potential, where the RSOC enhances the conductance and some regions, where RSOC diminishes the conductance. But for graphene based NIS junction RSOC diminishes the conductance for all values of the effective barrier potential. Further it is obtained that the generic junction shows enhanced Seebeck coefficient, thereby ensuring larger thermopower can be delivered by the usual junction compared to the other. Whereas the graphene based junctions are more capable of thermoelectric cooling. Finally, in case of a generic NIS junction, whether RSOC enhances or hinders thermoelectric effect and thermoelectric cooling depends on the values of the effective barrier potential. But in case of a graphene based junction, RSOC always enhances the Seebeck coefficient and diminishes the thermal current.



Chapter 8: Conclusions

The study of nanoscale junction systems has been drawing a wide attention in condensed matter community due to its possible future applications in fabricating and characterizing nano-electronics devices. On the other hand, graphene is one of the most coveted candidates in contemporary research because of its various exciting electronic properties and also for the successful realization in the form of graphene nanoribbons, carbon nanotubes, graphene flakes etc., at the mesoscale or even lower dimension. Further, where the surface inversion symmetry breaks, the Rashba spin-orbit coupling (RSOC) becomes salient and hence cannot be ignored in the study of quantum transport across the junction systems. The ability to tune the strength of RSOC using an external field provides an additional boost to the exploration of tunable junction devices. Motivated by above we have extensively studied quantum transport of the junction devices in presence of spin-orbit couplings. An elaborate introduction of the topic is enclosed in chapter 1. The second chapter includes a detailed derivation of the formalism, namely Blonder-Tinkham-Klapwijk (BTK) theory to compute the conductance in presence of NS and NIS junctions for both usual and graphene based junctions.

As a startup problem, we have studied a generic two dimension normal-superconductor (NS) junction with parabolic dispersion in presence of Rashba spin-orbit coupling. Mainly we have studied an interplay of the RSOC with a number of parameters such as the barrier transparency, Fermi surface mismatch, finite quasiparticle life time, symmetry of the superconducting lead etc. It is obtained that for a transparent barrier, with no Fermi surface mismatch between the materials forming the metallic and the superconducting leads of our study, the conductance is not responsive to the value of RSOC. But in case of a Fermi surface mismatch, the conductance becomes sensitive to RSOC where we have found that the low energy conductance is suppressed by RSOC for all pairing symmetries for a transparent barrier. Whereas for an opaque barrier case, the RSOC enhances the low energy conductance irrespective of the presence of a Fermi surface mismatch. For different pairing symmetries, the conductance as a function of the biasing energy show different behavior. This emphasizes that the tunneling spectroscopy of a NS junction is an effective tool to acquire the information on the pairing gap of the superconducting lead. Further it is obtained that the quasiparticle lifetime broadens the conductance peak and diminishes its value. Also we obtain that the tunneling conductance enhances with increasing ratio of the Fermi surface mismatch (β). These results are presented in chapter 3.

Chapter 3 also contains an investigation of the tunneling conductance of a device consisting of a normal-insulator-superconductor (NIS) junction where the insulating layer is modeled by an external gate voltage such that the Fermi en-

ergy of the insulating layer is ramped by V_0 . We have observed Fabry-Perot like oscillatory behavior for the tunneling conductance spectrum as a function of the effective barrier potential (a product of the both V_0 and the width, d). The spin-orbit term shows interesting effects on the oscillation pattern, in the sense that it shifts the minima and maxima positions. The modification of the oscillation patterns is such that, for some values of the effective barrier potential, RSOC enhances the conductance, while for other it suppresses the conductance.

The next chapter that is, chapter 4 is based on the thermoelectric properties of the generic NIS junctions where we have investigated the thermoelectric response of a spin orbit coupled junction. As earlier, we found an oscillatory feature for the thermopower as a function of the effective barrier potential. This results show interesting interplay with the effective barrier potential. The thermopower, similar to the conductance profile, enhances with RSOC for certain ranges of this potential, while for others the reverse happens. Besides these, we have investigated the efficiency of the system as a thermopower device. An oscillatory nature for both the thermal current and coefficient of performance, COP of the device (with regard to the thermoelectric cooling) has been obtained as a function of the effective barrier potential. The interplay of the RSOC strength and the effective barrier potential is a crucial ingredient for determining the magnitude of the thermal current extracted from the metallic lead and its performance as a cooling device.

Since the strength of RSOC and the effective barrier potential can be tuned by external means, our studies on the conductance and thermoelectric properties can be an important inputs to experimental studies that aim to provide the desired conductance and thermoelectric properties of a NIS junction device.

Next two consecutive chapters, that is chapter 5 and chapter 6 are dedicated to adatom decorated graphene based NS and NIS junction that are mimicked by the Kane-Mele model. In summary, we have investigated the spin resolved transport properties of a Kane-Mele NS junction. We have studied the conductance properties in details with the Rashba and intrinsic terms included and computed the spin dependent transport. We have found that the RSOC hinders the tunneling conductance for both spins, while ISOC augments the conductance for the up spin and hinders for the down spin. Further, we have investigated the tunneling conductance of a Kane-Mele NIS junction. We observe an oscillatory behavior for the tunneling conductance spectrum as a function of the effective barrier potential. The RSOC term shifts the peak and dip positions. With the inclusion of RSOC there is no change in the peak values whereas the conductance near the dip decreases for both the spins. Further ISOC term does not shift the peak positions though enhances the conductance for up spin near the dip and diminishes for the down spin. It may be noted that, while modeling the insulating barrier in

a conventional way, we would not get any oscillation for a generic NIS junction, the graphene based junction will continue to demonstrate oscillatory conductance owing to the Klein tunneling.

In the chapter 6, we have investigated the thermoelectric properties of a Kane-Mele NIS junction in presence of spin-orbit couplings in sufficient details. We have investigated the Seebeck coefficient and the thermoelectric Figure of merit of this junction device and explained how the SOC parameters assume roles in shaping up these properties. Further, the thermoelectric cooling of this junction device and its performance as a cooling device have been studied in details. The thermoelectric properties emerge to be sensitive to the SOC parameters.

In the final chapter, that is chapter 7 we have compared between the usual (no relativistic) and the graphene based junction systems which shows that the graphene based junctions yield more conductance compared to that of the usual systems. In case of an NIS junction one can find some regions of effective barrier potential where the RSOC enhances the conductance, whereas for graphene based NIS junction, RSOC always diminishes the conductance. Further, the comparison of thermoelectric properties shows that the generic junctions show more thermopower, whereas the graphene based junction systems have better uses towards thermoelectric cooling.



Chapter 9: Appendix: Simpson's Rule for 2D integration

Consider the double integral of the form,

$$I = \int_{a_y}^{b_y} \int_{a_x}^{b_x} f(x, y) dx dy \quad 9.1$$

It can be approximated by applying Simpson's 1/3 rule. First for the x integration and then for the y integration with N partitions for both the x and y values, such that,

x -values: $x_1, x_2, x_3, x_4, \dots, x_c, \dots, x_N$

y -values: $y_1, y_2, y_3, y_4, \dots, y_c, \dots, y_N$

The lower and upper bounds determine the sizes of the partitions,

$$h_x = \frac{b_x - a_x}{N - 1} ; h_y = \frac{b_y - a_y}{N - 1} \quad 9.2$$

The N number x -values and y -values form a two-dimensional grid of $N \times N$ points. The function $f(x, y)$ and the two-dimensional Simpson's coefficients are calculated at each grid point. Hence, the function $f(x, y)$ and the two-dimensional Simpson's coefficients can be represented by $N \times N$ matrices, F and S respectively. The Simpson matrix S for $N = 5$ is

$$\begin{pmatrix} 1 & 4 & 2 & 4 & 1 \\ 4 & 16 & 8 & 16 & 4 \\ 2 & 8 & 4 & 8 & 2 \\ 4 & 16 & 8 & 16 & 4 \\ 1 & 4 & 2 & 4 & 1 \end{pmatrix} \quad 9.3$$

Therefore, the two-dimensional Simpson's rule which is used to estimate the value of the surface integral can be expressed as,

$$I = \frac{h_x h_y}{9} \sum_{m=1}^N \sum_{n=1}^N (S_{mn} F_{mn}) \quad 9.4$$

This technique of integrating a doubly variable function is used extensively for computing Seebeck coefficient, thermoelectric cooling and its performance etc. Basically, it is used to integrate over the energy variable in addition to the angular integration.



Bibliography

- [1] R. G. Garcia, *Appl. Phys. Lett.*, vol. 60, p. 1960, 1992.
- [2] M. A. McCord and R. F. W. Pease, *Journal of Vacuum Science and Technology B : Microelectronics Processing and Phenomena*, vol. 4, p. 86, 1986.
- [3] R. J. Colton, D. DiLella, R. L. Mowery, A. Snow, J. H. Wandass, and C. R. K. Marrian, *Journal of Vacuum Science and Technology A: Vacuum, Surfaces, and Films*, vol. 6, p. 933, 1988.
- [4] D. P. DiLella, J. H. Wandass, R. J. Colton, and C. R. K. Marrian, *Review of Scientific Instruments*, vol. 60, p. 997, 1989.
- [5] C. R. K. Marrian and R. J. Colton, *Appl. Phys. Lett.*, vol. 56, p. 755, 1990.
- [6] E. A. Dobisz, C. R. K. Marrian, and R. J. Colton, *Journal of Applied Physics*, vol. 70, p. 1793, 1991.
- [7] M. Nahum and J. M. Mortinis, *Appl. Phys. Lett.*, vol. 63, p. 3075, 1993.
- [8] A. V. Feshchenko, J. V. Koski, and J. P. Pekola, *Phys. Rev. B*, vol. 90, p. 201407, 2014.
- [9] A. M. Clark, A. Williams, S. T. Ruggiero, M. L. Berg, and J. N. Ullom, *Appl. Phys. Lett.*, vol. 84, p. 625, 2004.
- [10] N. A. Miller, G. C. O'Neil, J. A. Beall, G. C. Hilton, K. D. Irwin, L. R. V. R Schmidt, and J. N. Ullom, *Appl. Phys. Lett.*, vol. 92, p. 163501, 2008.
- [11] P. Reddy, S. Y. Jang, R. A. Segalman, and A. Majumdar, *Science*, vol. 315, p. 1568, 2007.
- [12] B. Ludoph and J. M. Ruitenbeek, *Phys. Rev. B*, vol. 59, p. 12290, 1999.
- [13] K. Baheti, J. A. Malen, P. Doak, P. Reddy, S. Y. Jang, T. D. Tilley, A. Majumder, and R. A. Segalman, *Nano. Lett.*, vol. 8, p. 715, 2008.
- [14] J. A. Malen, P. Doak, K. Baheti, T. D. Tilley, R. A. Segalman, and A. Majumder, *Nano. Lett.*, vol. 9, p. 1164, 2009.
- [15] M. Nahum, T. M. Eiles, and J. M. Martinis, *Appl. Phys. Lett.*, vol. 65, p. 3123, 1994.
- [16] B. R. Choi, A. E. Hansen, T. Kontos, C. Hoffmann, S. Oberholzer, W. Belzig, and C. Schonenberger, *Phys. Rev. B*, vol. 72, p. 024501, 2005.

- [17] Y. S. Liu, B. C. Hsu, and Y. C. Chen, *J. Phys. Chem*, vol. 115, p. 6111, 2011.
- [18] J. Mastomaki, S. Roddaro, M. Rocci, V. Zannier, D. Ercolani, L. Sorba, I. J. Maasilta, N. Ligato, A. Fornieri, E. Strambini, and F. Giazotto, *Nano Res.*, vol. 10, p. 3468, 2017.
- [19] G. Deutscher, *Rev. Mod. Phys.*, vol. 77, p. 109, 2005.
- [20] D. Daghero and R. S. Gonnelli, *Supercond. Sci. Technol*, vol. 23, p. 043001, 2010.
- [21] G. Goll, H. Lohneysen, I. Yanson, and L. Taillefer, *Phys. Rev. Lett.*, vol. 70, p. 2008, 1993.
- [22] K. Hasselbach, J. Kirtley, and P. Lejay, *Physica B*, vol. 186-188, p. 201, 1993.
- [23] G. Ernst, A. Nowack, M. Weger, and D. Schweizer, *Euro Phys. Lett*, vol. 25, p. 303, 1994.
- [24] D. Wollman, D. Harlingen, W. Lee, D. Ginsberg, and A. Leggett, *Phys. Rev. Lett*, vol. 71, p. 2134, 1993.
- [25] C. Tsuei and J. R. Kirtley, *Rev. Mod. Phys*, vol. 72, p. 969, 2000.
- [26] C. C. Tsuei and J. R. Kirtley, *Phys. Rev. Lett.*, vol. 85, p. 182, 2000.
- [27] A. F. Andreev and T. M. Rice, *Sov. Phys. JETP*, vol. 19, p. 1228, 1964.
- [28] A. F. andreev, *Zh. Eksp. Teor. Fiz*, vol. 46, p. 1823, 1964.
- [29] A. Furusaki and M. Tsukada, *Solid State Commun.*, vol. 78, p. 299, 1991.
- [30] G. E. Blonder, M. Tinkham, and T. M. Klapwijk, *Phys. Rev. B*, vol. 25, p. 4515, 1982.
- [31] P. G. D. Gennes and D. S. James, *Phys. Lett.*, vol. 4, p. 151, 1963.
- [32] D. S. James, *J. de Physique*, vol. 25, p. 899, 1964.
- [33] J. Pankove, *Phys. Lett.*, vol. 21, p. 406, 1966.
- [34] F. Laube, G. Goll, H. v Lohneysen, M. Fogelstrom, and F. Lichtenberg, *Phys. Rev. Lett.*, vol. 84, p. 1595, 2000.
- [35] W. K. Park, J. L. Sarrao, J. D. Thompson, and L. H. Greene, *Phys. Rev. Lett.*, vol. 100, p. 177001, 2008.

- [36] L. Shan, H. J. Tao, H. Gao, Z. Z. Li, Z. A. Ren, G. C. Che, and H. H. Wen, *Phys. Rev. B*, vol. 68, p. 144510, 2003.
- [37] P. Szabo, P. Samuely, J. Kacmarcik, T. Klein, J. Marcus, D. Fruchart, S. Miraglia, C. Marcenat, and A. G. M. Jansen, *Phys. Rev. Lett.*, vol. 87, p. 137005, 2001.
- [38] G. E. Blonder and M. Tinkham, *Phys. Rev. B*, vol. 27, p. 112, 1983.
- [39] E. I. Rashba, *Fiz. Tverd. Tela*, vol. 2, p. 1224, 1960.
- [40] de Andrada e Silva E A, G. C. L. Rocca, and F. Bassani, *Phys. Rev. B*, vol. 50, p. 8523, 1994.
- [41] E. Silva, G. C. L. Rocca, and F. Bassani, *Phys. Rev. B*, vol. 55, p. 16293, 1997.
- [42] J. Nitta, T. Akazaki, H. Takayanagi, and T. Enoki, *Phys. Rev. Lett.*, vol. 78, p. 1335, 1997.
- [43] G. Engels, J. Lange, T. Schapers, and H. Luth, *Phys. Rev. B*, vol. 55, p. R1958, 1997.
- [44] D. Liang and X. P. A. Gao, *Nano. Lett.*, vol. 12, p. 3263, 2012.
- [45] S. Datta and B. Das, *Appl. Phys. Lett.*, vol. 56, p. 665, 1990.
- [46] D. Frustaglia and K. Richter, *Phys. Rev. B*, vol. 69, p. 235310, 2004.
- [47] R. Ionicioiu and I. Damico, *Phys. Rev. B*, vol. 67, p. 041307, 2003.
- [48] K. S. Novoselov, A. K. Geim, S. V. Morozov, D. Jiang, Y. Zhang, S. V. Dubonos, and V. G. A. A. Firsov, *Science*, vol. 306, p. 666, 2004.
- [49] A. H. C. Neto, F. Guinea, N. M. R. Peres, K. S. Novoselov, and A. K. Geim, *Rev. Mod. Phys.*, vol. 81, p. 109, 2009.
- [50] Y. Zhang, Y. Y. W. Tan, H. L. Stormer, and P. Kim, *Nature*, vol. 438, p. 201, 2005.
- [51] V. P. Gusynin and S. G. Sharapov, *Phys. Rev. Lett.*, vol. 95, p. 146801, 2005.
- [52] E. J. Kan, Z. Li, J. Yang, and J. G. Hou, *Appl. Phys. Lett.*, vol. 91, p. 243116, 2007.
- [53] X. Lin and J. Ni, *Phys. Rev. B.*, vol. 84, p. 075461, 2011.

- [54] X. Du, I. Skachko, A. Barker, and E. Y. Andrei, *Nat. Nanotech.*, vol. 3, p. 491, 2008.
- [55] A. H. C. Neto, F. Guinea, N. M. R. Peres, K. S. Novoselov, and A. K. Geim, *Rev. Mod. Phys.*, vol. 81, p. 109, 2009.
- [56] M. I. Katnelson and K. S. Novoselov, *Solid State Commun.*, vol. 143, p. 3, 2007.
- [57] A. H. Neto, F. Guinea, and N. M. R. Peres, *Phys. World*, vol. 19, p. 33, 2006.
- [58] M. I. Katsnelson, K. S. Novoselov, and A. K. Geim, *Nat. Phys.*, vol. 2, p. 620, 2006.
- [59] A. Calogeracos and N. Dombey, *Contemp. Phys.*, vol. 40, p. 313, 1999.
- [60] C. Itzykson and J. B. Zuber, *Quantum Field Theory*, Dover, New York.
- [61] J. M. Pereira, P. Vasilopoulos, and F. M. Peeters, *Nano Lett.*, vol. 7, p. 946, 2007.
- [62] A. K. Geim and K. S. Novoselov, *Nature Mater.*, vol. 6, p. 183, 2007.
- [63] V. V. Cheianov, V. Fal'ko, and B. L. Altshuler, *Science*, vol. 315, p. 1252, 2007.
- [64] M. C. Lemme, T. J. Echtermeyer, M. Baus, and H. Kurz, *IEEE Electron Device Lett.*, vol. 28, p. 282, 2007.
- [65] J. R. Williams, L. DiCarlo, and C. M. Marcus, *Science*, vol. 317, p. 638, 2007.
- [66] M. M. Fogler, L. I. Glazman, D. S. Novikov, and B. I. Shklovskii, *Phys. Rev. B*, vol. 77, p. 075420, 2008.
- [67] A. Ossipov, M. Titov, and C. W. J. Beenakker, *Phys. Rev. B*, vol. 75, p. 241401, 2007.
- [68] T. O. Wehling, K. S. Novoselov, S. V. Morozov, E. E. Vdovin, M. I. Katsnelson, A. K. Geim, and A. I. Lichtenstein, *Nano Lett.*, vol. 8, p. 173, 2008.
- [69] F. Schedin, A. K. Geim, S. V. Morozov, D. Jiang, E. W. Hill, P. Blake, and K. S. Novoselov, *Nature Mater.*, vol. 6, p. 652, 2007.
- [70] M. Ohishi, M. Shiraishi, R. Nouchi, T. Nozaki, T. Shinjo, and Y. Suzuki, *Jpn. J. Appl. Phys.*, vol. Part 2 46, p. L605, 2007.

- [71] E. W. Hill, A. K. Geim, K. Novoselov, F. Schedin, and P. Blake, *IEEE Trans. Magn.*, vol. 42, p. 2694, 2007.
- [72] N. Tombros, C. Jozsa, M. Popinciuc, H. T. Jonkman, and J. van Wees, *Nature*, vol. 448, p. 571, 2007.
- [73] S. Cho, Y. F. Chen, and M. S. Fuhrer, *Appl. Phys. Lett.*, vol. 91, p. 123105, 2007.
- [74] J. C. Meyer, A. K. Geim, K. S. Novoselov, T. J. Booth, and S. Roth, *Nature*, vol. 446, p. 60, 2007.
- [75] S. V. Morozov, K. S. Novoselov, M. I. Katsnelson, F. Schedin, L. A. Ponomarenko, D. Jiang, and A. K. Geim, *Phys. Rev. Lett.*, vol. 97, p. 016801, 2006.
- [76] A. A. Balandin, S. Ghosh, W. Bao, I. Calizo, D. Teweldebrhan, F. Miao, and C. N. Lau, *Nano. Lett.*, vol. 8, p. 902, 2008.
- [77] Y. M. Zuev, W. Chang, and P. Kim, *Phys. Rev. Lett.*, vol. 102, p. 096807, 2009.
- [78] D. Dragoman and M. Dragoman, *Appl. Phys. Lett.*, vol. 91, p. 203116, 2007.
- [79] B. Uchoa and A. H. C. Neto, *Phys. Rev. Lett.*, vol. 98, p. 146801, 2007.
- [80] A. I. Buzdin, *Rev. Mod. Phys.*, vol. 77, p. 935, 2005.
- [81] H. B. Heersche, P. J. Herrero, J. B. Oostinga, L. M. Vandersypen, and A. F. Morpurgo, *Solid state Comm.*, vol. 143, p. 72, 2007.
- [82] C. L. Kane and E. J. Mele, *Phys. Rev. Lett.*, vol. 95, p. 226801, 2005.
- [83] E. J. Mele and C. L. Kane, *Phys. Rev. Lett.*, vol. 95, p. 146802, 2005.
- [84] F. D. M. Haldane, *Phys. Rev. Lett.*, vol. 61, p. 2015, 1988.
- [85] H. Min, J. E. Hill, N. A. Sinitsyn, B. R. Sahu, L. Kleinman, and A. H. MacDonald, *Phys. Rev. B*, vol. 74, p. 165310, 2006.
- [86] Y. G. Yao, F. Ye, X. L. Qi, S. C. Zhang, and Z. Fang, *Phys. Rev. Lett.*, vol. 75, p. 041401, 2007.
- [87] C. Weeks, J. Hu, J. Alicea, M. Franz, and R. Wu, *Phys. Rev. X*, vol. 1, p. 021001, 2011.
- [88] L. Kou, B. Yan, F. Hu, S. C. Wu, T. O. Wehling, C. Felser, C. Chen, and T. Frauenheim, *Nano. Lett.*, vol. 13, p. 6251, 2013.

- [89] K. Zollner, T. Frank, S. Irmer, M. Gmitra, D. Kochan, and J. Fabian, *Phys. Rev. B*, vol. 93, p. 045423, 2015.
- [90] D. Marchenko, A. Varykhalov, M. R. Scholz, G. Bihlmayer, E. I. Rashba, A. Rybkin, A. M. Shikin, and O. Rader, *Nat. Commun.*, vol. 3, p. 1232, 2012.
- [91] Y. S. Dedkov, M. Fonin, U. Rudiger, and C. Laubschat, *Phys. Rev. Lett.*, vol. 100, p. 107602, 2008.
- [92] W. Greiner, *Relativistic quantum mechanics, springer, Germany*, 1984.
- [93] G. Dresselhaus, *Phys. Rev.*, vol. 100, p. 580, 1955.
- [94] E. I. Rashba, *Sov. Phys. Solid State*, vol. 2, p. 1109, 1960.
- [95] N. A. Sinitsyn, E. M. Hankiewicz, W. Teizer, and J. Sinova, *Phys. Rev. B*, vol. 70, p. 081312, 2004.
- [96] D. Bercioux and P. Lucignano, *Reports on Progress in Physics*, vol. 78, p. 106001, 2015.
- [97] J. Bardeen, L. N. Cooper, and J. R. Schrieffer, *Phys. Rev.*, vol. 108, p. 1175, 1957.
- [98] W. L. McMillan and J. M. Rowell, *Superconductivity*, vol. 1, Chap 11, New York, 1969.
- [99] D. J. Scalapino, *Superconductivity*, vol. 1, Chap10, New York, 1969.
- [100] D. J. Scalapino, J. R. Schrieffer, and J. Wilkins, *Phys. Rev.*, vol. 148, p. 263, 1966.
- [101] P. G. DeGennes, *Superconductivity Of Metals And Alloys*, Chap. 5, Westview Press, Boulder, 1999.
- [102] V. Lukic, *Thesis: Conductance of superconductor-normal metal contact junction beyond quasiclassical approximation*, University of Belgrade, 1997.
- [103] A. G. M. Jansen, F. M. Mueller, and P. Wyder, *Phys. Rev.*, vol. 16, p. 1325, 1977.
- [104] P. N. Chubov, I. K. Yanson, and A. I. Akimenko, *J. Low Temp. Phys.*, vol. 8, p. 32, 1982.
- [105] K. S. Ralls, R. A. Buhrman, and R. C. Tiberio, *Appl. Phys. Lett.*, vol. 55, p. 2459, 1989.

- [106] C. J. Muller, J. M. van Ruitenbeek, and L. J. de Jongh, *Physica C*, vol. 191, p. 485, 1992.
- [107] L. Viti, M. S. Vitiello, D. Ercolani, and L. Sorba, *Nanoscale Res Lett.*, vol. 7, p. 159, 2012.
- [108] D. B. Suyatin, C. Thelander, M. T. Bjork, I. Maximov, and L. Samuelson, *Nanotechnology*, vol. 18, p. 105307, 2007.
- [109] S. T. Ruggiero, A. Williams, W. H. Rippard, A. Clark, S. W. Deiker, L. R. Vale, and J. N. Ullom, *J. Low Temp. Phys.*, vol. 134, p. 973, 2004.
- [110] J. H. Chen, C. Jang, S. Xiao, M. Ishigami, and M. S. Fuhrer, *Nat Nano*, vol. 3, p. 206, 2008.
- [111] O. Klein, *Z. Phys.*, vol. 53, p. 157, 1929.
- [112] T. Ando, T. Nakanishi, and R. Sato, *J. Phys. Soc. Jpn*, vol. 67, p. 2857, 1998.
- [113] S. Murakami, N. Nagaosa, and S. C. Zhang, *Science*, vol. 301, p. 1348, 2003.
- [114] J. Sinova, D. Culcer, Q. Niu, N. A. Sinitsyn, T. Jungwirth, and A. H. MacDonald, *Phys. Rev. Lett.*, vol. 92, p. 126603, 2004.
- [115] J. Zhang, C. Triola, and E. Rossi, *Phys. Rev. Lett.*, vol. 112, p. 096802, 2014.
- [116] S. Wu and K. V. Samokhin, *Phys. Rev. B*, vol. 81, p. 214506, 2010.
- [117] X. Li, *Physica C*, vol. 485, p. 35, 2013.
- [118] Y. Tanaka and S. Kashiwaya, *Phys. Rev. Lett.*, vol. 74, p. 3451, 1995.
- [119] R. Vali and M. Vali, *J. Phys. Condens. Matter*, vol. 24, p. 325702, 2012.
- [120] Y. G. Naidyuk and I. K. Yanson, *Point-contact spectroscopy. Springer, Chap. 2, New York.*, 2005.
- [121] R. Hu, *Phys. Rev. Lett.*, vol. 72, p. 1526, 1994.
- [122] S. Kashiwaya, Y. Tanaka, H. Takashima, M. Koyanagi, and K. Kajimura, *Phys. Rev. B*, vol. 51, p. 1350, 1995.
- [123] T. Lofwander, V. S. Shumeiko, and G. Wendin, *Supercond. Sci. Technol.*, vol. 14, p. R53, 2001.

- [124] Z. Q. Mao, K. D. Nelson, R. Jin, Y. Liu, and Y. Maeno, *Phys. Rev. Lett.*, vol. 87, p. 037003, 2001.
- [125] M. Yamashiro, Y. Tanaka, and S. Kashiwaya, *Phys. Rev. B*, vol. 56, p. 7847, 1997.
- [126] C. Honerkamp and M. Sigrist, *J. Low Temp. Phys.*, vol. 111, p. 895, 1998.
- [127] T. Matsuyama, R. Kirsten, C. Meiniser, and U. Merkt, *Phys. Rev. B*, vol. 61, p. 15858, 2000.
- [128] S. Wu and K. V. Samokhin, *Phys. Rev. B*, vol. 82, p. 184501, 2010.
- [129] S. Singh and A. H. Romero, *Phys. Rev. B*, vol. 95, p. 165444, 2017.
- [130] Z. Yang, J. Wang, and K. S. Chan, *J. Phys. Soc. Jpn.*, vol. 78, p. 084706, 2009.
- [131] S. S. Kashiwaya and Y. Y. Tanaka, *Phys. Rev. B*, vol. 53, p. 2667, 1996.
- [132] M. Covington, M. Aprili, E. Paraoanu, L. H. Greene, F. Xu, J. Zhu, and C. A. Mirkin, *Phys. Rev. Lett.*, vol. 79, p. 277, 1997.
- [133] J. Y. T. Wei, N. C. Yeh, D. F. Garrigus, and M. Strasik, *Phys. Rev. Lett.*, vol. 81, p. 2542, 1998.
- [134] J. Hu, J. Alicea, R. Wu, and M. Franz, *Phys. Rev. Lett.*, vol. 109, p. 0266801, 2012.
- [135] E. Tuuli and K. Gloos, *Low temp. Phys.*, vol. 37, p. 485, 2011.
- [136] K. E. Gray, *J. Phy. F: Metal Physics*, vol. 1, p. 290, 1970.
- [137] M. Zemlicka, P. Neilinger, M. Trgala, M. Rehak, D. Manca, , and M. Grajcar, *Phys. Rev. B*, vol. 92, p. 224506, 2015.
- [138] A. Plecenik, M. Grajcar, S. Benacka, P. Seidel, and A. Pfuch, *Phys. Rev. B*, vol. 49, p. 10016, 1994.
- [139] Y. de Wilde, T. M. Klapwijk, A. G. M. Jansenm, J. Heil, and P. Wyder, *Physica B*, vol. 218, p. 165, 1996.
- [140] P. Kapri and S. Basu, *Euro. Phys. J. B*, vol. 90, p. 33, 2017.
- [141] S. Bhattacharjee and K. Sengupta, *Phys. Rev. Lett.*, vol. 97, p. 217001, 2006.
- [142] Y. Zhang, M. Han, and L. Shen, *Physica B*, vol. 405, p. 1168, 2010.

- [143] A. V. Kretinin, R. P. Biro, D. Mahalu, and H. Shtrikman, *Nano. Lett.*, vol. 10, p. 3439, 2010.
- [144] W. A. Little, *Microminiature refrigeration. Review of Scientific Instruments*, vol. 55(5), p. 661, 1984.
- [145] C. K. Stahle, D. McCammon, and K. D. Irwin, *Physics Today*, vol. 52, p. 32, 1999.
- [146] M. M. Leivo, J. P. Pekola, and D. V. Averin, *Appl. Phys. Lett.*, vol. 68, p. 1996, 1996.
- [147] A. M. Clark, N. A. Miller, A. Williams, S. T. Ruggiero, G. C. Hilton, L. R. Vale, J. A. Beall, K. D. Irwin, and J. N. Ullom, *Appl. Phys. Lett.*, vol. 86, p. 173508, 2005.
- [148] T. Yokoyama, J. Linder, and A. Sudbo, *Phys. Rev. B*, vol. 77, p. 132503, 2008.
- [149] W. Zhang, S. Yi, and L. You, *New Journal of Physics*, vol. 5, no. 1, p. 77, 2003.
- [150] K. S. Novoselov, A. K. Geim, S. V. Morozov, D. Jiang, M. I. Katsnelson, I. V. Grigorieva, S. V. Dubonos, and A. AFirsov, *Nature*, vol. 438, p. 197, 2005.
- [151] A. D. Martino, L. DellAnna, and R. Egger, *Phys. Rev. Lett.*, vol. 98, p. 066802, 2007.
- [152] F. Bonaccorso, Z. Sun, T. Hasan, and A. C. Ferrari, *Nat. Photonics.*, vol. 4, p. 611, 2010.
- [153] P. Avouris, *Nano. Lett.*, vol. 10, p. 4285, 2010.
- [154] A. G. Moghaddam and M. Zareyan, *Phys. Rev. Lett.*, vol. 105, p. 146803, 2010.
- [155] D. Pesin and A. H. MacDonald, *Nat. Mat.*, vol. 11, p. 409, 2012.
- [156] W. Han, R. K. Kawakami, M. Gmitra, and J. Fabian, *Nat. Nanotechnol.*, vol. 9, p. 794, 2014.
- [157] B. Ghosh, *J. Appl. Phys.*, vol. 109, p. 013706, 2011.
- [158] C. W. J. Beenakker, *Rev. Mod. Phys.*, vol. 80, p. 1337, 2008.
- [159] M. Zareyan, H. Mohammadpour, and A. G. Moghaddam, *Phys. Rev. B*, vol. 78, p. 193406, 2008.

- [160] C. W. J. Beenakker, *Phys. Rev. Lett.*, vol. 97, p. 067007, 2006.
- [161] F. Calleja, H. Ochoa, M. Garnica, S. Barja, J. J. Navarro, A. Black, M. M. Otrokov, E. V. Chulkov, A. Arnau, A. L. V. Parga, F. Guinea, and R. Miranda, *Nature Phys.*, vol. 11, p. 43, 2015.
- [162] K. Uchida, S. Takahashi, K. Harii, J. Ieda, W. Koshibae, K. Ando, S. Maekawa, and E. Saitoh, *Nature*, vol. 455, p. 778, 2008.
- [163] C. M. Jaworski, R. C. Myers, E. Johnston-Halperin, and J. P. Heremans, *Nature*, vol. 487, p. 210, 2012.
- [164] R. Swirkowicz, M. Wierzbicki, and J. Barana, *Phys. Rev. B*, vol. 80, p. 195409, 2009.
- [165] M. Hatami, G. E. W. Bauer, Q. F. Zhang, and P. J. Kelly, *Phys. Rev. B*, vol. 79, p. 174426, 2009.
- [166] X. B. Chen, Y. Z. Liu, B. L. Gu, W. H. Duan, and F. Liu, *Phys. Rev. B*, vol. 90, p. 121403, 2014.

Curriculum vitae

Priyadarshini Kapri was born on 24th August, 1990 in Kolkata, India. She did her B.Sc. with Physics Honours in 2011 from Bethune College under Calcutta University and M.Sc. in Physics from Indian Institute of Technology Guwahati in 2013. She had enrolled into the Ph.D programme at Indian Institute of Technology Guwahati in 2013. She had qualified Joint Entrance Screening Test (JEST) and Graduate Aptitude Test in Engineering (GATE) in 2013 and 2014. She has earned the Senior Research Fellowship in 2015 by Indian Institute of Technology Guwahati.





Indian Institute of Technology Guwahati- Department of Physics- Guwahati-781039, Assam, India

**Electrical and Thermal Transport through
Spin-Orbit coupled Nano-junctions: An em-
phasis on Graphene based junction devices**



Priyadarshini Kapri
Roll No.-136121017

A Thesis submitted for the award of the degree of Doctor of Philosophy in Physics by

Guwahati,
December
2018

barcode label

Indian Institute of Technology Guwahati- Department of Physics- Guwahati-781039, Assam, India

**Electrical and Thermal Transport through
Spin-Orbit coupled Nano-junctions: An em-
phasis on Graphene based junction devices**



Priyadarshini Kapri
Roll No.-136121017

**PhD
Thesis**

Guwahati,
December
2018

barcode label





Indian Institute of Technology Guwahati
Department of Physics.
Guwahati-781039, Assam, India

A Thesis submitted for the award of the de-
gree of Doctor of Philosophy in Physics by

**Electrical and Thermal Transport through
Spin-Orbit coupled Nano-junctions: An em-
phasis on Graphene based junction devices**

Priyadarshini Kapri

Guwahati
December 2018



Indian Institute of Technology Guwahati
Department of Physics
Guwahati-781039, Assam, India

A Thesis submitted for the award of the de-
gree of Doctor of Philosophy in Physics by

**Electrical and Thermal Transport through
Spin-Orbit coupled Nano-junctions: An em-
phasis on Graphene based junction devices**

Priyadarshini Kapri

Guwahati
December 2018

9.0.0.0.1

